Modelling and Simulation of Chiral and non-Chiral Nematic Liquid Crystals Between Cylinders

by

Arash Nikzad

A THESIS SUBMITTED IN PARTIAL FULFILLMENT OF THE REQUIREMENTS FOR THE DEGREE OF

DOCTOR OF PHILOSOPHY

in

THE FACULTY OF GRADUATE AND POSTDOCTORAL STUDIES

(Mechanical Engineering)

THE UNIVERSITY OF BRITISH COLUMBIA

(Vancouver)

December 2022

The following individuals certify that they have read, and recommend to the Faculty of Graduate and Postdoctoral Studies for acceptance, the dissertation entitled:

Modelling and Simulation of Chiral and non-Chiral Nematic Liquid Crystals Between Cylinders

submitted by Arash Nikzad in partial fulfilment of the requirements for

the degree of Doctor of Philosophy

in Mechanical Engineering

Examining Committee:

Dr. Dana Grecov, Professor, Mechanical Engineering, UBC
Supervisor

Dr. Mattia Bacca, Assistant Professor, Mechanical Engineering
Supervisory Committee Member

Dr. Fariborz Taghipour, Professor, Chemical and Biological Engineering, UBC
University Examiner

Dr. Abbas Milani, Professor, Mechanical Engineering, UBC
University Examiner

Additional Supervisory Committee Members:

Dr. Ian Frigaard, Professor, Mechanical Engineering
Supervisory Committee Member

Dr. Mark Martinez, Professor, Chemical and Biological Engineering
Supervisory Committee Member

Abstract

Liquid crystallinity defines a state between a crystal solid and a liquid. Liquid Crystal (LC) molecules have the flowing properties of liquids while they keep the orientational order of solids with no positional order. To study the characteristics of disc-like LCs, initially, an analytical method to calculate the viscosity coefficients and rheological properties of discotic nematic liquid crystals (DNLCs) was proposed. The method was illustrated on nematic Graphene oxide (GO) dispersions, the most processable graphene derivative, as an example of DNLCs. GO dispersions have attracted enormous attention due to their unique liquid crystal (LC) characteristics. In the second step, the calculated Landau and Leslie viscosity coefficients were implemented in the Ericksen-Leslie (EL) theory to simulate the flow of GO dispersions. GO aqueous suspensions, with a concentration range of 15 mg/mL to 30 mg/mL, were simulated as a lubricant between two cylinders with a small gap size, which is the preliminary geometry for journal bearings. The anisotropic feature of LCs leads to a preferred direction of the molecules close to the solid surfaces, making them an outstanding candidate for the lubrication problem. Flow properties of GO dispersions at different concentrations were calculated numerically using the EL theory and compared with the respective theoretical values, which were within 1% error. Lastly, the Landau-de Gennes theory was applied to investigate the behaviour of chiral liquid crystals (CLCs) between concentric and eccentric cylinders under different flow conditions. This theory was implemented using dynamic finite element simulations (COMSOL Multiphysics) to solve the evolution of the microstructure of CLCs and coupled with a linear momentum balance equation to capture the structure of CLCs. This section focused on the microstructure formation of CLCs and their performance as lubricants under various chirality strengths (θ), Deborah numbers (De), and eccentricity of eccentric cylinders. The hexagonal structure of the CLCs at low De, where the chiral term predominates, was observed, while at higher De, the hexagonal pattern vanished. The eccentricity ratio impact on the performance of CLCs was also considered, and it was concluded that CLCs as lubricants perform well at high θ and eccentricity and low De.

Lay Summary

Preventing energy dissipation from friction and wear in machines with rubbing surfaces has attracted increasing attention. An antiwear and friction-reducing lubricant was shown to save 1% of the gross national product (GNP). A breakthrough in lubricant design is employing Liquid Crystals (LCs) to reduce the energy lost through friction. LCs are remarkable since their molecules align between two sliding surfaces so that the frictional resistance is extremely low. The substantial difference of LCs from usual lubricants is that the molecules in LCs possess a preferred orientation. Therefore, understanding the physics behind applying LCs as lubricant optimizes the performance of systems with sliding surfaces, like journal bearings. In this study, we simulate the flow of LCs between two cylinders with a small gap size, the preliminary geometry for journal bearings, to provide insights into their behaviour and improve the energy efficiency of journal bearings.

Preface

This thesis is the outcome of my graduate study at the Mechanical Engineering Department at the University of British Columbia, which started in September 2016. The numerical simulations in this study were performed in the Industrial and Biological Multiphysics Laboratory, Institute for Computing, Information and Cognitive Systems (ICICS), under the supervision of Prof. Dana Grecov.

Chapters two, three, and four of the thesis are versions of the published articles. A version of Chapter 2 has been published in the Liquid Crystals journal [Arash Nikzad, Abozar Akbari & Dana Grecov (2021) Rheological properties of discotic nematic liquid crystals: graphene oxide dispersions study, Liquid Crystals, 48:12, 1685-1698] and was also presented in [Liquid Crystal Lubricants for Industrial and Biomedical Applications, 18th World Congress on Rheology (ICR 2020), Rio de Janeiro, Brazil]. I was the lead investigator of this study and was responsible for concept formation, numerical simulations, analysis, validations, visualization, and the majority of the manuscript composition. Dr. Dana Grecov was the supervisory and corresponding author on this project and was involved throughout the project, from concept formation to manuscript submission. Dr. Abozar Akbari, Ph.D. from the Department of Mechanical and Aerospace Engineering, Monash University, Australia, led the experimentations and was involved in the experimental part of the manuscript composition.

Chapter 3 is a version of the article published in Fluids journal [Arash Nikzad, Somesh Bhatia, Dana Grecov. (2022) Simulations of Graphene Oxide Dispersions as Discotic Nematic Liquid Crystals in Couette Flow Using Ericksen-Leslie (EL) Theory. Fluids 7:3, pages 103.]. I was the lead investigator and responsible for conceptualization, methodology, modelling and validation, formal analysis, and most of the manuscript composition. Dr.Dana Grecov was the supervisory and corresponding author on this project and was involved throughout the project, from concept formation to manuscript submission. Somesh Bhatia was involved in the conceptualization, methodology, and manuscript composition. He simplified the EL theory to study the Couette flow of GO dispersion. The coefficients obtained from the previous article, chapter two, were implemented in this article's equations to study the rheology of GO dispersion.

Chapter 4 is a version of the article already published in the Liquid Crystal journal [Arash Nikzad, Dana Grecov (2022) Dynamics of Chiral Liquid Crystals Between Cylinders

using Landau-de Gennes Theory, Liquid Crystals]. I was the lead investigator of this study and was responsible for concept formation, numerical simulations, analysis, validations, visualization, and manuscript composition. Dr. Dana Grecov was the supervisory and corresponding author on this project and was involved throughout the project, from concept formation to manuscript submission.

Table of Contents

List of Tables

List of Figures

Acknowledgments

I would like to thank the people without whom I would not have been able to complete this Ph.D.

First of all, I would like to express my special appreciation and gratitude to my supervisor, Prof. Dana Grecov, for the support, guidance, encouragement, and patience during my Ph.D. study. Dr. Dana Grecov has been indeed a tremendous mentor for me, and I appreciate the thoughtful comments and recommendations on all the articles and this dissertation. Moreover, I would like to thank my supervisory committee members for their time and guidance.

I would also like to thank my parents, who devoted their lives to me for their kindness and unwavering belief in me, my wife for endless patience, constant support, and of course, for all the late nights and early mornings. Without her support, this would not be possible. Thank you for being my best friend. I owe you everything.

Dedication

To my lovely parents – Zarafshan and Mohammad

&

To my life - Sara

1) Chapter 1: Introduction

1.1 Background

Liquid crystallinity defines a state between a crystal solid and a liquid. Liquid Crystals (LCs) respond to macroscopic force fields such as shear force [1], [2]. LC molecules can diffuse and flow like liquids [3]. LCs keep the orientational order of solids with no positional order (Figure 1-1). The orientational order implies that the molecules point in the same direction. In contrast, the positional order implies that the molecules' center of mass tends to lie on lattice points [4].

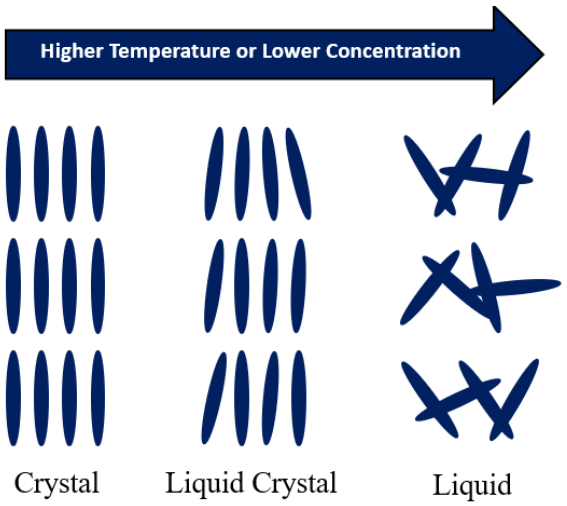

Figure 1-1 Transition from solid crystal to liquid crystalline mesophase showing positional order in crystals, orientational order in liquid crystals, and isotropic liquid

There are multiple ways of classifying LCs [4]–[6]. They can be classified based on shape, phase, or even order. Categorizing LCs based on their shapes leads to Calamitic (Rod-like) and Discotic (Disk-like). Two of the most basic molecules arrangements are nematic and smectic (Figure 1-2). Nematics have a high degree of long-range orientational order, meaning that the molecules are aligned in a preferred direction. Nematics possess the orientational order but no positional order, while smectics possess both orientational and one-dimensional positional order (i.e., layer-like). In the chiral LCs, the orientation direction rotates along a

helical axis. It is possible to have nematics and smectics in a chiral shape. The chiral nematic phase is also known as the cholesteric phase [4].

LCs can be mainly divided into thermotropic and lyotropic by the formation process. Thermotropic LCs show a phase transition by temperature, while the phase transition in lyotropic is obtained by a change in concentration (Figure 1-1).

The nematic phase is one of the most basic liquid crystalline symmetries shown in Figure 1-2 (a). The averaged preferred direction of the molecules axis is designated by a director "**n**", which has no tail or head. Nematic liquid crystals (NLCs) are anisotropic ordered fluids with a principal orientation. Most of the NLCs are uniaxial, while due to molecules' rotation restrictions, some thermotropic and lyotropic NLCs show biaxiality [7]. The degree of orientation in a uniaxial nematic can be defined by the order parameter S, which is zero in the isotropic state and approaches unity for perfect molecular alignment [4].

Lately, discotic liquid crystals (DLCs) have drawn considerable interest [8]. DLCs became important not only in energy and charge migration in self-organized systems but as functional materials for applications like photovoltaic solar cells, gas sensors [7], and lubricants [9]. Examples of nanoparticle solutions forming discotic nematic liquid crystals (DNLCs) in specific concentration ranges are Graphene Oxide (GO) aqueous solutions [10], α-Zirconium Phosphates (α-ZrP) [11], and aqueous clay suspensions [12].

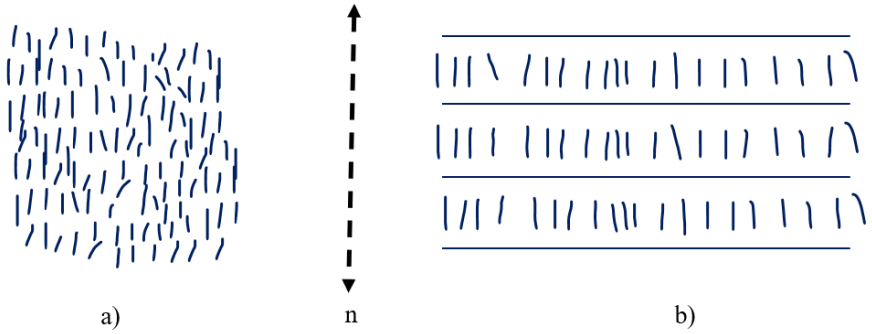

Figure 1-2 Molecular arrangement in a) nematic with orientational and no positional order and b) smectic-A phases with orientational and one-dimensional positional order

Cholesteric liquid crystals (CLCs), the same as NLCs, have a long-range orientational order and no long-range positional order. They exhibit a helical structure with a twist axis

perpendicular to the local molecular director, i.e., a chiral structure. CLCs are defined by two structural parameters: the helical pitch (p) and the twist sense (Figure 1-3). The pitch shows the distance along the axis, which corresponds to a rotation of 360 degrees in the orientation of the molecules, and the twist sense indicates a left- or right-handed helix [13]. In the cholesteric phase, layers correspond to a rotation of 180° of the molecular orientations or a half pitch. Therefore, a periodic twisted pattern exists, depending on the chiral strength.

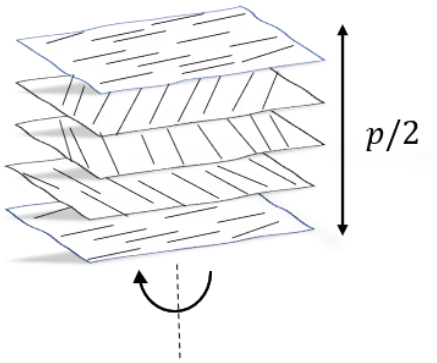

Figure 1-3 Cholesteric liquid crystal pitch in a simple twist showing half pitch and twist direction

Similar to other ordered mediums, LCs might indicate multiple local symmetry breaking or defects. The defects can be points or lines (disclinations) that have also been observed in other studies [14]. Under different flow conditions or material properties, the structure of CLCs can significantly differ from the simple twisted pattern. At a higher concentrated phase, hexagonal patterns could be observed [15]–[17], where the molecules are aligned in a direction with a lateral hexagonal order. However, cholesteric and hexagonal patterns can be seen simultaneously, for example, in a specific range of DNA concentrations [15].

There is a wide range of CLC applications, such as in biological systems like bacterial flagella [18], lubrication [19]–[22], DNA molecules in solution [15], [16], and solutions of nematic mixtures with chiral dopants in modern display devices.

1.2 Motivation

LCs are anisotropic materials with properties of both conventional liquid and solid crystals. Various investigations have been carried out on the rheological properties of LCs and their applications [1], [23], [24].

Existing numerical models for rheological properties are suitable only for rod-like particles [25] and suffer from various limitations, such as microstructure and flow field interdependence.

There are very few data on the viscosities of DNLCs, a nematic phase of disc-like particles [4]. To the best of the author's knowledge, there is no numerical model to calculate the rheological properties of DNLCs, while there are many DNLCs with outstanding mechanical properties, such as GO dispersion. Therefore, a model to calculate the rheological properties of LCs with disc-like particles is necessary to understand their behaviour in different applications.

It is essential to study the flow behaviour of nematic GO dispersion by evaluating the rheological properties to improve the potential of GO dispersions in the industrial-scale fabrication of graphene-based devices. However, the anisotropic features of nematic GO aqueous suspensions result in complex flow properties. The flow behaviour and rheology of nematic GO dispersions are essential for understanding graphene-based devices' top-down and bottom-up fabrication.

GO dispersion has been used in a wide range of applications. Developing a cost-effective synthesis process applicable to the bulk scale is essential to commercialize GOs. Some studies modeled a Couette–Taylor reactor to improve the GO synthesis process [26], [27], where the mixture of an aqueous colloidal suspension of GO and an additive was injected into the gap between the two concentric cylinders, but the flow of GO dispersion between cylinders still needs more investigation.

One of the interesting applications of LCs is applying them as lubricants since the efficiency and durability of journal bearings depend on the lubricant performance. Lubricants affect friction, wear, and load-bearing capacity. Therefore, a suitable lubricant is necessary to reduce the frictional force between the surfaces in mutual contact. Since LCs form an ordered molecular layer close to solid boundaries, which improves tribological performance [25], they are appropriate candidates to be used as lubricants to lower the friction coefficients, wear rates,

and contact temperature of sliding surfaces [28]. Furthermore, many lyotropic LCs exist in living organisms [29], making them worthwhile candidates as bio-lubricants. This research focuses on applying LCs as a lubricant between two cylinders, the preliminary geometry of journal bearings.

To assess the performance of a lubricant over a broad range of operating conditions, one can either conduct numerical simulations, which are fast and economical or perform experimental studies, which are time-consuming and expensive.

Moreover, to the author's knowledge, there is no study on the flow of CLCs between concentric and eccentric cylinders to investigate their structure and performance as a lubricant. Although the coupling between the structure of CLCs and the shear, extensional, and rotational flow between cylinders makes the interactions more complex, the simulation of CLCs between cylinders is essential to provide insights into their structure and improve their performance as a lubricant.

1.3 Literature Review

In several studies, the researchers worked on various aspects of the flow of LCs, such as the formation and evolution of LC's texture, and proposed analytical/numerical methods to model/simulate the flow of LCs. This study focused on defining a method that calculates the required coefficients for the Ericksen-Leslie (EL) and the Landau-de Gennes (LdG) theories in capturing the flow details of LCs and applying those theories to illustrate various aspects of the flow of LCs.

1.3.1 Graphene Oxide (GO):

Graphene, a one-atom-thick, is an exciting multifunctional material with strong mechanical properties, chemical inertness, and a vast surface area [30], [31]. Due to the exceptional properties of Graphene, it was used in numerous applications such as ultracapacitors, biosensors, nanocomposites, and transparent devices [32]–[35]. There has been remarkable progress in applying graphene for transparent conductors for LCD screens, and also it was proposed to replace indium-doped tin oxide (ITO) with graphene, as it has higher flexibility and better chemical stability at a lower cost [36]. To make graphene

commercially viable, a three-step process should be considered, which are a) oxidation of graphite to make graphene oxide and then b) sonication-based exfoliation, and then c) subsequent reduction using agents or heat if needed [27]. Among graphene derivatives, GO has attracted significant attention due to the higher processability and the possibility of producing the input raw material [37]. GO indicates a wide range of interactions such as van der Waals, electrostatic, polar, and hydrogen bonding [31]. Due to the negative charge of the oxygenated functional groups, GO flakes can make stable dispersion in aqueous mediums [38], [39].

Increasing the concentration of the anisotropic disc-like GO flakes in water leads to the particles' rotational restriction. As the anisotropic particles' free rotation becomes further hindered, the particles form ordered structures, self-assembling as lyotropic LCs [31], [40], [41]. The study of nematic GO dispersions is a topic of interest due to their ability to form highly-ordered structures that may allow for fabrication on a wide range of scales [31], [42]–[44].

Furthermore, due to the multifunctional properties of graphene-related materials, they have been considered in different studies as self-lubricating solids [45], [46] and as additives in oils or water [47], [48]. GO performance as a water-based lubricant has been evaluated and was shown to effectively reduce the friction and wear of sliding surfaces [49]. Kinoshita et al. [50] and Elomaa et al. [51] investigated the tribological properties of water-based GO suspensions, showing a remarkable improvement in friction reductions and evaluating the protective coating on surfaces. They also showed that the friction coefficient decreased by 57% compared to pure water. Therefore, understanding the rheological and tribological properties of GO and its derivatives in water will have a significant impact in the future.

1.3.2 Methods:

Various studies have been carried out to predict the flow behaviour of LCs [52]–[54]. Some theories describing LC behaviour cannot be applied to practical devices. Mean field theories, which are based on statistical mean-field, explain the average of all the molecular interactions. Onsager and Maier-Saupe's theories [55], [56] were the main theories based on mean field theory, assuming that all interactions are equal. In contrast to the mean-field theory, molecular theories are based on the interaction of all individual molecules or particles, with

some simplifications. As considering that all the molecules in the simulation can be very expensive, a limited number of molecules are used to explain the interaction between molecular and bulk properties of LCs. Molecular dynamics and Monte Carlo methods are popular and common molecular theories. In the molecular dynamics theory, the forces are from the interactions, and based on the interactions, the acceleration and velocity of molecules are calculated. Therefore the location of the molecules are updated in an iterative way based on the molecules velocity/acceleration. While in the Monte Carlo, the position are updated in a pseudo random way and the accept or reject of update is based on some rules. The drawback of this approach is that the dynamic properties of the LCs, such as viscous coefficients, cannot be obtained.

Continuum theories are the most popular approaches to modeling the behaviour of LC materials with considerably large scales. In the continuum approach, the assumption is that the behaviour of the LC molecules and the free energy density, which is a function of various properties, can be described by the director **n** or Q-tensor. EL theory and LdG are the most successful theories considered in this study, and more details are explained in the following sections.

The EL theory uses vector description, more specifically a uniaxial director (**n**), which indicates the bulk of molecules or particles' preferred orientation at any given point in the LC's domain [52], [53]. Nematic LCs typically possess a uniaxial configuration, i.e., a single axis of symmetry exists. Biaxial order, a situation with more than one axis of symmetry, may occur in LCs when the geometry is complex, such as confined surfaces. The uniaxial configuration can be determined by the degree of orientational order, S, where $S = 1$ when all the molecules are oriented in the preferred direction and $S = 0$ when the phase is isotropic. In the nematic phase, the scalar order parameter is between 0.5 to 0.7. S can be calculated based on the angle between each molecule and the nematic director **n**. In the case of biaxiality, we need more than one order parameter, and we should apply the tensor order parameter. Q-tensor, which will be discussed in the next section.

When the flow time scale is slower than the internal time scale such that the orientation dominates the rheology and the scalar order parameter is close to its equilibrium value, the EL theory could be used. For fast flows and short-length scale phenomena, such as defect dynamics, the LdG theory must be used. This theory predicts the behaviour of LCs by

employing an order parameter tensor (**Q**). The evolution of Q (Jaumann derivative) is equal to flow contribution (if there is flow), short range, long range, and chiral contribution (if it is a chiral LC) [57]–[59]. Both theories use modified stress tensors to capture the complex phenomenological aspects of the flow of LCs.

1.3.2.1 The Ericksen-Leslie (EL):

Extensive research has been performed on the theoretical and computational front to understand the morphology of LCs. In this study, one of the theories considered for modelling LCs is a continuum-based approach, the Ericksen–Leslie (EL) theory. Figure 1-4 represents the director and the molecular orientations (which are represented by n) for discotic LCs.

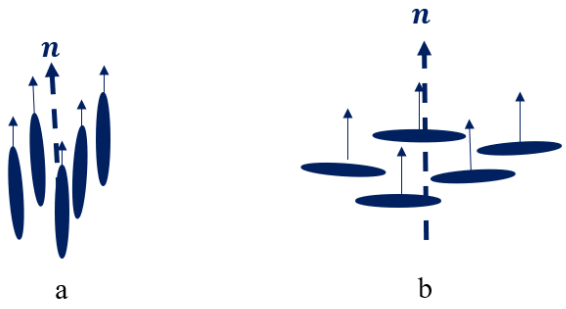

Figure 1-4 Schematic representation of director **n** for (a) Calamitic, which is along the long axis (b) Discotic, which is perpendicular to the long axis

The history of EL dates to 1961, when Ericksen formulated the first dynamic theory [60]. Leslie [61]–[63] formulated the constitutive equation to complete the EL dynamic theory for nematic liquid crystals. This more concise theory considered continuum theory variables like strain tensor rate and vorticity tensor. This theory then became widely accepted to study nematic liquid crystals and was successfully applied in studying LCs in a broad range of applications. Many authors [64]–[68] applied EL to investigate the flow-induced behavior of nematic LCs. Other examples of applying EL are: Cruz et al. [69] applied the theory in a confined region; Jiao et al. [70] investigated the stationary behavior of planar shear flows of nematics; and Han et al. [71] applied EL theory to analyze the behavior of nematic LCs in a 2D confined geometry with tangent boundary condition.

In the EL theory, the modified stress tensor is a function of viscosity coefficients, the director vector, and the velocity gradient. Considering the symmetry of the director and taking it to be of unit magnitude, Leslie simplified the equations based on Ericksen's theory of anisotropic fluids [72]. The constitutive equations were developed by incorporating Frank's theory to model the elasticity of the LCs [73]. The basis of Frank's elasticity coefficients is that LCs tend to resist and recover from distortion, analogous to the tendency of elastic solids to resist strain [73].

The flow behaviour of nematic LCs depends on the magnitude of the reactive parameter, or tumbling parameter λ, which is the ratio of the shear flow-aligning effect and vorticity tumbling effect. The value of the reactive parameter governs whether an LC is flow-aligning ($|\lambda| > 1$) or tumbling ($|\lambda| < 1$). The EL theory has been used to study flow-aligning LCs and tumbling LCs to understand the behaviour at different shear rates [74].

Since LCs are anisotropic viscoelastic materials, different coefficients need to be determined to predict their behaviour. The coefficients in the EL theory should be calculated for rod-like or disc-like LCs and then applied to the stress tensor. The Leslie coefficients in the EL theory are in the constitutive relation derived from the principal equations of EL, i.e., conservation of mass, momentum, and angular momentum.

1.3.2.2 Leslie Viscosity Coefficients:

In the EL theory, the modified stress tensor is a function of rheological properties, and the viscous stress tensor is calculated based on six viscosity coefficients, the Leslie viscosity coefficients, $\alpha_{i;\, i=1:6}$ [60]. The viscous component of the total stress tensor in the LdG theory is a function of three viscosity coefficients, the Landau viscosity coefficients, ν_i [57]. Many studies have found α_i for the rod-like liquid crystalline materials [14], [59], [75]. However, defining a method to calculate α_i and ν_i for DLCs is very important and needed.

The research studies focus on calculating the Leslie viscosity coefficients (i.e., the rheological properties) for rod-like liquid crystalline materials. Kuzuu and Doi [75] presented a microscopic theory for the rheological properties of NLCs for rod-like molecules. They found a microscopic expression for the Leslie coefficients by considering the EL constitutive equation derived from the molecular kinetic equation [75]. Besides, Marrucci [76] predicted the Leslie coefficients for very thin and long rod-like molecules. Larson added the viscous

contributions to Leslie viscosity coefficients using a friction factor [77]. Furthermore, Martins [78] found the Leslie coefficients for different materials in aligning, neutral, and non-aligning flow conditions. Baalss and Hess [79] considered perfectly ordered particles to derive a general expression for the Leslie coefficients' anisotropy.

Noroozi et al. [25] proposed a method to calculate the rheological functions and the viscosity coefficients for lyotropic rod-like LCs. They used Doi [75] and Larson [77] model to find the Leslie viscosity coefficients for nanocrystalline cellulose (NCC) aqueous suspensions.

Grecov and Rey [23] investigated the effect of orientation on the rheology of DNLCs. They mapped the stress tensors from EL and the LdG theory to find the Leslie viscosities and other rheological functions since, in the slow flow, the LdG theory converges to the EL theory [80].

1.3.2.3 Landau-de Gennes (LdG):

The flow of LCs involves the interaction of microstructures, which evolve in time and space, with macro-scale flow properties. To predict the flowing properties of LCs, various continuum models have been proposed to study the behaviour of LCs microstructures and their interaction with the flow [53], [60], [81], [82]. One of the most successful continuum models to predict LCs rheological properties is the LdG theory which has been implemented in different studies [59], [83]–[85]. In the LdG theory, the flow of LCs is predicted by the evolution of a traceless and symmetric second-order parameter tensor (Q) in time [23], [86]–[88]. In this theory, the evolution of microstructure in time is a function of flow contributions and short-range and long-range elasticity. The interaction between microstructure and macro-scale attributes of the flow is implemented by modifying the total stress tensor in Navier-Stokes equations, which is given in [57], [83], [88], [89]. LdG theory has been successfully implemented to predict defect formation, tumbling of achiral discotic, and alignment of liquid crystals in 2D simulations [83], [87]–[90]. For CLCs, an additional term is added to the formulation to consider the helical distortion resulting from the interaction of spatial gradient caused by chiral forces and the elastic terms [91]. The chiral force and the elastic terms at low shear rates prevent the molecules from responding to the flow. While, at higher shear rates, chiral structures form as the result of flow and chiral force competition. Pospisil et al. [84] generated a phase diagram based on the results to show the dynamic behaviour under applied

shear. Noroozi et al. also applied the same theory to show the dependence of shear viscosity on the shear rate in the CNC dispersions [25].

LCs, possess an elastic and viscous response to external stress. The coupling between the director and the velocity field results in strong non-Newtonian flow behaviour. Due to this coupling, LCs exhibit significant dynamical responses under shear flow, such as shear banding and molecular tumbling [87], [92], [93]. This is more prominent in the CLCs, where the twisted arrangement of the director can increase viscosity under shear flow in the direction of its helix, i.e., permeation [94]–[96]. In permeation, when a CLC is under an imposed flow in the direction of its helix axis, the viscosity can increase more than 100 times compared to the same material in the isotropic phase [96]. Fadda et al. [97] investigated the dynamics of a quasi 2D isotropic droplet in a cholesteric liquid crystal medium under symmetric shear flow. They found that the dynamics depend on the magnitude of the shear rate, the anchoring strength of the liquid crystal at the droplet interface, and the chirality. Zhang et al. [98] numerically considered NLCs confined in cylindrical cavities with strong and weak homeotropic anchoring conditions and showed that the elastic constants affect the director alignment in chiral structures with strong homeotropic anchoring conditions.

Furthermore, CLCs under shear flow were studied for low Ericksen numbers [85], and the dynamics of chiral responses were classified. Venhaus et al. [85] simulated the alignment dynamics of CLCs using the LdG. They showed that the rods form a structure resulting from the combination of tumbling and cholesteric phases for high shear rates as flow and chiral forces compete. Wiese et al. have also computationally studied the morphological changes of CLCs in a Poiseuille flow and found that at low pressure gradients, the chiral structure remains unchanged [99].

1.3.3 Application of LCs as Lubricant:

In order to increase the energy efficiency of the systems with rubbing surfaces, we need to reduce energy dissipation from friction and wear. Machines and devices with two solid surfaces in sliding motion, need lubricants to lower friction and the contact temperature and prevent wear. Understanding the physics behind applying lubricant between surfaces helps optimize their performance and save more energy. Developing efficient lubricants is of great technological and economic importance as it can save 1% of the gross national product (GNP).

The molecular structure of the lubricant directly influences the system's tribological performance as the structure of molecules can react with the sliding surfaces, performing as an antiwear and friction-reducing lubricant. The idea of applying LCs as a lubricant or additive goes back around 30 years ago [5], [100]. However, in recent studies, there has been significant progress in studying LCs as a lubricant. Cheng et al. [101] studied how friction force and LCs' molecular orientation are related in a confined geometry. It was shown that a higher shear velocity results in a better alignment of the molecules and, consequently, a reduction in the friction force. The simulation of LCs as lubricants between concentric or eccentric cylinders, the preliminary geometry for journal bearings, has also received significant attention [1], [23], [24], [102]. Noroozi and Grecov investigated the rheological behaviour of nematic LCs between concentric cylinders [24] and eccentric cylinders [83]. They showed that the liquid crystalline materials form an ordered molecular layer close to solid boundaries, improving the tribological performance and making them suitable candidates for application as lubricants.

Applying different computational methods to study the flow between concentric and eccentric cylinders with a small gap size, which is the preliminary geometry for journal bearings, was the topic of several studies [59], [83], [103]–[107]. However, the flow of viscoelastic fluids, specifically CLCs, between eccentric rotating cylinders needs investigation. Challenges such as the numerical setup of complex flow between two cylinders, which includes shear, rotational and extensional flow, and convergence in small to moderate gaps between the cylinders, make the numerical study of viscoelastic effects of the flow between eccentric cylinders difficult. Li [108] simulated the flow between eccentric cylinders with different viscoelastic constitutive equations. Results indicated that viscoelasticity enhanced the lubricant pressure field and positively affected lubrication performance, i.e., lower friction and wear and higher load-bearing capacity. Grecov and Clermont [109] applied the stream-tube method to simulate unsteady flows of non-Newtonian incompressible fluids between concentric and eccentric cylinders and found significant viscoelastic effects in moderate and narrow gaps.

1.3.4 Introduction to COMSOL

The software used for this study is COMSOL Multiphysics, a commercial Finite Element Analysis (FEA) simulation package. COMSOL uses Galerkin finite element method

to discretize the continuum domain into several finite pieces and to find the solution at nodal points. The LdG equations of LC's microstructure coupled with the Navier-Stokes equations in COMSOL. The system of partial differential equations can be discretized by the FEA, which results in a linear system of equations. COMSOL solves this system of equations using the MUltifrontal Massively Parallel sparse direct Solver (MUMPS). MUMPS uses multifrontal LU decomposition to generate upper triangle and lower triangle matrices. Moreover, the time steps in the transient analysis in COMSOL are calculated using multi-order Backward Differential Formula and variable damping factor based on CFL numbers for fluid mechanic related problems.

1.4 Summary of the Gaps in Existing Knowledge

As discussed earlier, viscosity coefficients are limited to rod-like LCs, and a method is required to calculate DNLC's viscosity coefficients. Finding meaningful values for the viscosity coefficients required in the EL theory and the LdG theory for DLCs is essential.

Although the shear rheology of aqueous nematic GO dispersions forming DLC has been recently investigated for shear rates up to 1000 s^{-1} [110]–[112], the prediction and understanding of nematic GO dispersions behaviour under higher shear rates are vital for developing fabrication protocols paired with different liquid- processing techniques.

Besides, it was mentioned that the preliminary geometry of journal bearings is eccentric cylinders, and the flow between two cylinders includes shear, extensional and rotational flow which makes the flow complex. Combining this complex flow with LCs microstructure evolution makes the problem more complex for simulation. There have been studies on the simple shear flow of NLCs and a few more complex flows, but they are mainly limited to rod-like NLCs simulations. As the literature review suggests, there is no study of the flow of CLCs between concentric and eccentric cylinders or preliminary geometry of journal bearings.

1.5 Objectives and Approaches

This study aims to propose a method to calculate the rheological properties of DLCs and predict the behaviour of chiral LCs between cylinders to reveal both microstructure and macroscale attributes of the flow of LCs. The main objectives of the study are as follows:

- To propose a method to calculate rheological properties for DNLCs:

  An analytical method to calculate the viscosity coefficients of DNLCs is proposed. Using this approach, the viscosity coefficients for a DLC are calculated, and the rheological properties are compared with the experimental results to verify the proposed method. The method is illustrated on nematic GO dispersions as an example of DNLCs. The Landau and Leslie viscosity coefficients are calculated using the proposed analytical method, which can be applied to calculate the stress tensors in the EL and LdG theories to model a DNLC.

- To understand the behaviour of GO dispersion as DNLC using the EL theory:

  As an example of DNLC between concentric cylinders, the flow of GO dispersions is simulated using the EL theory. The Leslie viscosity coefficients calculated using the proposed method are used to calculate the stress tensor in the EL theory. The behaviour of GO dispersions with different concentrations, corresponding to the nematic phase, in a wide range of shear rates, is investigated to obtain the orientation and the viscosity profiles.

- To understand the dynamics of CLCs between cylinders using LdG Theory:

  The behaviour of CLCs between concentric and eccentric cylinders under different flow conditions is investigated using the LdG theory. This theory is implemented using dynamic finite element simulations to solve the evolution of the microstructure of CLCs and couple it with a linear momentum balance equation (modified Navier-Stokes equation) to capture the structure of CLCs. The study focuses on the microstructure formation of CLCs and their performance as lubricants under various chirality strengths (θ), Deborah numbers (De), and eccentricity of eccentric cylinders.

The procedure that is suggested to connect all the objectives and investigate the behaviour of a new LC is as follows:

1. Performing experimental study to calculate the apparent viscosity (Objective 1)

2. Using the proposed analytical method to calculate the alignment angle based on the experimental inputs, such as the size of the LC (Objective 1)
3. Validating alignment angle by comparing with the apparent viscosity from the experimental study (Objective 1)
4. Calculating rheological properties (α_i and ν_i) for the LC from the proposed analytical method (Objective 1)
5. Applying EL theory to simulate the behaviour of the LC in the application of interest (Objective 2)
6. Applying LdG theory in COMSOL to simulate the behaviour of the LC in the application of interest (Objective 3)

1.6 Thesis Layout

Chapter two presents the details of the proposed method to calculate the rheological properties of DNLCs. The results are compared with experimental studies on GO, as an example of DNLCs, to validate the method. The results of this comparison and suggested values for the Leslie and Landau coefficients are presented in this chapter.

Chapter three covers the details of the simulation of GO dispersions between concentric cylinders using EL theory. The Leslie viscosity coefficients calculated in the previous chapter are used to calculate the stress tensor in the EL theory. In this chapter, GO dispersions in the concentration range of 15 mg/ml to 30 mg/ml, where GO dispersion is in the nematic phase, at a wide range of shear rates, are investigated to obtain the orientation and the viscosity profile. The alignment angles of GO dispersions at different concentrations are studied.

Chapter four focuses on the behaviour of CLCs between concentric and eccentric cylinders under different flow conditions using LdG theory. This chapter describes the LdG theory in detail for CLCs. The results of this theory on capturing the microstructure of CLCs under different parameters such as De, chiral strength, and eccentricity ratio are investigated. This chapter shows the hexagonal structure at low De (0.001), where the chiral term is predominant, and the uncoiling twisted pattern of CLCs at higher De.

Finally, in chapter five, a summary of the results is highlighted, followed by a discussion on the potential future research directions.

In the end, the references are mentioned.

2) Chapter 2: Rheological Properties of Discotic Nematic Liquid Crystals: Graphene Oxide Dispersions Study

This chapter's main objective is to propose an analytical method to calculate the viscosity coefficients and various rheological properties for discotic nematic liquid crystals (DNLCs). Using this approach, the viscosity coefficients for a discotic liquid crystal (DLC) are calculated. The method has been illustrated on nematic Graphene oxide (GO) dispersions, the most processable derivative of graphene. The Leslie and the Landau viscosities coefficients, the alignment viscosity, the rotational diffusivity, and other rheological properties are calculated as a function of concentration. The Landau and Leslie viscosity coefficients can be used for stress tensors calculations in the EL theory and the Landau-de Gennes theory to model DNLC.

The results of this method are compared with the experiment conducted by the co-author of the our article [102] at the Department of Mechanical and Aerospace Engineering at Monash University. The experiment aimed also to find the range of concentrations corresponding to the GO aqueous suspensions' liquid crystalline phase.

The remainder of the section is organized into four sections: section two describes the analytical method used to calculate the Leslie and Landau viscosity coefficients, section three discusses the experimental method, the results are presented in section four, and section five concludes the paper.

2.1 Analytical Method

In the EL model, a modified stress tensor couples the microstructure and macro-scale attributes of LCs and is a function of six viscosity coefficients (α_i), the director vector (**n**), and the velocity gradient tensor. The total stress tensor, **t**, is the summation of the isothermal static deformation, $\mathbf{t^0}$, and the hydrodynamic one, $\mathbf{t}'$ [113]

$$t' = \alpha_1 nnnn : D + \alpha_2 nN + \alpha_3 Nn + \alpha_4 D + \alpha_5 nn.D + \alpha_6 D.nn \qquad 2.1$$

where **D** is the symmetric part of the velocity gradient tensor ($D = 1/2[\nabla v + (\nabla v)^T]$, **N** is the rotation rate of $\boldsymbol{n}$ relative to that of the background fluid and equals $N = \dot{n} - n.\omega$, where $\dot{\mathbf{n}}$ is the substantial time derivative of **n** and **ω** is the antisymmetric part of the velocity gradient ($\omega = 1/2[\nabla v - (\nabla v)^T]$).

The total stress tensor for liquid crystalline materials in the LdG theory includes a viscoelastic stress tensor, which is the summation of the symmetric viscous stress tensor and an elastic stress contribution [88]. The symmetric viscous stress tensor, $\mathbf{t^V}$ is a function of three viscosity coefficients (ν_i), the order parameter tensor (**Q**), the rate of deformation tensor (**A**), and the unit tensor (**I**) and is given by [23]:

$$t^V = \nu_1 A + \nu_2 \left\{ Q.A + A.Q - \frac{2}{3}(Q:A)I \right\} + \nu_4 [(A:Q)Q + A.Q.Q + Q.A.Q + Q.Q.A + \{(Q.Q):A\}I] \qquad 2.2$$

Grecov [23] proposed an approach to calculate ν_i as a function of Leslie viscosity coefficients, α_i, scalar order parameter, S, and shape factor, β, by mapping the stress tensors of LdeG and EL theories. The three viscosity coefficients $\tilde{\nu_1}, \tilde{\nu_2}$ and $\tilde{\nu_4}$, can be calculated as below:

$$\tilde{\nu}_2 = \frac{\left[\tilde{\alpha}_5 - \frac{\beta S}{3}\left(2 + S - \frac{S^2}{2}\right) - \frac{S\beta^2}{3}(4 - S - S^2)\right]}{S}$$

$$\tilde{\nu}_4 = \frac{\tilde{\alpha}_1 + \beta^2 S^2\left[\frac{8}{9}(1 - S) + \frac{S^2}{12}\right]}{2S^2} \qquad 2.3$$

$$\tilde{\nu}_1 = \tilde{\alpha}_4 + \left(\frac{2\tilde{\nu}_2 S}{3}\right) - \left(\frac{\tilde{\nu}_4 S^2}{3}\right) - \frac{4}{9}[\beta^2(1 - S - \frac{S^2}{4})$$

where $\tilde{\alpha}_i$ and $\tilde{\nu}_i$ are dimensionless values of the Leslie viscosities and the Landau viscosity coefficients and are defined by dividing them by the characteristic viscosity, $\bar{\eta}$, and are equal to $\alpha_i/\bar{\eta}$ and $\nu_i/\bar{\eta}$.

The Leslie viscosity coefficients can be expressed in terms of two main components, elastic and viscous, $\alpha_i = \alpha_i^E + \alpha_i^V$. The prediction of the elastic part of the Leslie viscosities, α_i^E, for DLCs can be computed by the equations for rod-like particles proposed by Kuzuu and Doi [75]:

$$\begin{aligned}
\alpha_1^E &= -2\bar{\eta}\beta^2 S_4 \\
\alpha_2^E &= -\bar{\eta}\beta\left(1 + \frac{1}{\lambda}\right)S_2 \\
\alpha_3^E &= -\bar{\eta}\beta\left(1 - \frac{1}{\lambda}\right)S_2 \\
\alpha_4^E &= \bar{\eta}\beta^2\left(\frac{2}{35}\right)(7 - 5S_2 - 2S_4) \\
\alpha_5^E &= \bar{\eta}\beta\left[\left(\frac{\beta}{7}\right)(3S_2 + 4S_4) + S_2\right] \\
\alpha_6^E &= \bar{\eta}\beta\left[\left(\frac{\beta}{7}\right)(3S_2 + 4S_4) - S_2\right]
\end{aligned} \qquad 2.4$$

where S_i is the order parameter, and λ is the reactive parameter.

Tumbling and flow-aligning nematics can be classified based on the reactive parameter. In this study, the reactive parameter is in the range of flow-aligning, with $|\lambda|>1$. Although the direction of each molecule or particle can be changed suddenly in a shear field due to intermolecular interactions, at high shear rates, the molecules or particles tend to point close to the direction of the flow [4]. For flow aligning DNLCs, the flow alignment angle could be defined as the angle made by the average molecular unit normal and the x-axis [90]. This angle depends on the reactive parameter as $\theta_{al} = 0.5 * \cos^{-1}(\frac{1}{\lambda})$

Larson [77] defined the viscous components of the Leslie viscosities, α_i^V, as below:

$$\begin{aligned} \alpha_1^V &= \frac{\beta_V^*}{0.15}\bar{\eta}S_4 \\ \alpha_2^V &= \alpha_3^V = 0 \\ \alpha_4^V &= \frac{\beta_V^*}{0.15}\bar{\eta}\frac{2}{105}(7 - 10S_2 + 3S_4) \\ \alpha_5^V &= \alpha_6^V = \frac{\beta_V^*}{0.15}\bar{\eta}\frac{2}{7}(S_2 - S_4) \end{aligned} \qquad 2.5$$

where β_V^* is the ratio of viscous to elastic contributions, $\beta_V^* = \xi_{str}D_r^*/KT$; ξ_{str} is the friction factor $\xi_{str} = KT/2D_r$; K is the Boltzmann's constant; D_r is the rotational diffusivity and D_r^* is the rotational diffusivity corresponding to the characteristic concentration c^*, which will be defined later in equation 2.19. The relationship between D_r^* and the averaged rotational diffusivity, $\overline{D_r}$, is used to define $\beta_V^* = 0.15\,\overline{D_r}/D_r$ (for more details, please see [75]).

The Parodi's relation brings down these six Leslie coefficients to five, as follows:

$$\begin{aligned} \alpha_6^E &= \alpha_2^E + \alpha_3^E + \alpha_5^E \\ \alpha_6^V &= \alpha_5^V \end{aligned} \qquad 2.6$$

The Leslie coefficients for DNLCs can be calculated by modifying the previous parameters for discotic materials. The rotational diffusivity, D_r, shows the rotation of the axisymmetric particle and is defined by the Stokes-Einstein equation [114] as below:

$$D_r = \frac{KT}{\eta_0 \widehat{{}^rK_\perp}} = \frac{KT}{6V_p\eta_0 \, {}^rK_\perp} \qquad 2.7$$

where T is the absolute temperature, η_0 is the solvent viscosity, and V_P is the volume of the particle. Rotational diffusivity can be calculated for different shapes based on their material constant, ${}^rK_\perp$. Applying the material constant for disc-like particles ($\widehat{{}^rK_\perp} = \frac{32d^3}{3}$) [114], the rotational diffusivity becomes:

$$D_{r0} = \frac{3KT}{32\eta_0 d^3} \qquad 2.8$$

where d is the diameter of the discs. Therefore, the averaged rotational diffusivity is [115]:

$$\overline{D_r} = \frac{BD_{r0}}{(c\mathrm{d}^3)^2} \qquad 2.9$$

where B is the correction parameter, and 'c' is concentration or number of molecules or particles per unit volume of sample. As mentioned earlier, D_r^* is the value of the rotational diffusivity at the concentration of c^*, transition concentration from isotropic to nematic, which can be found using equation 2. 9 only by replacing 'c' with 'c^*'.

The shape factor, β, is a function of the aspect ratio, p, which for a thin disc with a low aspect ratio ($t \ll d$) equals "-1" and for long rods equals "+1". β is defined as:

$$\beta = \frac{p^2 - 1}{p^2 + 1} \qquad 2.10$$

Order parameters S_2 and S_4 can be obtained using second-and fourth-order Legendre polynomials, P_2 and P_4 for a variable *x*, respectively, are [77]:

$$S_2 \equiv < P_2(x) > \; P_2(x) = \frac{1}{2}(3x^2 - 1) \qquad 2.11$$

$$S_4 \equiv < P_4(x) > \; P_4(x) = \frac{1}{8}(35x^4 - 30x^2 + 3) \qquad 2.\,12$$

According to [75], S_2 and S_4 are functions of non-dimensional concentration, ratio of the sample concentration to the characteristic concentration, $C = c/c^*$, and can be expressed as below.

$$S_2 = 1 - 0.14726C^{-2} - 3.344 \times 10^{-1}C^{-4} - 1.49 \times 10^{-1}C^{-6} + \cdots \qquad 2.\,13$$

$$S_4 = 1 - 0.49087C^{-2} - 2.713 \times 10^{-1}C^{-4} - 1.56 \times 10^{-1}C^{-6} + \cdots \qquad 2.\,14$$

The rest of the terms approaches zero and can be ignored compared to the first four terms.

The equilibrium equation between isotropic (*i*) and nematic phases (*n*) should be employed to define the characteristic concentration for DLCs [55]:

$$c_n + bc_n{}^2\rho = c_i + bc_i{}^2 \qquad 2.\,15$$

where c_i and c_n are isotropic and nematic concentrations, respectively. Parameter 'b' relates to the particle shape, where for disc-like particles is [114]:

$$b_d = (\pi/4)^2 d^3 \qquad 2.\,16$$

Onsager found the following solution for equation 2. 15:

$$bc_i = 3.3399 \;\text{ and }\; bc_n = 4.4858 \qquad 2.\,17$$

The characteristic concentration of DNLCs is between the isotropic concentration and the nematic one where the two phases coexist, $c_i < c < c_n$. Kuzuu and Doi [75] used the

average concentration of isotropic and nematic phases for the characteristic concentration of rod-like LCs. Calculating the characteristic concentration for DLCs in a similar way leads to:

$$\begin{cases} b_d c_i = 3.339 \\ b_d c_n = 4.48 \end{cases} \text{ and } c^* = \frac{c_i + c_n}{2} \qquad b_d c^* = 3.9095 \qquad 2.\ 18$$

Therefore, the characteristic concentration can be expressed as:

$$c^* = \frac{19.91}{\pi d^3} \qquad 2.\ 19$$

Based on the characteristic concentration and the rotational diffusivity, characteristic viscosity, $\bar{\eta}$, can be defined as below [115]:

$$\bar{\eta} = \frac{c^* KT}{2\overline{D_r}} \qquad 2.\ 20$$

The concentration, c, can be obtained by dividing volume fraction (ϕ) by volume of a disc (V) with diameter d and thickness t:

$$c = \frac{\phi}{V} = \frac{\frac{M_f \rho_{sol}}{M_f \rho_{sol} + (1 - M_f) * \rho_{sub}}}{\frac{\pi}{4} d^2 t} \qquad 2.\ 21$$

where M_f is the mass fraction, ρ_{sol} is the density of the solvent and the ρ_{sub} is the substance density.

The reactive parameter, λ, is defined as a function of the order parameter and the shape factor as below [23]:

$$\lambda = \frac{\beta(4 + 2S - S^2)}{6S} \qquad 2.\ 22$$

In this study, the values of the reactive parameter were obtained at different concentrations. This value at each concentration can be obtained by substituting the equilibrium scalar order parameter, S_{eq}, in equation 2.22. It is worth noting that in the EL theory, the scalar order parameter is assumed to remain constant and always equal to its value at equilibrium. S_{eq} is a function of the nematic potential, U, and can be found by the following expression [83]:

$$S_{eq} = \frac{1}{4} + \frac{3}{4}\sqrt{1 - \frac{8}{3U}} \qquad U = 3C \qquad \text{2. 23}$$

Finally, all the required parameters have been modified and can be substituted in equations 2. 4 and 2. 5, to calculate the Leslie coefficients for DNLCs. According to [75], the Leslie coefficients should satisfy the following thermodynamic inequalities to ensure a positive entropy production:

$$\begin{gathered} \alpha_4 \geq 0 \\ 2\alpha_1 + 3\alpha_4 + 2\alpha_5 + 2\alpha_6 \geq 0 \\ 2\alpha_4 + \alpha_5 + \alpha_6 \geq 0 \\ -4\gamma_1(2\alpha_4 + \alpha_5 + \alpha_6) \geq (\alpha_2 + \alpha_3 - \gamma_2)^2 \end{gathered} \qquad \text{2. 24}$$

where γ_1 and γ_2 are the rotational and irrotational torque coefficients, respectively, and are equal to:

$$\begin{aligned} \gamma_1 &= \alpha_2 - \alpha_3 \\ \gamma_2 &= \alpha_5 - \alpha_6 \end{aligned} \qquad \text{2. 25}$$

The Miesowicz viscosities are essential for describing the anisotropic behavior of the LCs and are essential to calculate the alignment viscosity. These viscosities correspond to the director in three different directions and are expressed in terms of the Leslie coefficients [60]:

- $\eta_a = \frac{1}{2}(\alpha_3 + \alpha_4 + \alpha_6)$ [along the flow direction]
- $\eta_b = \frac{1}{2}(\alpha_4 + \alpha_5 - \alpha_2)$ [along the velocity gradient direction]
- $\eta_c = \frac{1}{2}\alpha_4$ [along the vorticity axis]

For discotic nematic particles, the following inequalities hold [79]:

$$\eta_b < \eta_c < \eta_a \qquad 2.\ 26$$

For high enough shear rates and flow aligned LCs, the viscous force overcomes the elastic effects and aligns all the molecules or particles close to the flow direction. Therefore, the alignment viscosity or the apparent viscosity corresponding to the flow alignment direction is [23], [116]:

$$\frac{\eta_{al}}{\bar{\eta}} = \frac{\eta_a}{\bar{\eta}} + \frac{1}{2}\left(\frac{\eta_b}{\bar{\eta}} - \frac{\eta_a}{\bar{\eta}}\right)\left(1 - \frac{1}{\lambda}\right) + \frac{\alpha_1}{4\bar{\eta}}\left(1 - \frac{1}{\lambda^2}\right) \qquad 2.\ 27$$

2.2 Experimental Method

GO was synthesized from natural graphite (SP-1, Bay Carbon, MI) by the well-known modified Hummers method [117] and was then dispersed in water by sonication for two hours, following by the cleaning process and eliminating un-exfoliated graphite oxide by centrifugation. Scanning electron microscopy (SEM) revealed that the GO flakes had an average size of 1 ± 0.2 μm (Figure 2-1).

To investigate the sheet size of the GO, low concentration solution of GO was imaged by SEM to find the flake size distribution. Figure 2-2 shows that the GO sheets' size has a distribution from less than 0.5 μm to over 2 μm, more than 87% ranges between $0.5 - 2$ μm.

X-ray photoelectron spectroscopy (XPS) was performed to study oxygenated functional groups on the GO sheets. XPS measurements were performed with an Omicron ESCA Probe (Omicron Nanotechnology, Taunusstein, Germany) using monochromatic AlKa

radiation (hm = 1486.6 eV); Kratos Vision v 2.2 software was used to perform curve fitting and to calculate the atomic concentrations.

Nematic phase GO dispersion in different concentration (0.25 mg/ml, 7.5 mg/ml, 10 mg/ml, 15 mg/ml, 20 mg/ml, 30 mg/ml, 40 mg/ml and 60 mg/ml) were prepared by dehydration of dilute GO, with the aid of superabsorbent polymer (cross-linked polyacrylate copolymer-based hydrogel beads, Demi Co., Ltd, China) (followed the protocol explained in [31]). The dehydration process was repeated to achieve the desired (Figure 2-3). The concentration of the dispersions was determined by an Ocean Optics USB4000 UV-vis spectrometer, measuring the absorbance at 230 nm (using a quartz cuvette, Starna Cells Pty. Ltd, Australia).

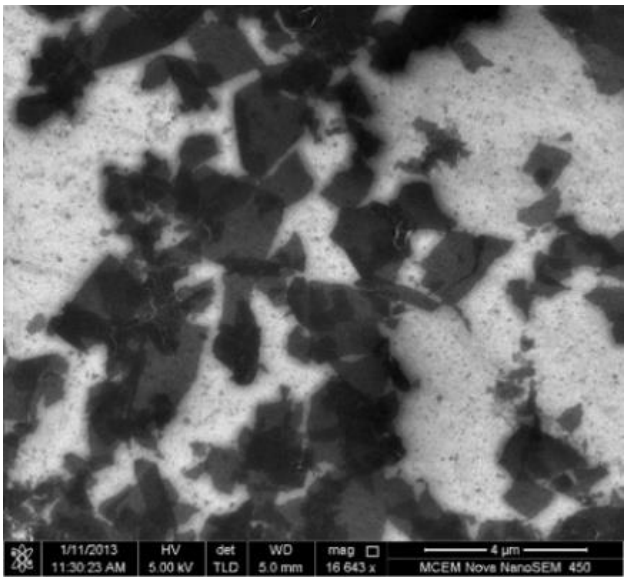

Figure 2-1 SEM image of GO sheets showing the average size of 1 ± 0.2 µm

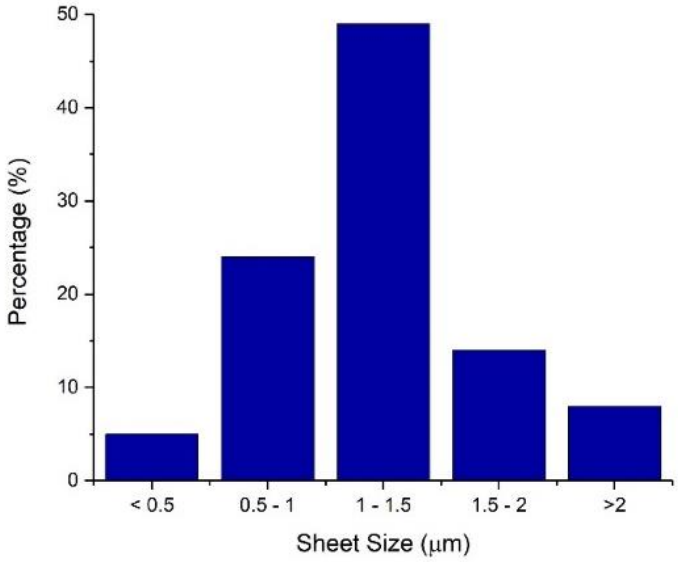

Figure 2-2 GO sheet size distribution which shows that most of the GO flakes are between 1 and 1.5 μm

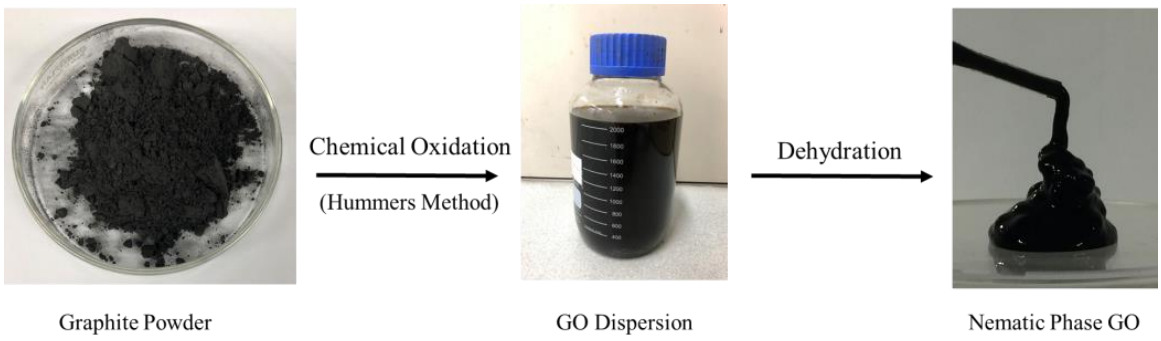

Figure 2-3 Steps of synthesizing nematic phase GO from graphite powder to nematic GO

Polarised light microscopy imaging was carried out using a Leica DM IRB microscope with an LC-PolScope (LPS) Abrio imaging system from CRI Inc. [31], to detect phase transition and nematic GO dispersion.

HAAKE MARS II Rheometer (Thermo Electron Corporation, Germany) was used to experimentally investigate the rheological behavior of a range of concentrations of aqueous

GO dispersions in the nematic phase. Using a Peltier system and a thermostat HAAKE Phoenix II, the temperature inside the cone-plate was fixed to 22.00±0.01 °C. The experiments were obtained using a titanium coated cone-plate with a 60 mm diameter, a cone angle of 1°, and 2 ml dispersions with a constant gap of 0.041 mm. Zero-shear viscosity was evaluated by measuring the GO dispersions' viscosity at a shear rate of 0.001 s^{-1}. Each data point was obtained by using three different samples and at least five measurements.

2.3 Results

2.3.1 Experimental

The collected XPS survey spectra, together with the peak area percentages revealed that the synthesized GO contains only carbon and oxygen with an atomic ratio of C/O about 2.13 (Figure 2-4).

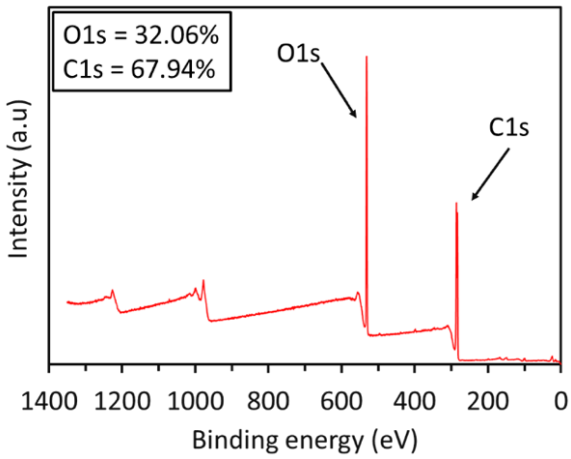

Figure 2-4 XPS survey spectrum of the GO, with the corresponding peak areas percentage and C/O ratio in the inset.

C1s and O1s XPS spectra of graphene oxide are shown in Figure 2-5. Curve fitting of the C1s and O1s spectra was performed using a Gaussian-Lorentzian peak shape after performing a smart background correction. The C1s spectra in Figure 2-5a has two prominent peaks at 284.9 eV and 287.1 eV, which can be fit to 285.2, 287.1, and 288.2, assigned for the C-OH, C=O, and O=C-OH functional groups in the GO sheets, respectively. It is notable that

most structural models of graphene oxide also include an epoxide group (C-O-C), which should have C1s binding energy similar to C-OH [118]. The binding energy at 284.8 is also assigned to the C-C and C-H bonds. Information provided by analysis of the O1s spectra Figure 2-5b can complement the information provided by analysis of C1s spectra, whereas the O1s peak at 530.6 eV can be assigned to contributions from C=O and O=C-OH groups and OH groups.

The formation of LC phases in GO dispersion was experimentally characterized by studying the deflection of light by GO dispersion, as the anisotropy of such phases results in light being refracted in two different directions. This presents as birefringence under polarised light and can be seen using a polarised light microscope [1], [31], [40], [119]. Polarized light imaging technique has been widely used for order parameter characterization of molecules and particles [119] as well as GO sheets in liquids [1], [120] or solid-state films [31], [121]. At very low concentrations of GO dispersion (Figure 2-6a), 0.25 mg/ml, no birefringence is observed due to the random orientation of the sheets in the medium; however, as the concentration of GO dispersion increases to the point where an NLC phase is formed, birefringence within images of light scattering appears (Figure 2-6). The fully nematic phase GO dispersion can be seen at a 15 mg/ml concentration and above. The dark and bright brushes in higher concentrations show the typical schlieren texture of the GO dispersion nematic phase. The hue of the images represents the azimuth angles of GO sheets, as depicted by the legend.

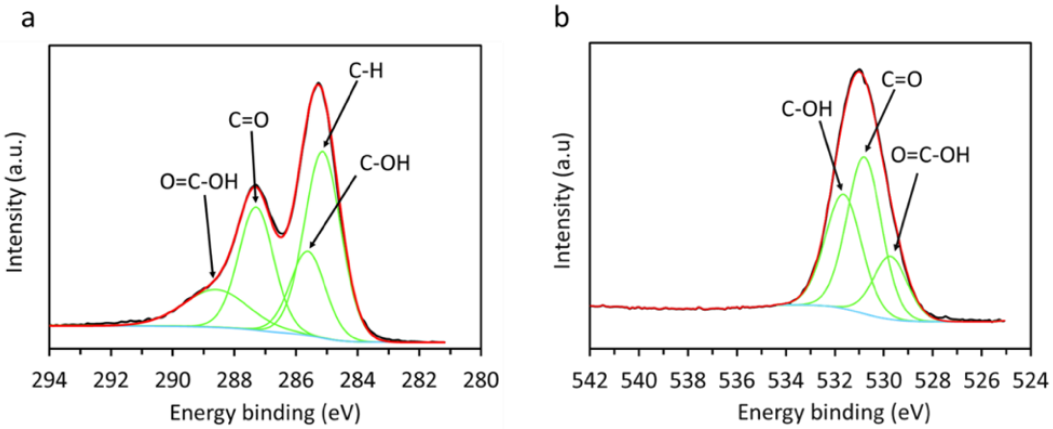

Figure 2-5 XPS spectra for GO (a) C1s peak, (b) O1s peak

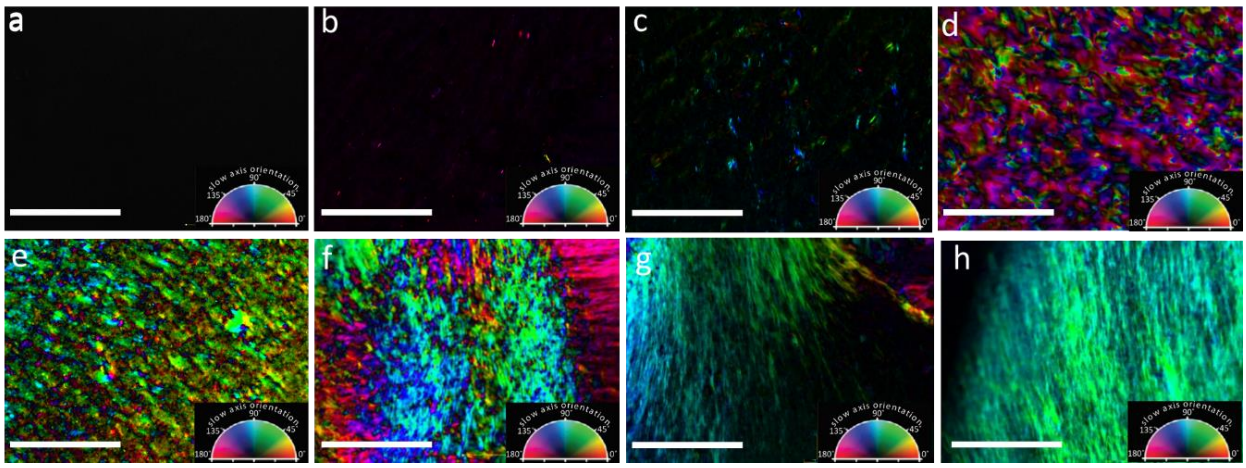

Figure 2-6 Polarized light imaging results of GO dispersion with different concentrations: a) 0.25 mg/ml, b) 7.5 mg/ml, c) 10 mg/ml, d)15 mg/ml, e) 20 mg/ml, f) 30 mg/ml, g) 40 mg/ml, and h) 60 mg/ml

The rheological behavior of a range of concentrations of aqueous GO dispersions was investigated using a standard steady shear test, the deviation in a sample's viscosity under conditions of increasing shear rate. The resultant steady-state shear flow curves showed the behavior of GO flakes dispersed in a liquid medium under applied shear stress. Depending on the sample's concentration, GO dispersions exhibited either Newtonian or non-Newtonian behavior under steady shear (Figure 2-7). At low GO dispersion concentrations of 7.5 and 10 mg/ml, the shear viscosity of the dispersions exhibits Newtonian behavior over a wide range

of shear rates. In contrast, for dispersions with higher concentrations, shear-thinning behaviors are exhibited, where the viscosity of the dispersion decreases with increasing shear rates.

Figure 2-7 Rheology data for seven different concentrations of GO dispersion with a 5% error bar, showing plateau region and constant viscosity for all of the concentrations

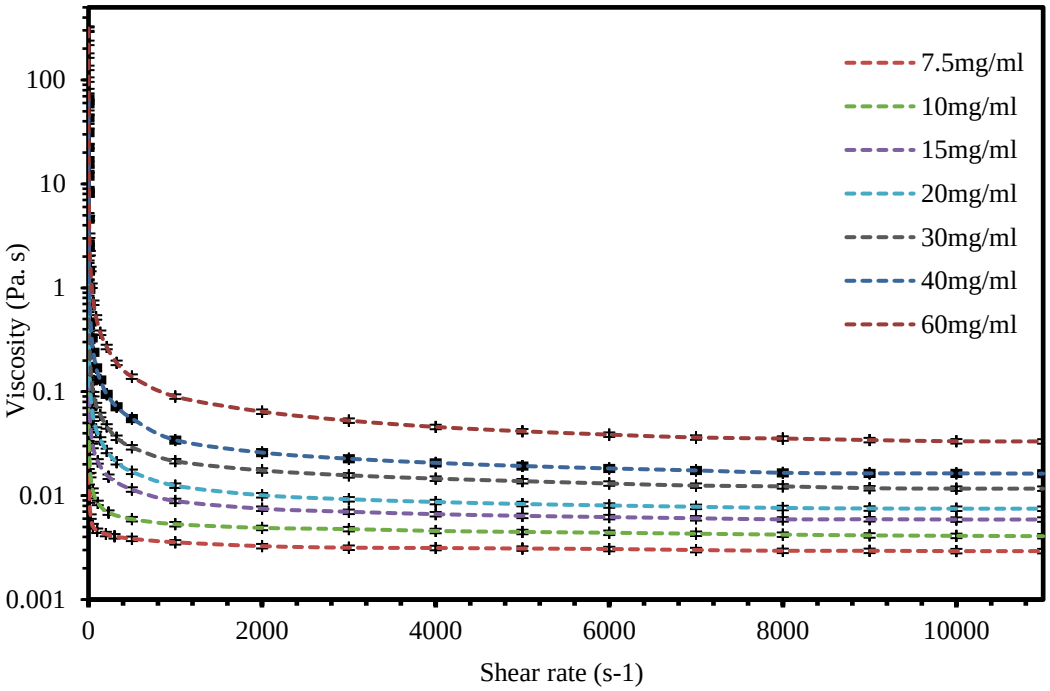

In recent works [111], [112], [122], a variation of viscosity of the nematic GO dispersion has been studied under relatively low shear. However, for low shear rates, the nematic GO dispersions are shear-thinning. In this study, for the first time, very high shear rates (up to 5000 s^{-1}) were applied to the nematic GO dispersions in different concentrations. A plateau region corresponding to an approximately constant viscosity was found for all the concentrations. The value of the viscosity corresponding to this plateau is the alignment viscosity. Therefore, the last measurement at a very high shear rate is considered the viscosity compared with the modelling results. So, four data points, viscosities at the nematic phase (15, 20, 25,30 mg/ml), are compared with the modelling results in the next section.

The experimental data in this study are the average of at least five measurements from three different samples. Table 2-1 shows the average viscosity and the uncertainty from the experimental measurement.

Table 2-1 Experimental values of viscosity at different concentrations

Concentration (mg/ml)	η_{exp} ***(Pa.s)***
15	0.00579±0.00025
20	0.0075±0.000 5
25	0.0097±0.0004
30	0.0119±0.001

2.3.2 Analytical Results

In this section, the calculation of the rheological properties for nematic GO dispersions in a range of concentrations, from 15 to 30 mg/ml, corresponding to the nematic phase, is presented. Since the aspect ratio, $p = t/d$, of GO dispersion particles is in the order of 10^{-4}, the infinitely thin assumption is valid, which leads to $\beta = -1$.

In the analytical model, the correction parameter, B is unknown. Solving the analytical method, the values of B corresponding to the minimum error between the predicted alignment viscosity and the experimental one is obtained. The nematic potential, U, is a function of concentration and the characteristic concentration, c^*, as given by equation 2.23. The characteristic concentration corresponds to the transition from isotropic to the nematic phase, equal to 13.75 mg/ml, using equation 2.19. As the experimental results showed (see Figure 2-6), for a concentration of 10 mg/ml, the GO dispersion is in the isotropic phase, and for a concentration of 15 mg/ml, the nematic phase appears. This indicates that the value of c^* is between 10 and 15 mg/ml. Therefore, the value obtained by equation 2.19 is valid. The values

of λ can be found by calculating the value of S_{eq} for different concentrations, using equation 2.23 (Table 2-2).

Table 2-2 The values of the reactive parameter λ

Concentration (mg/ml)	**λ calculated from S_{eq}**
15	-1.405
20	-1.143
25	-1.049
30	-1.001

Figure 2-8 shows the averaged rotational diffusivity, decreasing continuously as the concentration increases, having the same trend for different correction parameters. As can be seen, different values of the correction parameter directly affect the value of the averaged rotational diffusivity, which leads to different characteristic viscosities (equation 2.20). Hence, various Leslie coefficients (equation 2.4 and equation 2.5) and alignment viscosities (equation 2.26) can be determined based on different correction parameters or averaged rotational diffusivity.

The experimental results (Figure 2-6) showed that the nematic phase starts at a concentration of 15 mg/ml. The predicted alignment viscosity from the analytical method explained in section 2 was compared with the experimental alignment viscosity for the concentrations of 15, 20, 25, and 30 mg/ml. Figure 2-9 shows that for different correction parameters, the analytical results are in perfect agreement with the experimental results.

The experimental alignment viscosities from at least five measurements from three different samples have been compared with the calculated alignment viscosities, as shown in Table 2-3. This table indicates the good agreement between the calculated and the experimental viscosity and also the corresponding numerical parameter, B, at different concentrations.

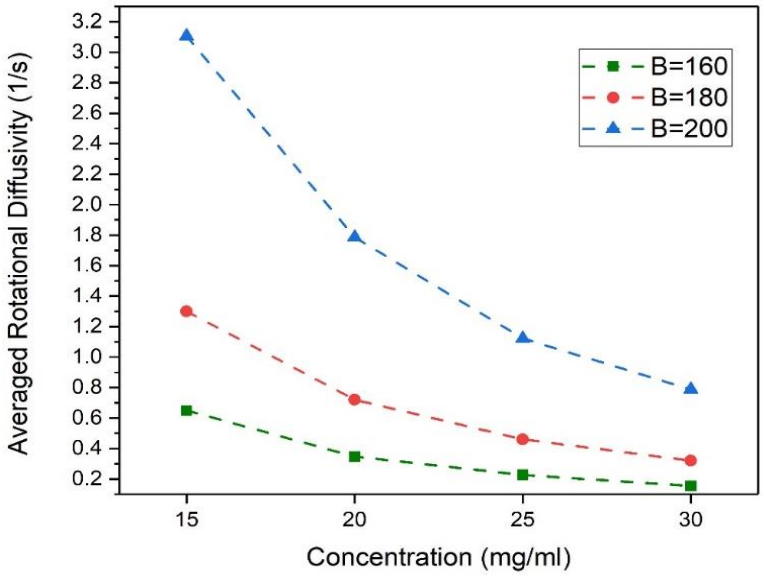

Figure 2-8 Averaged rotational diffusivity as a function of concentration for nematic GO dispersions for different values of the correction parameter B

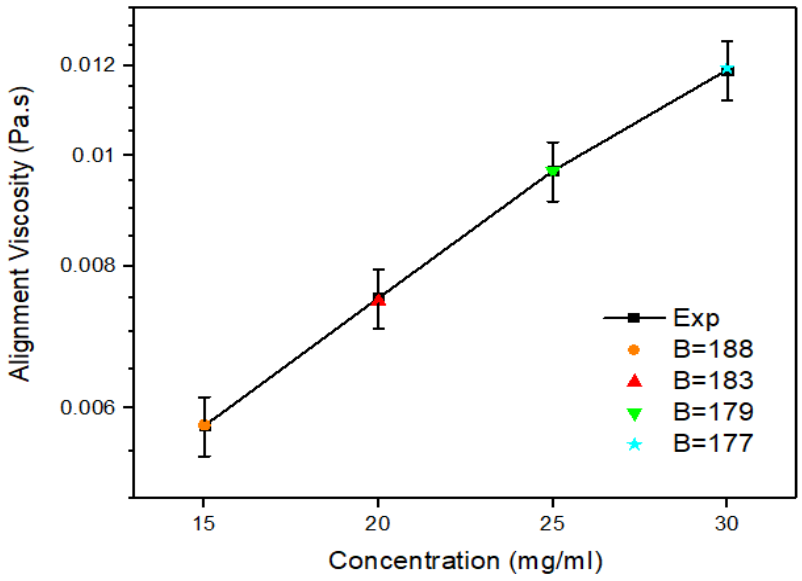

Figure 2-9 Experimental and analytical alignment viscosity of nematic GO dispersions for different values of B with a 5% error bar on the experimental data

Table 2-3 Experimental and analytical values of the alignment viscosity for nematic GO dispersions for various concentrations

Concentration (mg/ml)	η_{exp} **(Pa.s)**	(η_{analyt}, B)
15	0.00579±0.00025	(0.0058, 188)
20	0.0075±0.000 5	(0.00745, 183)
25	0.0097±0.0004	(0.0097, 179)
30	0.0119±0.001	(0.01195, 177)

Figure 2-10 shows the Miesowicz viscosities and the alignment viscosity at different concentrations calculated using the analytical method. Each component represents the viscosity in a specific direction. For DNLCs, the highest viscosity corresponds to the director along the flow direction (η_a), and the lowest corresponds to the director along the velocity gradient (η_b).

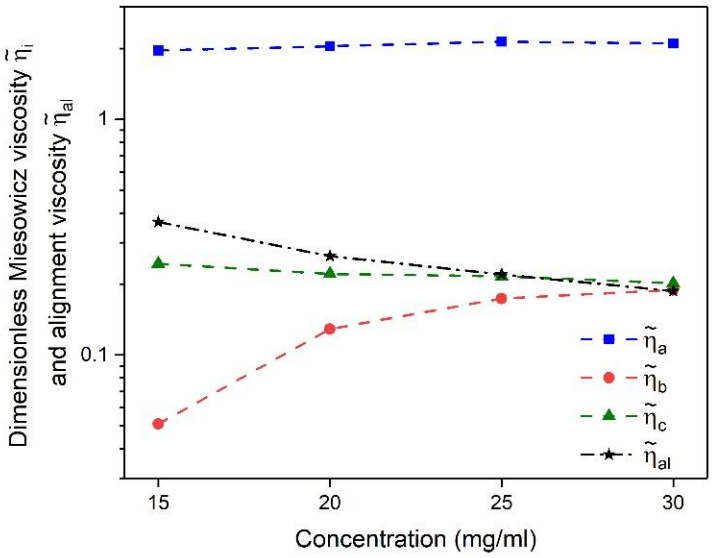

Figure 2-10 Dimensionless Miesowicz and alignment viscosities; each component (a, b, c) represents the viscosity in a specific direction from 15 mg/ml to 30 mg/ml

In Figure 2-11, the dimensionless Leslie coefficients are shown as a function of the concentration. It show that α_3 and α_6 have very close values and are positive for all the

concentrations, while α_1 is negative and possesses the lowest value of the coefficients. It can be seen that the absolute values of the other coefficients (α_2, α_4, and α_5) are very small compared to α_1, α_3, and α_6. The calculated Leslie coefficients are also in agreement with Kroger and Sellers' [123] prediction for flow-aligning LCs where $\alpha_3 \geq \alpha_2 \geq 0$. Since GO dispersion is a DLC, viscosity along the velocity gradient direction should be greater than the viscosity along the vorticity axis which leads to $\alpha_2 \geq \alpha_5$.

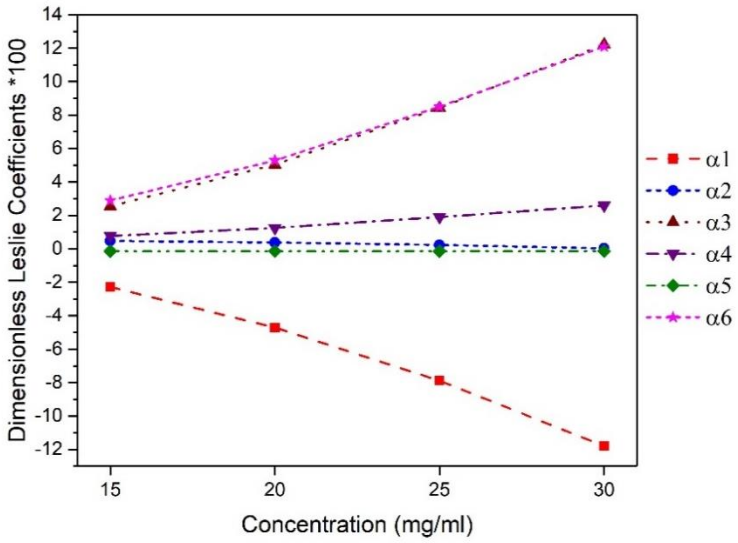

Figure 2-11 Dimensionless Leslie coefficients (*100) of nematic GO dispersion for different concentrations from 15 mg/ml to 30 mg/ml

Table 2-4 Dimensionless Leslie coefficients (*100) of nematic GO dispersions

Concentration (mg/ml)	$\tilde{\alpha}_1$	$\tilde{\alpha}_2$	$\tilde{\alpha}_3$	$\tilde{\alpha}_4$	$\tilde{\alpha}_5$	$\tilde{\alpha}_6$
15	-2.28	0.47	2.54	0.77	-0.14	2.89
20	-4.71	0.38	5.04	1.25	-0.14	5.28
25	-7.88	0.23	8.42	1.9	-0.14	8.5
30	-11.79	0.023	12.21	2.59	-0.1437	12.09

The flow-alignment angle, θ_{al}, depends on the reactive parameter and varies for every concentration. Lower concentrations in the nematic phase possess higher alignment angles

since the degree of order is lower. Figure 2-12 indicates the value of the alignment angle at different concentrations.

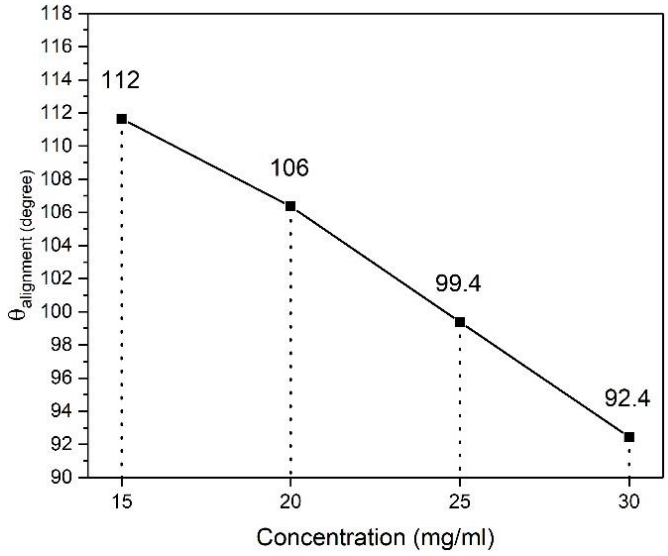

Figure 2-12 The flow-alignment angle at different concentrations from 15 mg/ml to 30 mg/ml

As mentioned previously, to calculate the viscous stress tensor in the LdeG theory, the Landau viscosity coefficients are essential. Figure 2-13 presents the dimensionless Landau viscosity coefficients $\tilde{\nu}_1$, $\tilde{\nu}_2$, and $\tilde{\nu}_4$ and their values are tabulated in Table 2-5.

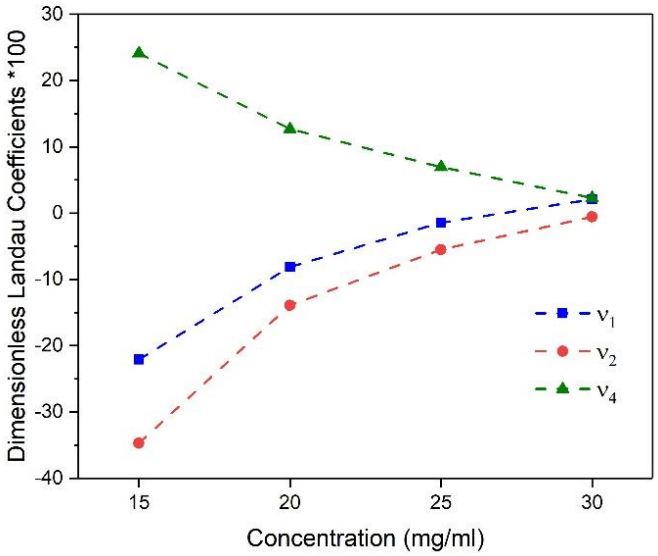

Figure 2-13 Dimensionless Landau coefficients (*100) of nematic GO dispersion for different concentrations from 15 mg/ml to 30 mg/ml

Table 2-5 Dimensionless Landau coefficients (*100) of nematic GO dispersions

Concentration (mg/ml)	$\tilde{\nu}_1$	$\tilde{\nu}_2$	$\tilde{\nu}_4$
15	-22.1	-34.7	24.1
20	-8.1	-13.9	12.7
25	-1.43	-5.49	6.95
30	2.1	-0.54	2.28

2.4 Summary and Remarks

The formation of LC phases in GO dispersions was analyzed by studying the refraction of light by these dispersions. It showed that as the dispersion phase changes from isotropic to anisotropic nematic phase, the birefringence within light scattering images emerges. It was depicted that the nematic GO dispersion started at a concentration above 10 mg/ml and reached to fully nematic phase at 15 mg/ml. Furthermore, the rheological behavior of aqueous GO dispersions was considered for high shear rates up to 5000 s^{-1} to find the value of the alignment viscosity for concentrations between 15 mg/ml and 30 mg/ml where the nematic phase exists. The alignment viscosities for concentrations from 15 to 30 mg/ml and the corresponding numerical correction parameters, B, were calculated using the analytical method and compared

with the experimental results. In this model, the optimal value for the correction parameter, B, was calculated to predict the experimental viscosities. The Leslie and the Landau viscosity coefficients at different concentrations were obtained with the proposed model.

Although the viscosity coefficients for GO suspensions were calculated in this study, the same approach can be used for other nematic GO suspensions (e.g., different size of the particles) or any DNLC. To model other DLCs in the nematic phase and to find the alignment viscosity, the size of the molecules at each concentration in the nematic phase and the alignment viscosity are required as input to the proposed model. The numerical parameter is then used to calibrate the model and find the rheological parameters.

3) Chapter 3: Dynamics of Graphene Oxide Dispersions in Couette Flow Using Leslie-Ericksen Theory

The objective of this chapter is to simulate the flow of graphene oxide (GO) dispersions, a discotic nematic liquid crystal (DNLC), using the Ericksen-Leslie (EL) theory. GO aqueous suspension, as a lubricant, effectively reduces the friction between solid surfaces. The geometry considered in this chapter is two cylinders with a small gap size, which is the preliminary geometry for journal bearings. The Leslie viscosity coefficients calculated in the previous chapter were used to calculate the stress tensor in the EL theory. The behavior of GO dispersions in the concentration range of 15 mg/mL to 30 mg/mL, shown in the recent chapter to be in the nematic phase, was investigated to obtain the orientation and the viscosity profile. The viscosities of GO dispersions obtained from numerical simulations were compared with those from our recent experimental study, and it was observed that the values are within the range of experimental uncertainty. The alignment angles of GO dispersions at different concentrations, the anchoring angles, and a sensitivity analysis are investigated using EL theory.

The organization of the article is as follows. The method, the governing equations, and the numerical setup are described in the next section. The results and discussion are presented in the following sections. Finally, the paper is concluded in the last section.

3.1 Method

In this study, the EL theory is used to analyze the Couette flow of GO dispersions in water as DNLC. The flow in this simulation is steady, incompressible, and isothermal, with no gravity or external field. The EL theory is known to admit multiple solutions based on the anchoring angle (the orientation at the boundaries in case of confined flows) and the flow conditions. Lima and Rey [124] studied the Poiseuille flow of DNLCs and reported the

existence of multiple solutions based on the anchoring angle and the flow conditions. The Couette flow of nematic LCs using EL theory for a fixed velocity profile has been previously implemented [125]. Similar implementations employing a fixed velocity profile have been used to study Poiseuille flow [124], [126] and Jeffrey-Hamel flow [127] as well. The two-dimensional channel flow has been studied for tumbling nematic LCs [128] and for nematic LC flows under the application of magnetic field by [129] . Further, Cruz et al [129] studied the three-dimensional pressure-driven flow under the effect of a magnetic field. Anderson et al [130] studied the two-dimensional channel flow taking the assumption of unidirectional flow. They explained the existence of multiple solutions and the energy requirements for the stability of the flow solutions. Furthermore, shear and pressure-driven flows were studied by [131] under the thin-film approximation.

3.1.1 Ericksen-Leslie (EL) Theory

The constitutive equations in the EL theory combine the effects of anisotropic viscous properties and elasticity present in the LCs through modification of the stress tensor in the Navier-Stokes equations. The EL theory consists of Equations 3.1–3.6, which govern the flow and development of the orientation of LCs. These equations include the mass conservation, linear momentum conservation, angular momentum conservation equations, and the required constitutive equations. The mass conservation equation is as shown below.

$$\rho \nabla \cdot \mathbf{u} = 0 \tag{3.1}$$

where $\mathbf{u}$ is the velocity vector and ρ is density.

The conservation of linear momentum equation is as shown below.

$$\rho \frac{D\mathbf{u}}{Dt} = -\nabla \cdot \left((p + w_F)\mathbf{I}\right) + \nabla \cdot \boldsymbol{\tau} + \mathbf{g} \cdot \nabla \mathbf{n} + \mathbf{G} \cdot \nabla \mathbf{n} + \rho \mathbf{F} \tag{3.2}$$

where p is pressure, w_F is elastic energy, $\boldsymbol{\tau}$ is the viscous stress tensor, **g** is the internal body force vector, **n** is the unit vector representing the orientation, **G** is the force vector due to an external body moment, and **F** is the external body force per unit mass.

The angular momentum conservation equation is represented as shown below.

$$\nabla \cdot \left(\frac{\partial w_F}{\partial \nabla \mathbf{n}}\right) - \frac{\partial w_F}{\partial \mathbf{n}} + \mathbf{g} + \mathbf{G} = \varphi \mathbf{n} \tag{3.3}$$

where φ is the Lagrange multiplier, which simplifies the balance of elastic and viscous torques [132]. The elastic effects of the LCs are modeled using Frank's theory, and the term representing the elastic energy is as shown below.

$$w_F = \frac{1}{2}k_{11}(\nabla \cdot \mathbf{n})^2 + \frac{1}{2}k_{22}(\mathbf{n} \cdot \nabla \times \mathbf{n})^2 + \frac{1}{2}k_{33}(\|\mathbf{n} \times \nabla \times \mathbf{n}\|)^2 \tag{3.4}$$

where k_{11}, k_{22}, and k_{33} are known as Frank's elasticity coefficients for the splay, twist, and bend, respectively [73].

In the present case, the LC orientation is affected only by the hydrodynamic field. The stress tensor due to viscous forces is as shown below.

$$\boldsymbol{\tau} = \alpha_1(\mathbf{nn}:\mathbf{A})\mathbf{nn} + \alpha_2\mathbf{nN} + \alpha_3\mathbf{Nn} + \alpha_4\mathbf{A} + \alpha_5\mathbf{nn}\cdot\mathbf{A} + \alpha_6\mathbf{A}\cdot\mathbf{nn} \tag{3.5}$$

where α_i represents the Leslie viscosity coefficients (i = 1…6), which are unique to each liquid crystalline material. The Leslie coefficients are subject to certain thermodynamic constraints, and these constraints can be found in any introductory material on LCs [5], [132]. The internal body force can be evaluated using the equation shown below.

$$\mathbf{g} = -\gamma_1\mathbf{N} - \gamma_2\mathbf{A}\cdot\mathbf{n} \tag{3.6}$$

The rotational viscosities (γ_i) are defined as $\gamma_1 = \alpha_2 - \alpha_3$ and $\gamma_2 = \alpha_5 - \alpha_6$. In Equations 3.5 and 3.6, the term $\mathbf{N} = \dot{\mathbf{n}} - \mathbf{W}\cdot\mathbf{n}$, which describes the angular velocity of the

director relative to the fluid velocity. $\mathbf{W} = \mathbf{0.5}(\nabla\mathbf{u} - (\nabla\mathbf{u})^T)$ is the vorticity tensor and $\mathbf{A} = \mathbf{0.5}(\nabla\mathbf{u} + (\nabla\mathbf{u})^T)$ is the rate of deformation tensor.

Flow alignment is a property of the LCs, which means that the LC molecules in the bulk of the domain orient at a fixed angle compared to the direction of the velocity, and that it is dependent on the Leslie viscosities and is therefore a material property [4]. The flow alignment angle can be calculated using $\theta_{al} = 0.5\cos^{-1}\left(\frac{1}{\lambda}\right)$, where λ is the reactive parameter and is calculated as $\lambda = -\gamma_2/\gamma_1$. The value of the reactive parameter governs whether a given LC is flow aligning ($|\lambda| > 1$) or tumbling ($|\lambda| < 1$). For discotic LCs, $\lambda < 0$.

3.1.2 Simplified Equations of Couette Flow

The equations for Couette flow in this study are in polar coordinates, which were derived by Atkins and Leslie [125]. As mentioned earlier, r is the radial distance, and θ represents the angle of a given point from the horizontal in the anti-clockwise sense. These equations were used by Noroozi and Grecov [24] to further study different nematic LCs.

Figure 3.1 represents the typical Couette flow geometry. The inner and outer surfaces are at radii R_1 and R_2, respectively. The outer surface is provided with an anti-clockwise angular velocity ω. The enlarged image shows the flow direction along with the orientation θ of a discotic liquid crystal molecule.

Furthermore, the orientation of a discotic LC molecule is shown along with the orientation angle. Equations 3.1 –3.6 can be simplified by choosing the velocity vector u as (0, $r\omega(r)$, 0) and the director n as $(\sin(\theta), \cos(\theta), 0)$. The resulting equations in the dimensionless form are as shown in Equations 3.7 and 3.8.

$$\tilde{f}(\theta)\left[\frac{1}{\tilde{r}}\frac{\partial\theta}{\partial\tilde{r}} + \frac{\partial^2\theta}{\partial\tilde{r}^2}\right] + \frac{1}{2}\frac{d\tilde{f}(\theta)}{d\theta}\left[\frac{1}{\tilde{r}^2} + \left(\frac{\partial\theta}{\partial\tilde{r}}\right)^2\right] + (\tilde{\gamma}_1 + \tilde{\gamma}_2\cos 2\theta)\frac{\tilde{r}}{2}\frac{\partial\tilde{\omega}}{\partial\tilde{r}} = 0 \qquad 3.7$$

$$\frac{1}{\tilde{r}}\frac{\partial}{\partial\tilde{r}}\left[\tilde{r}^3\tilde{g}(\theta)\frac{\partial\tilde{\omega}}{\partial\tilde{r}}\right] = 0 \qquad 3.8$$

The terms $\tilde{f}(\theta)$and $\tilde{g}(\theta)$ are defined as shown in Equations (3.9) and (3.10), respectively.

$$\tilde{f}(\theta) = \cos^2\theta + \varepsilon\sin^2\theta \quad (3.9)$$

$$2\tilde{g}(\theta) = 2\widetilde{\alpha_1}\sin^2\theta\cos^2\theta + (\widetilde{\alpha_6} - \widetilde{\alpha_3})\cos^2\theta + (\widetilde{\alpha_5} - \widetilde{\alpha_2})\sin^2\theta \quad (3.10)$$

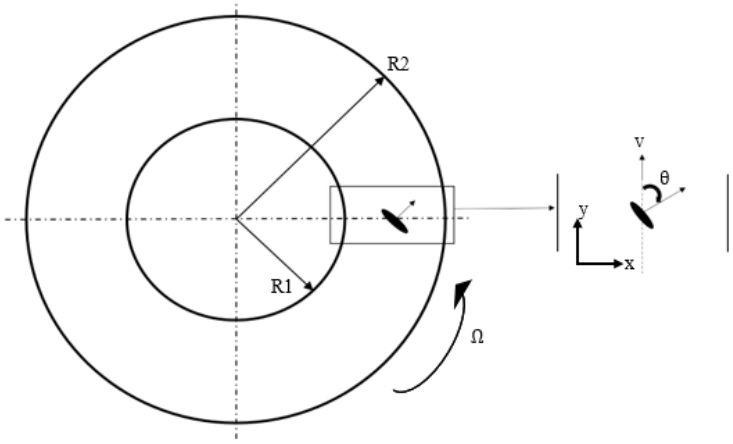

Figure 3-1 Couette flow geometry with R1 and R2 representing the radius of the inner and outer surfaces, respectively.

In Equations 3.7–3.10, the tilde represents that the parameters are non-dimensionalized. The parameter $\varepsilon = {k_{33}}/{k_{11}}$ and the terms are non-dimensionalized as per Table 3-1.

Table 3-1 Non-dimensionalized variables for Couette flow.

$\tilde{\omega}$	$\tilde{r}$	$\widetilde{\gamma_i}$	$\widetilde{\alpha_i}$
$\frac{\omega L^2 \eta}{k_{11}}$	$\frac{r}{L}$	$\frac{\gamma_i}{\eta}$	$\frac{\alpha_i}{\eta}$

In Table 3-1, L represents the difference between the radii R_1 and R_2, and η represents the average of the Miesowicz viscosities η_1, η_2, and η_3. These viscosities are calculated as:

$$\eta_1 = \frac{1}{2}(\alpha_3 + \alpha_4 + \alpha_6)\,; \eta_2 = \frac{1}{2}(\alpha_4 + \alpha_5 - \alpha_2);\ \eta_3 = \frac{1}{2}\alpha_4 \qquad 3.11$$

The three Miesowicz viscosities represent the viscosities of the LCs in a shear flow when the LCs are aligned along the flow direction, along the velocity gradient direction, and the vorticity direction. Figure 3-2 represents these different arrangements.

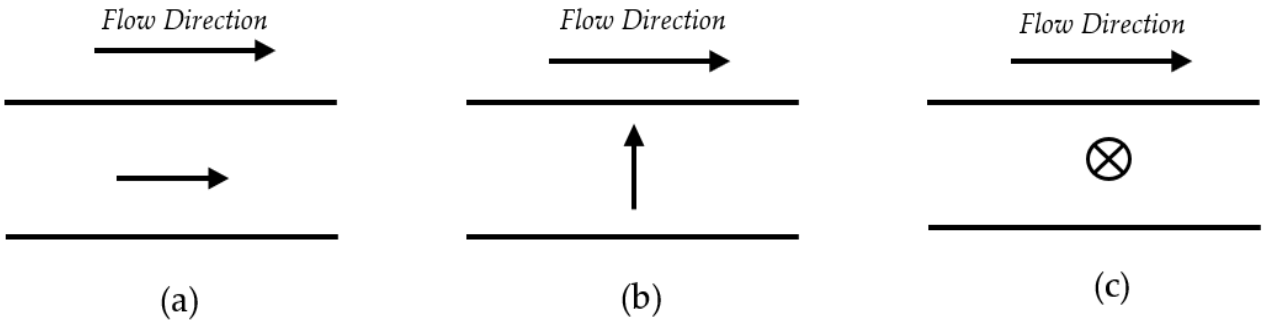

Figure 3-2 Miesowicz viscosities in the direction of (a) velocity, (b) velocity gradient, and (c) vorticity.

Recent developments have been achieved to obtain these anisotropic viscosity coefficients based on the rheological measurements without the application of magnetic or electric fields [25]. Miesowicz introduced a technique to calculate the orientation in three perpendicular directions of the LCs, and thereby, the viscosities measured are termed as Miesowicz viscosities [133]. Based on the applications considered as a motivation for this study, the focus is to study the behavior of flows of LCs. The stable planar solution branches of nematic LCs under the application of shear flow are the in-plane elastic state, the in-plane tumbling–wagging state, the in-plane viscous-driven state, and the in-plane wagging state [134]. There are stable out-of-plane mode solution branches as well [134]. In this study, the focus is on the in-plane elastic state and the in-plane viscous-driven state, and the other solution branches are not discussed here.

3.2 Numerical Setup

In this section, the scheme to solve the EL theory's equations is described. In the EL theory, Equations 3.7 and 3.8 are non-linear, non-homogeneous, and second-order one-dimensional ODEs. They can be solved numerically using either shooting or relaxation methods. Since the LC system is prone to multiple solutions, using the relaxation method to numerically solve these equations is preferable. This method was implemented by Noroozi and Grecov [24] to model the flow of nematic LCs between concentric cylinders, and the solution was computed on a mesh of 500 elements, representing a gap of 10^{-4} m. The mesh independency study was conducted by comparing the change in the orientation profile with mesh refinement. The relaxation method was used to obtain the solution of the boundary value problem of a system of first-order differential equations. Therefore, Equations 3.7 and 3.8 are re-written into a system of four equations, and the variables that are solved are θ, ω, $\partial\theta/\partial r$, and $\partial\omega/\partial r$. In this method, the spatial derivatives of θ and ω are calculated during the solution procedure. The methodology involves selecting an initial guess of the solution, based on which the solution branch is selected. The finite difference form of the equations is obtained to numerically solve the system of equations. The infinity norm of the change in the solution was selected as the convergence criterion, and the value of tolerance was set as 10^{-6}. The solution methodology was previously implemented by Noroozi and Grecov [24], and the scheme was validated using nematic liquid crystalline materials DDA9 and AZA9.

In the governing Equations 3.7–3.10, two sets of material coefficients, namely, Leslie viscosity coefficients and Frank's elasticity coefficients, are present. In order to implement the EL theory, Leslie viscosity coefficients are required. The viscosity coefficients of GO dispersion were obtained using a model based on the rheological data of GO suspensions in water [102] and are shown in Table 3-2. As shown, the coefficients are different for different concentrations of GO. The elastic coefficients of GO suspensions in water are not available in the literature, and therefore, a sensitivity study was conducted to determine the impact of the elastic coefficients on the orientation of the LCs. The values of the elastic coefficients were chosen to have the order 10 pN, which is the value typically observed for Frank's elasticity coefficients of nematic LCs. The results of the sensitivity analysis are presented in the results section for EL theory.

Table 3-2 Dimensionless Leslie coefficients (×100) of nematic GO dispersions at different concentrations.

Concentration (mg/mL)	$\tilde{\alpha}_1$	$\tilde{\alpha}_2$	$\tilde{\alpha}_3$	$\tilde{\alpha}_4$	$\tilde{\alpha}_5$	$\tilde{\alpha}_6$
15	−2.28	0.47	2.54	0.77	−0.14	2.89
20	−4.71	0.38	5.04	1.25	−0.14	5.28
25	−7.88	0.23	8.42	1.9	−0.14	8.5
30	−11.79	0.023	12.21	2.59	−0.1437	12.09

3.3 Results

This section presents the results obtained from the study of Couette flow of GO dispersion. Before the in-depth discussion of the results obtained, it is essential to look at the stability diagram of the LC orientation for discotic LCs, shown in Figure 3-3 [23]. The figure represents the stable and unstable alignment angles of the director. The alignment angle θ_{al} is the angle that the director makes with respect to the primary direction of flow. All the nematic LCs are uniaxial, and the director states cannot be distinguished [5]. Therefore, a 180° rotation of the LC molecule results in the same orientation, which explains both the stable and unstable alignment angles being 180° apart from each other.

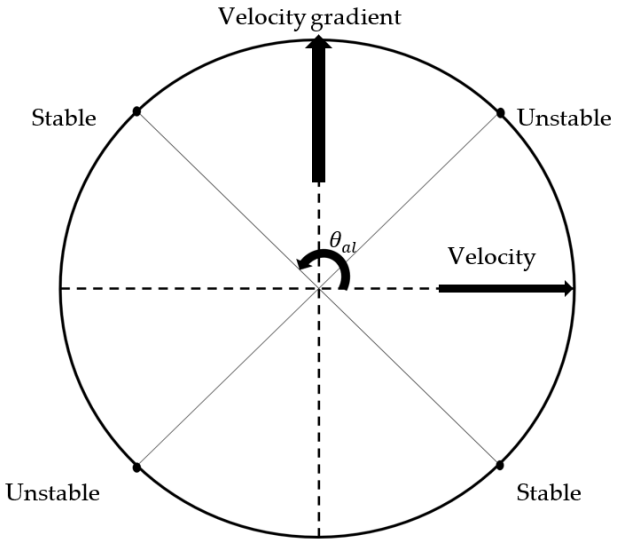

Figure 3-3 Schematic showing the stable and unstable alignment angles for nematic discotic liquid crystals based on the direction of the velocity and the velocity gradient.

3.3.1 Orientation Profile of GO Dispersion

This orientation of LCs depends on the balance of elastic and viscous forces. The elastic forces are dominant at lower shear rates, and then as the shear rate increases, the contribution of the viscous forces increases [135]. At low rotational velocities, due to the dominance of the elastic forces, the orientation in the bulk of the domain is dependent on the anchoring angle. With the increase in the velocity, a larger part of the molecules in the domain reaches the alignment angle. At high shear rates, the viscous forces are dominant, and except for a boundary layer where the orientation is at the anchoring angle, the bulk of the domain reaches flow alignment. This has been previously reported for calamitic liquid crystals [25].

In the present study, the orientation profile of GO dispersion is obtained for different concentrations of GO dispersions at a range of shear rates using the EL theory. The numerically obtained orientation angle in the bulk of the domain is compared with the theoretical value of the alignment angle. Flow alignment of LCs is observed at higher shear rates, and if the orientation in bulk reaches the flow alignment angle, it can be concluded that the numerical solution is validated. Figure 3-4 shows the orientation profile of GO dispersion at a concentration of 20 mg/mL obtained by the EL theory, across the dimensionless gap at different dimensionless shear rates at $\epsilon = 0.5$. This figure shows that the flow alignment is obtained at high shear rates. The anchoring angle in the EL theory is considered as $0.53\pi = 95°$. The choice of anchoring angle is not arbitrary and was selected based on the study performed to compare the numerically obtained viscosity with the theoretical value, and the discussion is provided in the upcoming sections. The initial guess of the orientation was selected as a value between the orientation angle and the anchoring angle. The initial guesses of the velocity and the gradient were set as the typical Couette flow profile. Figure 3-5 demonstrates the orientation profile for all the concentrations obtained by the numerical solution of EL theory at a high shear rate, $\omega = 10^4$. The numerical values of the alignment angle are in good agreement with the theoretically calculated value, which can be obtained as $\theta_{al} = \frac{1}{2} * \cos^{-1}\left(\frac{1}{\lambda}\right)$. Table 3-3 represents the comparison of the alignment value obtained from the numerical solution with the theoretical alignment value of the orientation angle for each concentration. The table confirms that the value of flow alignment angle is obtained for all the concentrations, and the error for the simulation is less than 1% for each concentration.

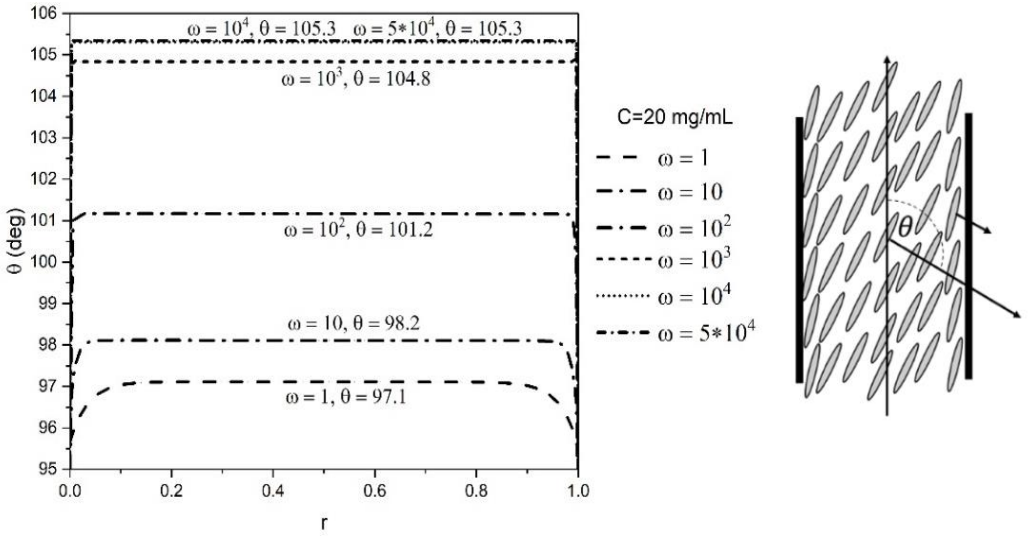

Figure 3-4 Orientation profiles for 20 mg/mL GO dispersion across the dimensionless gap at different dimensionless shear rates using the EL theory.

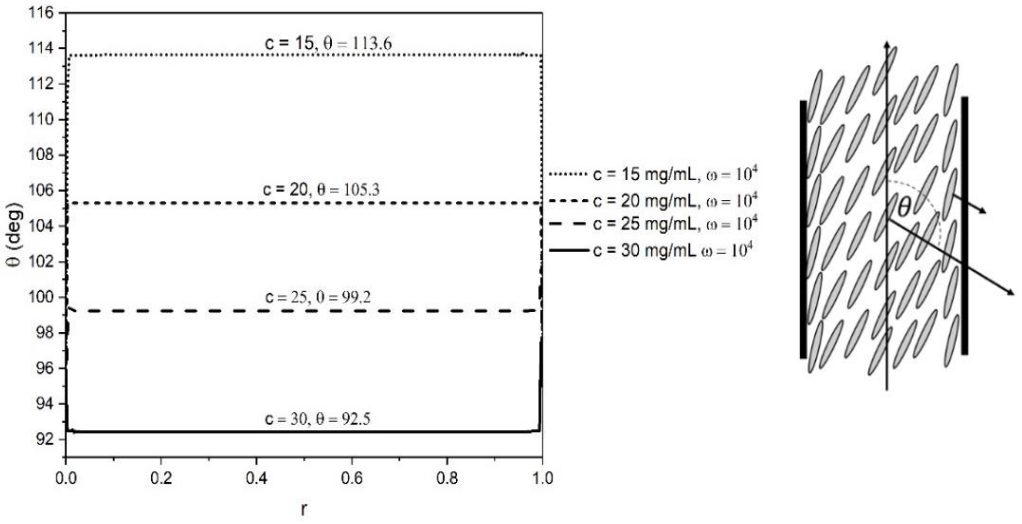

Figure 3-5 Orientation profiles for 15, 20, 25, and 30 mg/mL GO dispersions across the dimensionless gap at different dimensionless shear rates using the EL theory.

Table 3-3 Comparison of theoretical and numerically obtained values for orientation angles at alignment.

Concentration (mg/mL)	**Simplified Theory (deg)**	**Numerical Results from the EL (deg)**	**EL Error (%)**
15	113.3	113.6	0.26%
20	105.3	105.3	0.00%
25	99.3	99.2	−0.10%
30	92.4	92.5	0.11%

3.3.2 Multi-stability and Multiplicity of Solutions

The LCs are prone to having multiple orientation solutions and the solution branch selected depends on the initial guess given to the solver [24], [136]. In this section, studies have been performed to show the stable and unstable branches of the solution. To highlight the difference between the solution branch selection, the anchoring angle was chosen as $\pi/2 = 90°$. The study was performed using $\epsilon = 0.5$. To obtain the stable branch of the solution, the initial guess was above 90°, and to obtain the unstable branch, the initial guess was lower than 90°. The stark contrast between the stable and unstable branches of the solution are highlighted in Figures 3-6 and 3-7. The stable branch solutions are similar to the cases studied in the previous section. At low ω, elasticity is dominant, and as it increases, there is a competition between the elastic and the viscous term to dominate the orientation of molecules. At high ω, a significant part of the domain reaches flow alignment. The elasticity of GO dispersion is a combination of splay, bend, and twist as it is implemented by Frank constants. Dietrich et al. showed that splay and bend elastic constants for lyotropic LCs are similar, while the twist is much lower, which is true for LCs in general [122]. However, to the best of our knowledge, there is no complete set of elastic constants for lyotropic nematics.

In the unstable branch, the solution develops oscillations, and the orientation does not reach the alignment value with the increase in the shear rate. It was observed that the initial guess for the orientational angle can make the results unstable and even diverge at higher ω, which was seen by other authors [24], [124]. An initial guess lower than 90° showed a higher

chance of reaching the unstable solution, while an initial guess above 90° showed a better chance of reaching the stable solution.

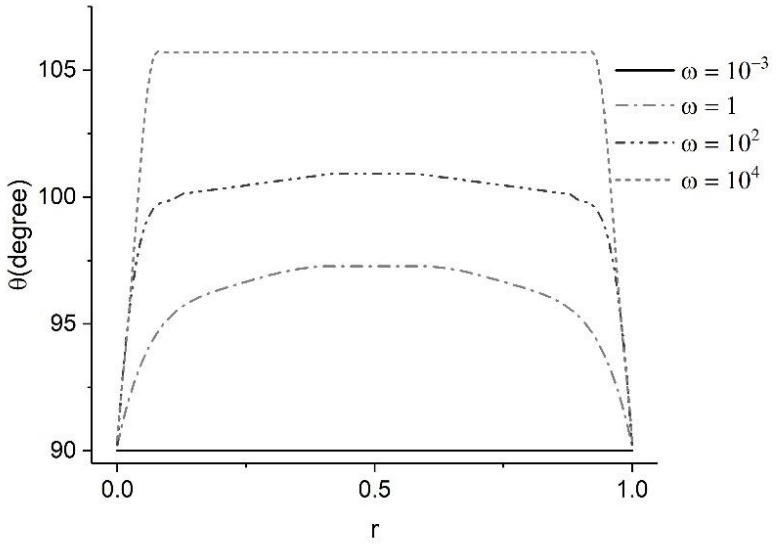

Figure 3-6 Stable solution branch for 20 mg/mL GO dispersion showing the increase in non-dimensionless shear rate results in orientation reaching alignment value.

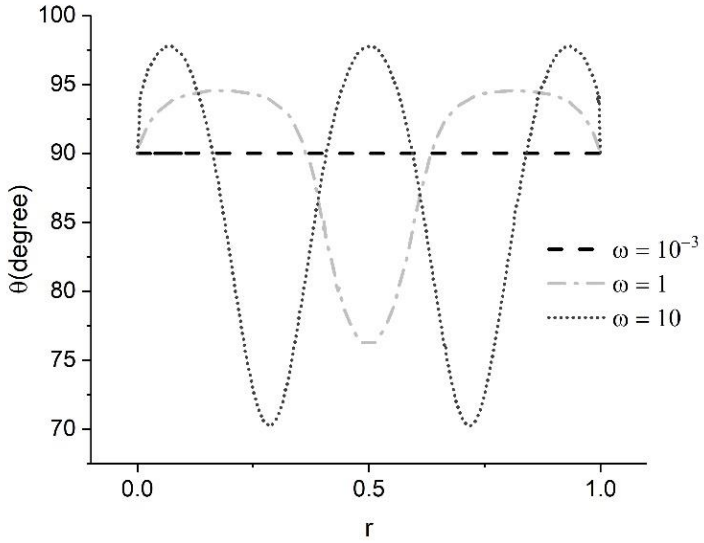

Figure 3-7 Unstable solution branch for 20 mg/mL GO dispersion at different shear rates showing the increase in non-dimensionless shear rate results in oscillations within the orientation.

At low ω, the contribution of the anchoring angle is more significant, and as ω increases, the contribution of the viscous term increases, and unstable alignment is reached. With a further increase in the ω, the fluctuations propagate with higher frequencies.

3.3.3 Viscosity Response of GO dispersion

In the previous section, it was observed that the orientation angle reaches the alignment value at higher shear rates. The next step was to examine the viscosity obtained at different shear rates using the EL theory. In the study, the apparent viscosity is calculated, and it is defined as the viscosity of a Newtonian fluid under the same conditions. The apparent viscosity can be evaluated using Equation 3.12 [125].

$$\eta = \frac{R_2 - R_1}{\int_{r_1}^{r_2} \frac{ds}{g[\theta(s)]}} \qquad 3.12$$

In Equation 3.12, the function $g(\theta)$ is based on the definition shown in Equation 3.10. Equation 3.12 is based on a function for nematic LCs and therefore applies to a discotic LC such as GO. However, its applicability can be easily tested by ensuring that the calculated Miesowicz viscosities match with the values obtained using Equation 3.11. Since the scheme is planar, only the values of η_1 and η_2 can be tested for. Tables 3-4 and 3-5 represent the theoretical and calculated values of η_1 and η_2 using the EL theory. To obtain the theoretical value, Equation 3.11 was used, and the value was compared with those obtained from Equation 3.12. η_1 was calculated using the value of orientation set to 90° in the entire domain, and to calculate η_2, the value was set to 180°. It is evident that the difference in values is minimal, which justifies the use of Equation 3.11.

Table 3-4 Comparison of dimensionless theoretical values of η_1 and calculated from the EL at different concentrations.

Concentration (mg/mL)	**η_1 from Simplified Theory**	**η_1 from Numerical Results from EL**	**Difference**
15	1.3737	1.3741	0.03%
20	2.5599	2.5603	0.01%
25	4.1659	4.1659	0.00%
30	5.9493	5.9497	0.01%

Table 3-5 Comparison of dimensionless theoretical values of η_2 and calculated from the EL at different concentrations.

Concentration (mg/mL)	**η_2 from Simplified Theory**	**η_2 from Numerical Results from EL**	**Difference**
15	0.036416	0.036535	0.32%
20	0.161637	0.161637	0.00%
25	0.338584	0.336735	−0.55%
30	0.516128	0.5140956	0.90%

In this study, the effect of anchoring angles at different concentrations was investigated. Figure 3-8 shows that at lower shear rates, the anchoring angle results in different viscosity values, while at higher shear rates, the anchoring angle effect becomes less significant. Different anchoring angles do not affect the value at flow alignment. However, at low shear rates, the anchoring angle affects the value of viscosity. For all the concentrations, the viscosity values at a higher shear rate converged to their respective experimental values. Higher anchoring angles led the viscosity to be closer to the experimental values but had a numerical limitation. The anchoring angles corresponding to the viscosity values closest to the experimental results [102] at concentrations of 15, 20, 25, and 30 mg/mL are 114, 117, 118, and 118 degrees, respectively. Figure 3-9 represents the viscosity variation for GO dispersion at different anchoring angles from the EL theory. It is evident that the increase in concentration results in a higher viscosity at flow alignment.

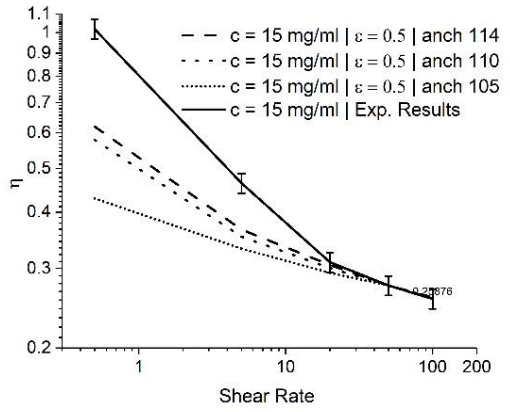

(**a**)

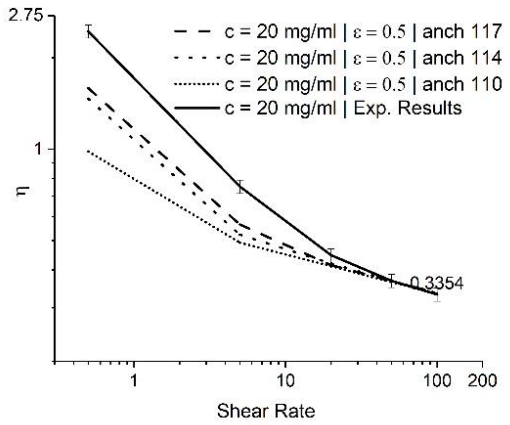

(**b**)

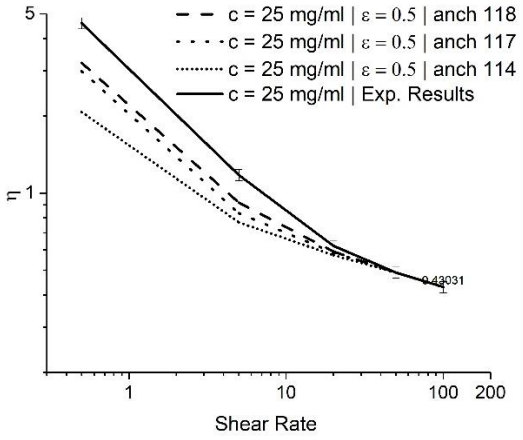

(**c**)

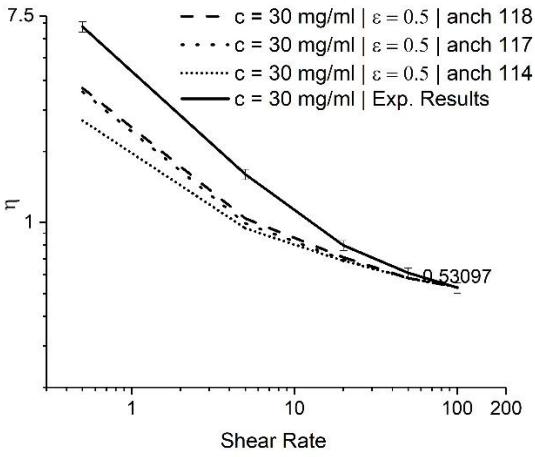

(**d**)

Figure 3-8 Dimensionless viscosity vs. shear rate at different anchoring angles for ϵ = 0.5 at a)15, b)20, c)25, and d)30 mg/mL concentrations using the EL theory.

The results from the numerical simulation using the EL theory have been compared with the experimental viscosities, as shown in Table 3-6, which indicates the excellent agreement at different concentrations.

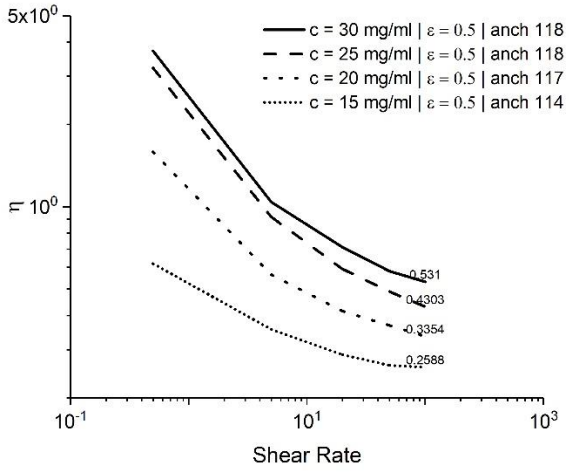

Figure 3-9 Dimensionless viscosity vs. shear rate obtained at different concentrations for $\epsilon = 0.5$ at different anchoring angles using the EL theory.

Table 3-6 Comparison of the dimensionless experimental values of alignment viscosity and calculated from EL at different concentrations.

Concentration (mg/mL)	$\boldsymbol{\eta_{exp}}$	$\boldsymbol{\eta_{EL}}$
15	0.2568 ± 0.0885	0.2588
20	0.3319 ± 0.0221	0.3354
25	0.4303 ± 0.0177	0.4303
30	0.5288 ± 0.0044	0.5310

Both observations can be explained based on the Miesowicz viscosities and the orientation angle in the domain. It was shown that when the orientation angle is 90°, the value of viscosity is expected to be equal to η_1, and when the value of orientation angle increases towards 180°, the viscosity can be expected to be closer to η_2. From Tables 4 and 6, it can be understood that value of η_2, along with the value of the alignment angle, results in increasing values of viscosity when the concentration increases. Similarly, the trend of a higher anchoring

angle resulting in a higher viscosity can be explained by the orientation in the domain becoming closer to the orientation representing η_2.

The shear-thinning behavior has previously been reported for flow-aligning nematic LCs and GO suspensions [122], [136], [137]. Choi et al. [136] and Adnan et al. [138] investigated the viscosity of GO suspensions for shear rates up to $10\ s^{-1}$ and showed that it increased for different concentrations of GO dispersion from the isotropic to discotic phase. Giudice and Shen [138] explored GO aqueous suspensions viscosity further, considering the higher shear rate of $10^2 s^{-1}$, and showed that the shear-thinning behavior becomes more noticeable at higher concentrations. Tesfai et al. [139] investigated the rheology of GO suspensions in the higher range of shear rates (up to $500\ s^{-1}$) for various concentrations (from 0.05 g/L to 0.5 g/L). They showed that at high shear rates, the shear-thinning behavior of the viscosity is followed by a shear-independent region (plateau). The viscosity behavior of GO suspensions from these studies is qualitatively consistent with our results. The quantitative differences between our study and other studies are due to different factors, such as dimensions and the size distribution of the GO sheets.

3.3.4 Sensitivity Analysis of Frank's Elasticity Coefficients

As mentioned previously, there is no literary source available containing the elasticity coefficients of GO suspensions. Dietrich et al. suggested an extremely low value for k_{22} (twist) and a similar order of magnitude for k_{11}(splay) and k_{33} (bend) [140]. To remedy this, as there is no twist here, a sensitivity analysis was performed using different ratios of $\varepsilon = k_{33} / k_{11}$. The tested values are ϵ = 0.5, 1, and 2, which lie in the range of values typically expected in nematic LCs [127], [141], [142]. GO dispersions at 15 mg/mL with the anchoring angle of $0.53\pi = 95°$ were studied. It is important to note that the value of k_{22} does not affect the simulations, except for the value of the average of the elastic coefficients and is maintained constant across the test cases. This value only affects the dimensional value of the shear rate. Figure 3-10 represents the variation in the viscosity with the shear rate for the different values of ϵ. It is evident that the changes in ϵ do not change the overall trend for viscosity, and the final value of alignment viscosity is the same.

The next step is to examine the changes that the ratio causes in the orientation. It is known that at higher shear rates, the effect of the elasticity is limited to a boundary layer, while the orientation in the domain is primarily dominated by viscous forces [127]. Figure 3-11. shows the overlap of orientation angles of the LCs close to the boundary from numerical solutions using the EL theory. The orientation profile is compared at different values of ϵ at the anchoring angle $0.53\pi = 95°$ and the same non-dimensional shear rate $\omega = 10^3$. The difference in the profile suggests that the ratio influences the transition from the anchoring angle to the alignment angle.

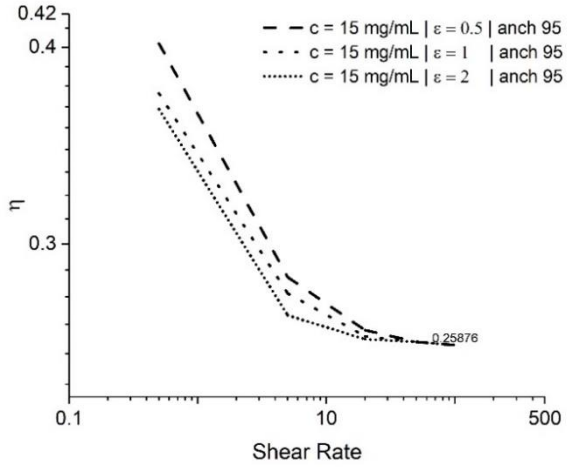

Figure 3-10 Dimensionless viscosity vs. shear rate in the sensitivity study of Frank coefficients using the EL theory

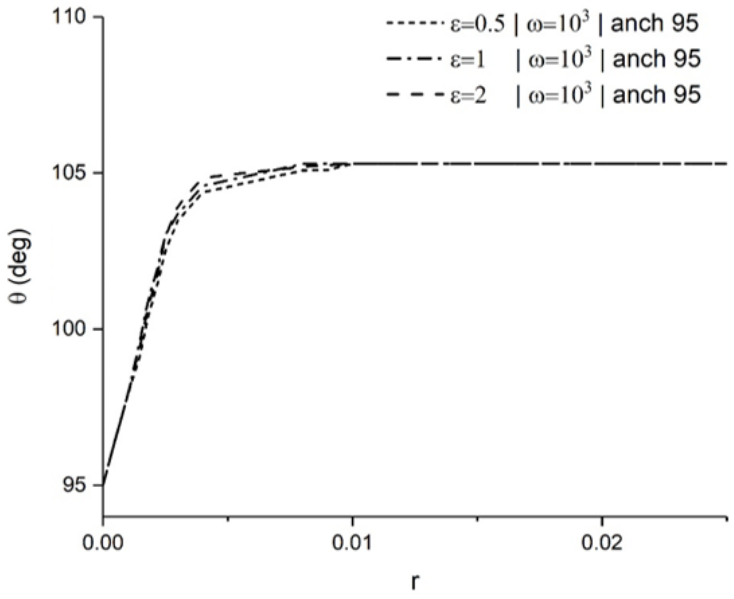

Figure 3-11 Variation in orientation angle for different coefficients of elasticity

3.4 Conclusion

In this chapter, the numerical simulations of GO dispersion as a DNLC between two cylinders with a small gap size, which is a preliminary geometry for journal bearing, were performed to characterize the orientation of flow-aligning particles in GO dispersions and its effect on the viscosity response, i.e., the rheology, In the previous chapter, the Leslie viscosity coefficients of GO dispersions at concentrations of 15, 20, 25, and 30 mg/mL were calculated. At these concentrations, GO dispersions are in the nematic phase of LC. In this chapter, the calculated coefficients were used to perform the simulations using the EL theory. Applying this theory, the behavior of the molecule under a wide range of shear rates, from 10^{-3} to 10^{4}, was studied. In the study, the numerically obtained values of alignment viscosity showed agreement with the theoretical values. The flow alignment behavior of molecules at high shear rates was obtained. Consequently, the shear-thinning behavior of the flow-aligned LCs was observed. The orientation profiles obtained at different shear rates showed that at lower shear rates, the elastic forces dominate the orientation profile of the director, and as the shear rate increases, the viscous forces become predominant and the orientation in the bulk of the domain reaches the alignment angle. The effect of the anchoring angle on viscosity was explained and it was seen that the value of the viscosity at a high shear rate is independent of the anchoring angle. Moreover, it was observed that the solution's stability depended on the initial guess,

which indicates the presence of multiple branches of solutions that the LC could take in the EL theory. Since Frank's elastic constants for GO dispersion were not available in the literature, a sensitivity analysis was performed to determine the effect of different ratios of the elasticity coefficients in the EL theory. The results showed that the alignment angle is not dependent on Frank's elastic constants in the considered range of 0.5 to 2.

4) Chapter 4: Simulation of Chiral Liquid Crystals Between Cylinders

This chapter applies the Landau-de Gennes (LdG) theory to investigate the behaviour of chiral liquid crystals (CLCs) between concentric and eccentric cylinders under different flow conditions. This theory is implemented in dynamic finite element simulations to solve the evolution of the microstructure of CLCs and couple it with linear momentum balance equation (modified Navier-Stokes equation) to capture the structure of CLCs. The study focuses on the microstructure formation of CLCs and their performance as lubricants under various chirality strengths (θ), Deborah numbers (De), and eccentricity of eccentric cylinders.

This chapter aims to numerically study the rheological and structural behaviour of CLCs between concentric and eccentric cylinders. It compares the structure of molecules, the scalar order parameter, pressure force per unit length (p_i^*), and friction force per unit length (τ_i^*) on the inner cylinder at different flow conditions.

The organization of this article is as follows: first, the LdG theory and the governing equations are presented, followed by the numerical methods for solving the set of governing equations. Then, selected results for the flow of CLCs between concentric and eccentric cylinders are presented. Finally, the conclusions are presented.

4.1 Method

The evolution equation is defined by the traceless and symmetric second-order parameter tensor (Q), describing the microstructure of the LC materials. The tensor order parameter Q can be expressed as [143]:

$$Q = S\left(nn - \frac{1}{3}I\right) + \frac{1}{3}P(mm - ll) \tag{4.1}$$

where I is the second-order unity tensor; S is the first, and P is the second scalar order parameter, defined as $-\frac{1}{2} \leq \mathrm{S} = \frac{3}{2}\mu_n \leq 1$, $-\frac{3}{2} \leq \mathrm{P} = 3(\mu_n + \frac{\mu_m}{2}) \leq \frac{3}{2}$ [88]. Parameters $\mu_n, \mu_m,$ and μ_l are the largest, second largest, and smallest eigenvalues corresponding to the eigenvector n, m, and l of the order parameter tensors, respectively.

To solve the dynamics of LCs along with other equations, the evolution equation is written as follows [143]:

$$\hat{Q} = F(\nabla v, Q) + H^{sr}(\overline{D}_r, Q) + H^{lr}(\overline{D}_r, \nabla Q) + \mathcal{P}(\nabla Q) \tag{4.2}$$

where $\hat{Q}$ is the Jaumann derivatives of Q; F is the flow contribution; $H^{sr}$and H^{lr} are short-range and long-range elasticities; v is the velocity profile; and $\overline{D_r}$ is the averaged microstructural rotational diffusivity. $\hat{Q}$ is defined as:

$$\hat{Q} = \frac{\partial Q}{\partial t} + (v.\nabla)Q - W.Q + Q.W \tag{4.3}$$

where W is the vorticity tensor; and $W = \frac{1}{2}[\nabla v - (\nabla v)^T]$. The flow contribution at the microstructure level depends on Q, shape parameter β, and the rate of the deformation tensor A, where $A = \frac{1}{2}[\nabla v + (\nabla v)^T]$.

Flow contribution (F) in equation 4.2 is defined as:

$$\begin{aligned} F = \frac{2}{3}\beta A + \beta\left[A.Q + Q.A - \frac{2}{3}(A{:}\,Q)I\right] \\ -\frac{1}{2}\beta\{(A{:}\,Q)Q + A.Q.Q + Q.A.Q + Q.Q.A - [(Q.Q){:}\,A]I\} \end{aligned} \tag{4.4}$$

and H^{sr} shows the intermolecular forces and is defined as [57]*:*

$$H^{sr} = 6\overline{D}_r\left[\left(\frac{U}{3} - 1\right)Q + UQ.Q - U(Q{:}\,Q).\left(Q + \frac{1}{3}I\right)\right] \tag{4.5}$$

where I is the unit tensor; and U is the nematic potential [115]. $\overline{D}_r$ indicates the averaged microstructural rotational diffusivity and can be expressed as a function of rotational diffusivity (D_r):

$$\overline{D}_r(Q) = D_r\left[1 - \frac{3}{2}(Q{:}Q)\right]^{-2} \tag{4.6}$$

H^{lr} represents the surface anchoring effects from the wall boundaries to the fluid [57]:

$$H^{lr} = \frac{6\overline{D}_r L_1}{ck_BT}\left\{\nabla^2 Q + \frac{L^*}{2}\left[\nabla(\nabla.Q) + [\nabla(\nabla.Q)]^T - \frac{2}{3}tr\big(\nabla(\nabla.Q)\big)\right]\right\} \tag{4.7}$$

where c represents the concentration of molecules in the LC state; K_B is the Boltzmann constant; T is the absolute temperature; and $L^* = L_2/L_1$ and L_i are the Landau coefficients.

$\mathcal{P}$ in Equation 4.2 is the chiral term and shows the ratio of elasticity to the helical distortions of molecules tending to increase the twist pattern of the directors [85]:

$$\mathcal{P} = (\varepsilon_{mik}Q_{mj,k} + \varepsilon_{mjk}Q_{mi,k}) \tag{4.8}$$

where ε is Levi-Civita symbol; The dimensionless numbers that are important in this numerical study are the Ericksen number (Er), Deborah number (De), and Energy ratio (R) [58]:

$$Er = \frac{cK_BTVh}{6L_1Dr};\ De = \frac{V}{6hD_r};\ R = \frac{cK_BTh^2}{L_1} \tag{4.9}$$

V is the velocity of the inner cylinder; h is the flow characteristic length scale; and D_r is pre-averaged rotational diffusivity [60]. The dimensionless form of $\hat{Q}$ is shown below:

$$\hat{Q} = F + \left(\frac{1}{De}\right) H^{sr} + \left(\frac{1}{Er}\right)(H^{lr}) + \left(\frac{\theta}{Er}\right)\mathcal{P} \tag{4.10}$$

where θ quantifies the ratio of anisotropic distortional elasticity to the isotropic one, which is defined based on the isotropic (L) and the anisotropic ($\mathcal{L}$) long-range length scale:

$$\theta = \frac{L^2}{\mathcal{L}^2} \tag{4.11}$$

The derivation of the equations for non-chiral LCs can be found in [14]. The components of the chiral term ($\mathcal{P}$), from equation 4.8, are as below:

$$\begin{aligned}
\mathcal{P}_{11} &= 2\frac{\partial Q_{13}}{\partial y} \\
\mathcal{P}_{12} &= -\frac{\partial Q_{13}}{\partial x} + \frac{\partial Q_{23}}{\partial y} \\
\mathcal{P}_{13} &= \frac{\partial Q_{12}}{\partial x} - \frac{\partial Q_{11}}{\partial y} + \frac{\partial Q_{33}}{\partial y} \\
\mathcal{P}_{22} &= -2\frac{\partial Q_{23}}{\partial x} \\
\mathcal{P}_{33} &= \frac{\partial Q_{22}}{\partial x} - \frac{\partial Q_{33}}{\partial x} - \frac{\partial Q_{12}}{\partial y}
\end{aligned} \tag{4.12}$$

The total stress tensor τ_t for an LC has three main components: the symmetric component τ_s, where τ_s = viscous (τ_v) + elastic (τ_e); the asymmetric component (τ_a), and the Ericksen stress tensor (τ_{Er}) [57], [88].

$$\begin{aligned}
\tau_t &= \tau_a + \tau_s + \tau_{Er} \\
\tau_v &= \nu_1 A + \nu_2 \left[Q.A + A.Q - \frac{2}{3}(Q:A)I\right] \\
&\quad + \nu_4\{(A:Q)Q + A.Q.Q + Q.A.Q + Q.Q.A \\
&\quad + [(Q:Q)A]I\}
\end{aligned} \tag{4.13}$$

$$\tau_e = ck_B T\left\{\frac{-2\beta}{3}H - \beta\left[H.Q + Q.H - \frac{2}{3}(H:Q)I\right] + \frac{\beta}{2}\{(H:Q)Q + H.Q.Q + Q.H.Q + Q.Q.H + [(Q:Q)I]\}\right\}$$

$$\tau_a = ck_B T\{H.Q - Q.H\}$$

$$\tau_{Er} = ck_B TL_1\{L^*(\nabla.Q)(\nabla Q)^T - \nabla Q:(\nabla Q)^T\}$$

H in the above equations is the summation of short- and long-range elasticity; ν_i are the Landau viscosity coefficients, which can be derived by mapping the stress tensors of the LdG and Ericksen-Leslie models [57].

Furthermore, the dimensionless modified Navier-Stokes equations, i.e. linear momentum balance equation, for an LC can be written as [6]:

$$Re_n.\left[\frac{\partial V^*}{\partial t^*} + (V^*.\nabla^*)V^*\right] = -\nabla^* p^* + \nabla^*.\tau_t^* \qquad 4.14$$

where $V^*$is the dimensionless velocity, $p^*$is the dimensionless pressure, and Re_n is the Reynolds number defined in [6] for LCs. $Re_n = \rho_c Vh/\mu_c$, where ρ_c is a characteristic density, μ_c is the characteristic viscosity of LCs, and h is the difference between the inner and the outer cylinder radii. This Reynolds number adapted to LCs represents the ratio of inertial force to viscous force. The characteristic viscosity of LCs can be defined as $\mu_c = cK_BT/(\frac{V}{h})$. Therefore, by replacing the characteristic viscosity in the Reynolds number we can define $Re_n = \rho V^2/cK_BT$.

The dimensionless total shear stress τ_t^* is ($\tau_{...}^*$ represents the dimensionless total shear stress component):

$$\tau_t^* = \frac{\tau_t}{ck_BT} = \tau_a^* + \tau_e^* + \left(\frac{Er}{R}\right).\tau_\nu^* + \left(\frac{1}{R}\right).\tau_{Er}^* \qquad 4.15$$

The simulations were performed in COMSOL Multiphysics which is based on the Finite Element Method. The governing equations for the LC state were solved using the laminar flow module (SPF) and the PDE general module (G) embedded in COMSOL. The solver for the simulation is the MUltifrontal Massive Parallel sparse direct Solver (MUMPS) with adaptive relaxation factor and variable backward differentiation formula (BDF) for time-stepping and an acceptable relative error of 10^{-6}. The element quality in this study was 0.99 in concentric cylinders and at least 0.83 with approximately 20,000 elements for the whole domain. The mesh independence study of the final solutions was implemented based on standard methods. The numerical domain and boundary conditions are shown in Figure 4-1. The inner cylinder in Figure 4-1 is rotating with a velocity of V. The eccentricity ratio is defined as $[\epsilon/(R_2 - R_1)] \times 100$, where ϵ is the eccentricity and R_1 and R_2 are the inner and the outer cylinder radii.

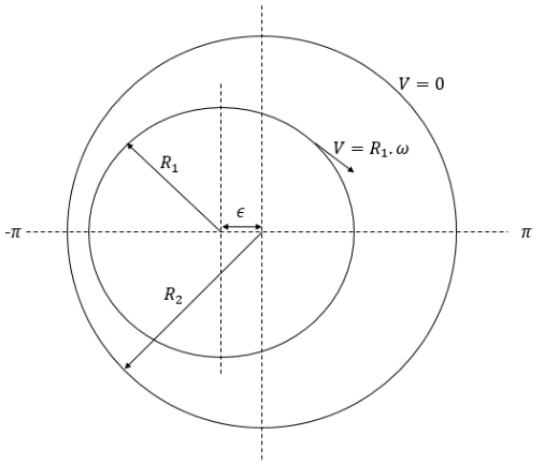

Figure 4-1 Eccentric cylinder boundary conditions with eccentricity of ϵ

$$Q_B = S_{eq}.\begin{bmatrix} \frac{y^2}{x^2+y^2} - \frac{1}{3} & \frac{-x.y}{x^2+y^2} & 0 \\ \frac{-x.y}{x^2+y^2} & \frac{x^2}{x^2+y^2} - \frac{1}{3} & 0 \\ 0 & 0 & -\frac{1}{3} \end{bmatrix} \quad 4.16$$

This boundary condition corresponds to a tangential orientation of molecules to the wall boundaries. The equilibrium scalar order parameter is $S_{eq} = \frac{1}{4} + \frac{3}{4}\sqrt{1 - \frac{8}{3U}}$, where U is the nematic potential that should be at least higher than three to be in the nematic phase [58]. In this study, $U = 4$ was chosen for the numerical simulations.

The equations and simulation setup were validated in a previous study [14]. In the current study, to reduce the computational costs in the concentric cylinders' simulations, only a quarter of the domain was considered instead of the whole domain, and the periodic boundary conditions were applied to the entrance and exit of the quarter domain. Similar mesh configurations for the quarter domain and the whole domain were considered for comparison. Therefore, the total number of mesh elements for the whole domain was four times greater than that of the quarter. In the eccentric cylinders, due to eccentricity, part of the geometry is wider, and part of the geometry is narrower. The eccentricity leads to an asymmetry in flow and velocity subsequent to the asymmetry in geometry. Streamlines are closer to each other in the narrower domain, and the magnitude of velocity is higher, while in the wider area, the streamlines are more distant, and the magnitude of velocity is lower. Hence, we need to consider the whole domain for the simulation.

4.2 Results

This section reviews the dimensionless results of the simulations of CLCs between concentric and eccentric cylinders for microstructure coupled with the flow in COMSOL Multiphysics. Effects of different factors such as De, θ, and eccentricity were investigated at $Re_n = 0.01$ and $\beta = 0.9$. In this study, De ranged from 0.001 to 1, the energy ratio, R, was constant (10^4) and the Ericksen number, Er, ranged between 10 to 10^4. Chiral strength θ, which describes the chirality (i.e., director twisting pattern formation), ranged from 0 (non-chiral) to 70. The eccentricity ratio ranged from 0 to 75%.

4.2.1 Concentric Cylinders

As explained earlier, only a quarter of the full concentric cylinder domain was simulated to reduce the computational cost for the concentric cylinder simulations. Simulation

of a quarter of the cylinders in 2D (i.e., circles), and applying periodic boundary conditions is equivalent to the simulation of the whole domain. Figure 4-2 shows the molecular structure and scalar order parameter contour for the whole domain and a quarter of the full domain. The number of hexagonal structures is the same in the simplified and the full domain. As mentioned earlier, the hexagonal structure was observed in [15]. The structure was also shown in Rey's study [144], which investigated the rheology and flow properties of biological LCs using the EL and the LdG models. Rey showed that at low DNA concentrations, the structure leads to the cholesteric phase, while at higher concentrations, it leads to the hexagonal phase.

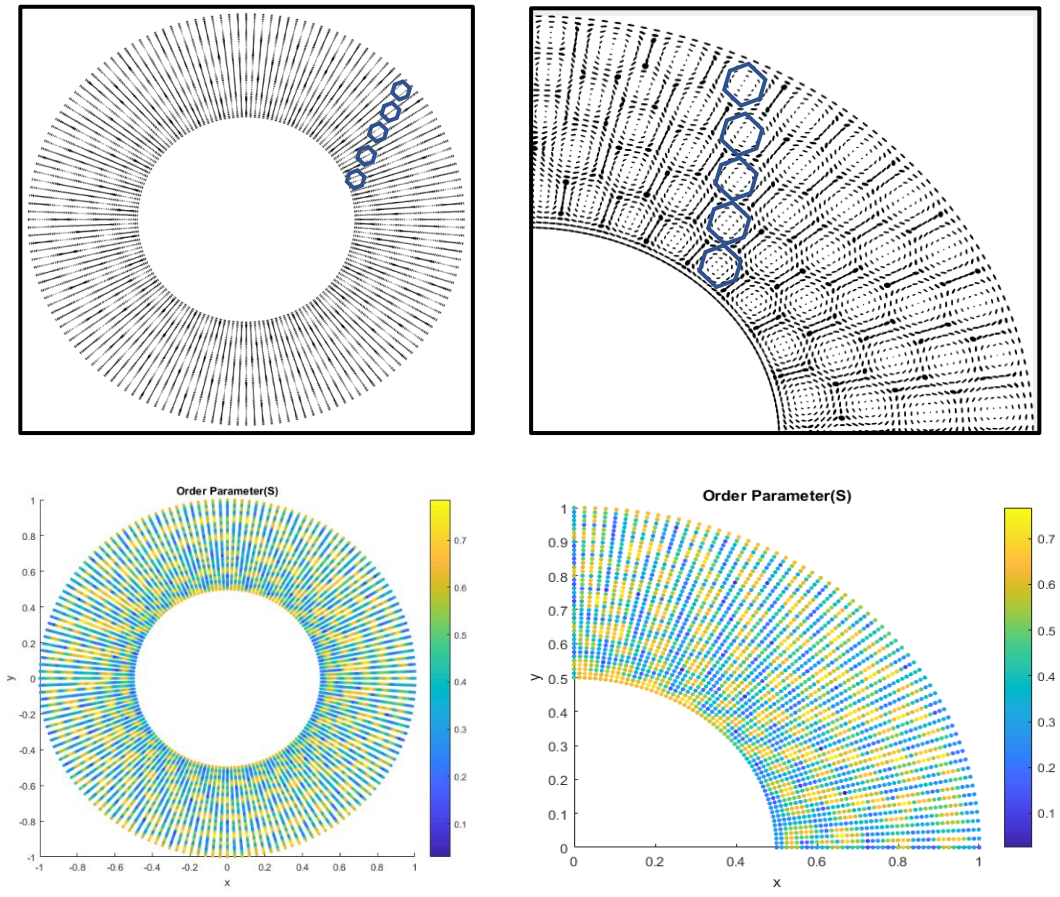

Figure 4-2 Molecular structure, and order parameter, S, between the full domain and a quarter domain

4.2.1.1 Chirality effect:

Chirality influences the structure of molecules. As the structure is fully coupled with the flow, it is expected to have different properties in the flow as chiral strength changes. The chiral strength, θ, varies from 10 to 70. As the tensor-order parameter includes negative eigenvalues, tensor M was used, which is Q+I/3 [24], for the schematic representation of molecules. Since we are simulating a rod-like CLC, triaxial ellipsoids with a major axis equal to the largest eigenvalue of M are used to represent molecule structures. The first and second minor axes correspond to M's second-largest and smallest eigenvalues, respectively, at any point. The aspect ratio of the ellipsoid axes equals the ratio of the eigenvalues of the modified tensor order parameter M.

Figure 4-3 depicts the molecular structure of CLCs between concentric cylinders under different θ at a constant De of 0.001. The results indicate that chiral strength directly influences the helical structure and repetitive structures. At the lowest value of θ (i.e., 10), only one full rotation occurs. The direction of molecules at the boundaries is locked in since the walls are in a fixed boundary condition. Molecules create a helical structure from the inner cylinder to the wall of the outer cylinder perpendicular to the flow direction. As θ increases, the number of full rotations increases proportionally, and complex hexagonal structures appear. As the gap is constant (h), increasing θ means lower cholesteric pith (p). Therefore, the confinement ratio of h/p is higher at higher θ. At a smaller confinement ratio, the cholesteric structure is strongly confined, and the anchoring overcomes the twist pattern. At a higher confinement ratio, where θ is higher, the cholesteric is weakly confined, and the twist pattern is more evident as it is pushed away from the wall into the center, and more repetitive structures were observed.

At θ = 10 (Figure 4-3.a, chiral strength), the chiral term is not high enough to compete with the elasticity terms to build a hexagonal structure. As θ increases to 20 (in Figure 4-3.b), shorter striations in the texture appear as the pitch decreases. As θ further increases to 50 and 70 (as shown in Figures 4-3.c and 4-3.d) chiral interactions increase and cause a more complex structure with a decrease in the helical microstructure size (i.e., smaller pitch).

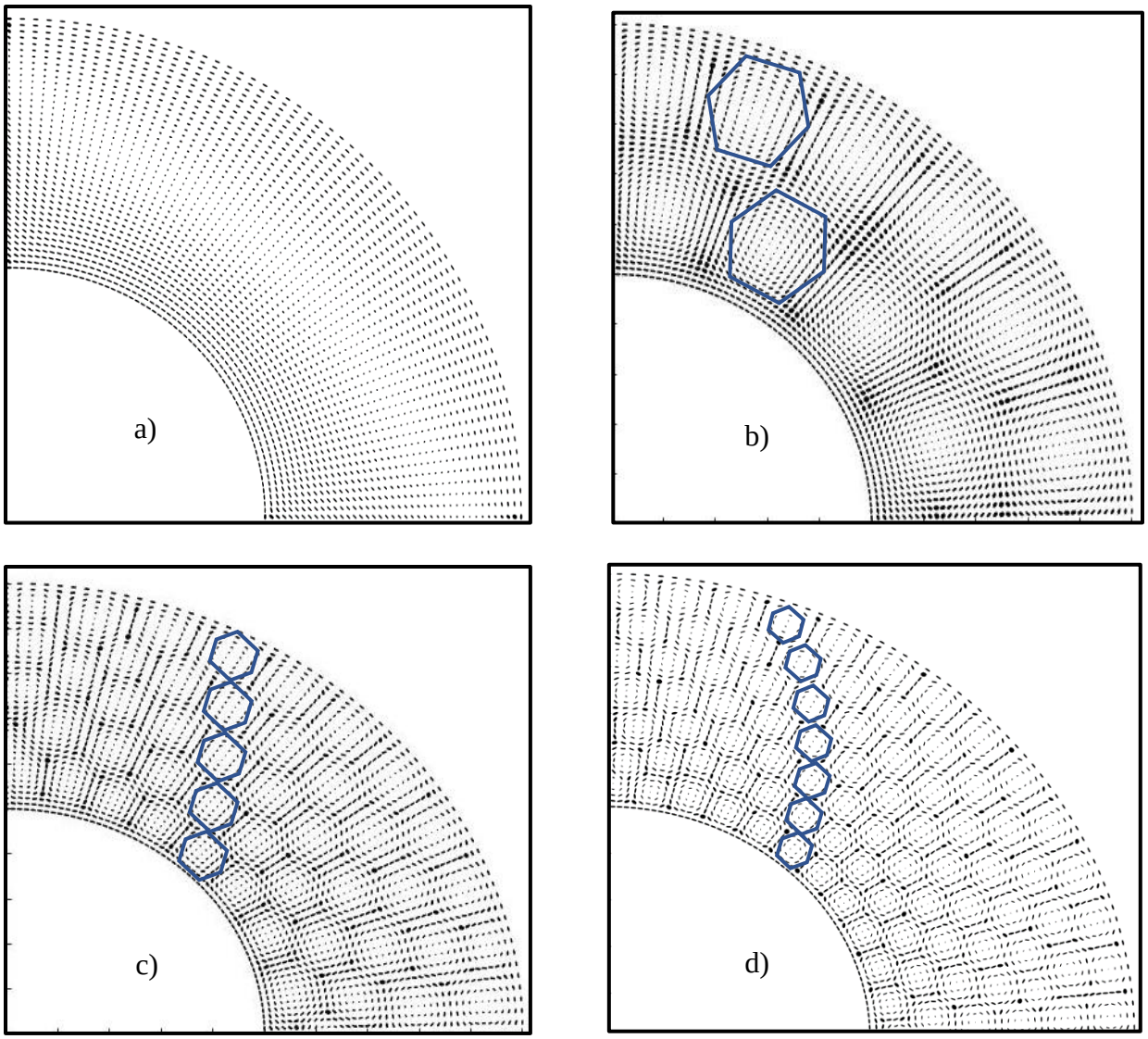

Figure 4-3. Molecular structure of CLCs between concentric cylinders under different θ at a constant De of 0.001; a) θ=10, b) θ=20, c) θ=50, and d) θ=70

To investigate the order of CLCs, contours of the scalar order parameter (S) are presented in Figure 4-4 for all four chiral strengths. A higher degree of orientational order in the domain corresponds to a higher value of S. Scalar order parameter equaling one indicates a fully ordered domain while zero shows absolute randomness or an isotropic state. A lower value of S occurs close to defect points or disclination lines.

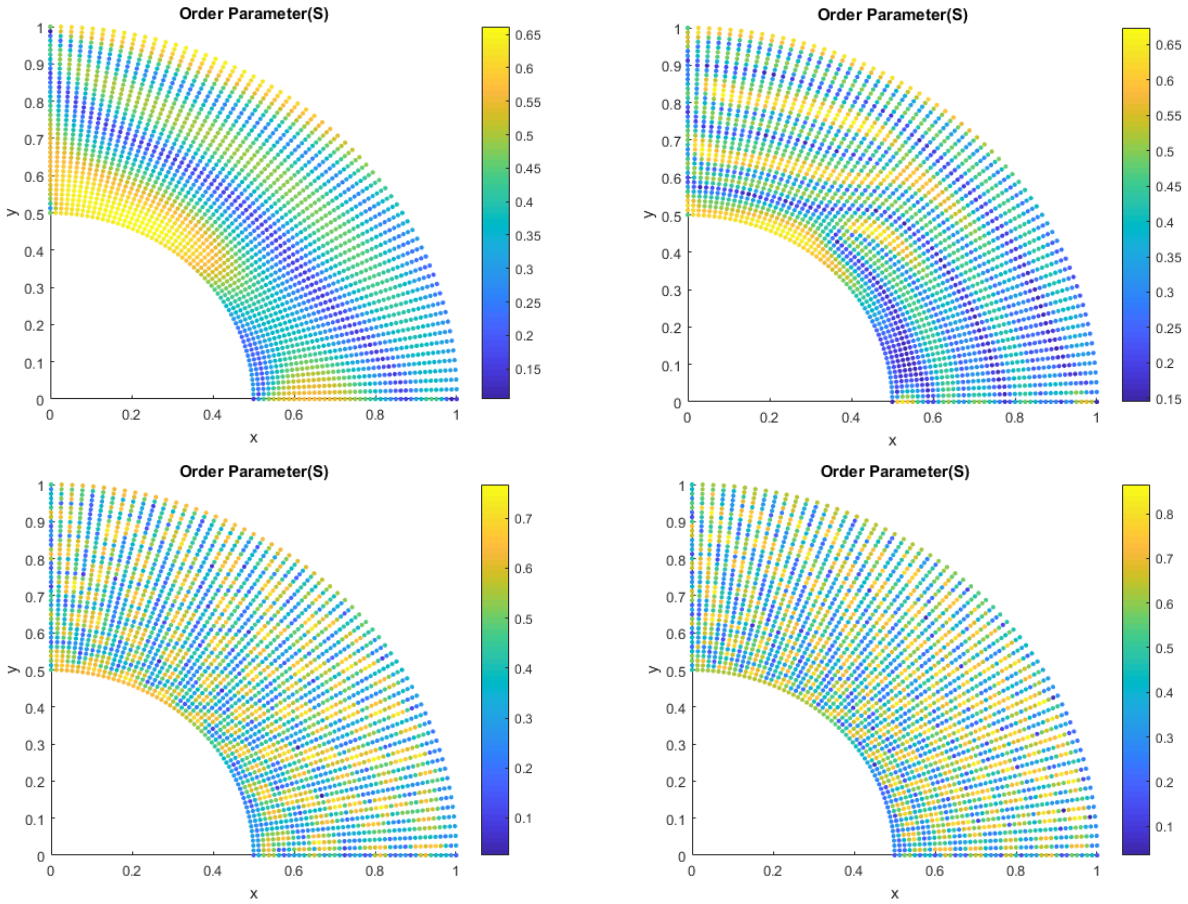

Figure 4-4. Scalar order parameter S for CLCs between concentric cylinders under different θ at a constant De of 0.001; a) θ=10, b) θ=20, c) θ=50, and d) θ=70

At higher θ, the structure becomes more complex, affecting the flow properties. Figure 4-5 compares values for the pressure force per unit length (p_i^*) and friction force per unit length (τ_i^*), on the inner cylinder for θ values from 10 to 70, at a constant De of 0.001. Figure 4-5 indicates a positive correlation between θ and p_i^* and τ_i^* on the inner cylinder. At the lowest θ, p_i^* is around 5, while at a higher chiral strength (θ=70), it significantly increased to 28. A similar pattern can be seen for τ_i^*. Higher θ lowers the pitch and results in higher pressure. τ_i^* increased more than ten times in the range of θ from 10 to 70, due to a higher velocity gradient at higher θ.

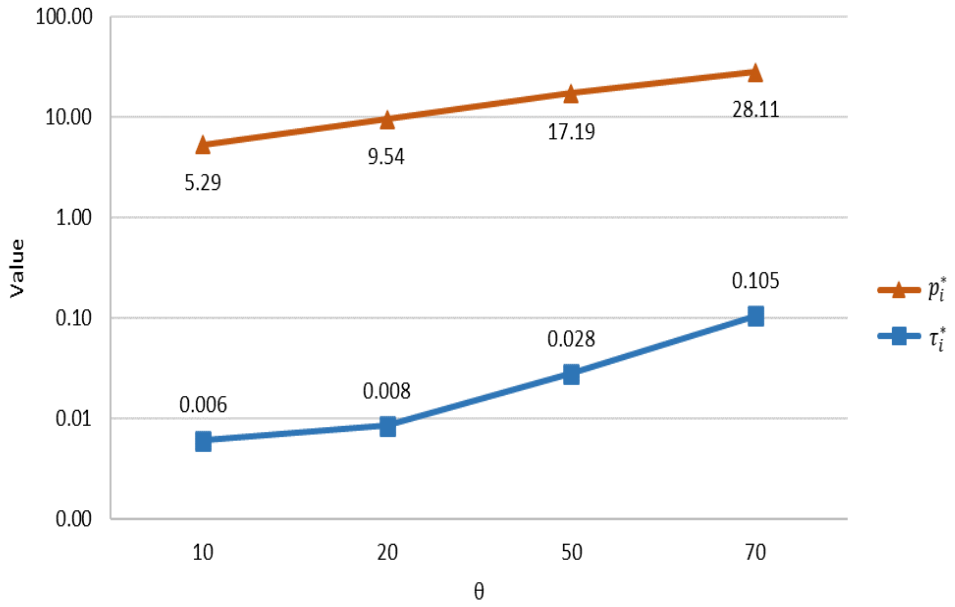

Figure 4-5 p_i^* and τ_i^* on the inner cylinder between concentric cylinders at De= 0.001

4.2.1.2 De effect:

Like the chirality study, the molecular structure under various De numbers from 0.001 to 1 at constant θ=50 were investigated. As R (energy ratio) is constant in this study, changing De corresponds to Er changing. The chiral term is dominant at low Er (i.e., low shear rate) and the twist pattern is evident. In Figure 4-6.a, the five hexagonal structures are seen to exist

between the walls. As De increases from 0.001 to 0.01 (Figure 4-6.b), the structure is still hexagonal and twisted, but the number of hexagonal structures decreases to four.

In comparison, Figure 4-6.c indicates that the competition between chirality and viscous force is more important, with a weak chiral structure. As De reaches one, the chiral structure completely vanishes and the domain becomes almost fully ordered (Figure 4-6.d). This can be seen from the scalar order parameter contours in Figure 4-7. Figures 4-6 and 4-7 indicate that the chiral structure depends on the viscous force.

In Figure 4-7, the scalar order parameters' contours show that low Er (significantly low De) allows the chiral structure to be formed. Nevertheless, as the shear rate increases and Er reaches one, the time-scale characteristic of deformation by the flow becomes comparable to the relaxation time scale of the LCs, and at a high shear rate (i.e., higher viscous forces compared to the chiral strength), the helical structure disappears and converts to a monodomain along the flow direction.

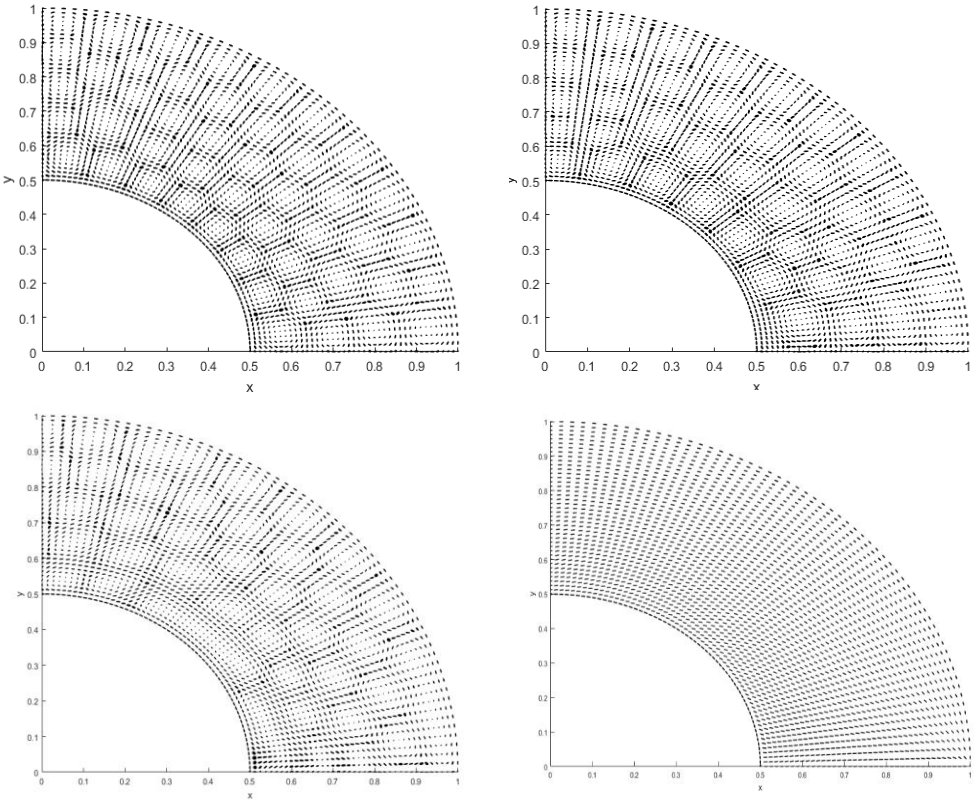
y
x
0 0.1 0.2 0.3 0.4 0.5 0.6 0.7 0.8 0.9 1

Figure 4-6 Molecular structure of CLCs between concentric cylinders at θ=50 at different De numbers; a) De=0.001, b) De=0.01, c) De=0.1, and d) De=1

The effect of higher De numbers on p_i^* and τ_i^* is shown in Figure 4-8. Increasing De numbers (i.e., shear rate) results in increasing τ_i^*. In contrast, p_i^* decreases within the range of De from 0.001 to 0.1 at θ=50, as the number of hexagonal structures decreases, and it then increases for De=1. As shown in Figure 4-6, from De=0.001 to 0.1, hexagonal structures exist and as De increases to 1, the chiral structure is eliminated, which is also seen in other works [85], [145]. The structure becomes close to fully ordered, which leads to an increase in p_i^* and the increase in τ_i^* is due to an increase in the viscous effect (i.e., increases in Er).

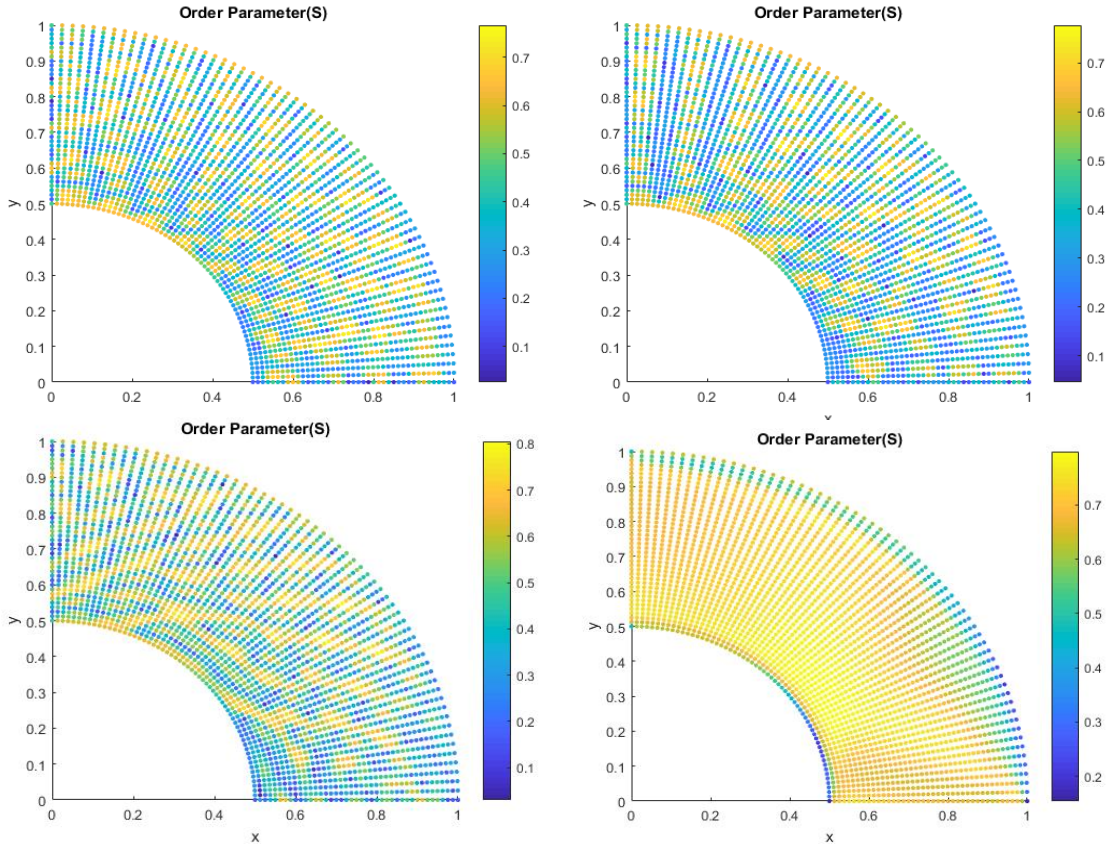

Figure 4-7 Scalar order parameter of CLCs between concentric cylinders at θ=50 and different De numbers; a) De=0.001, b) De=0.01, c) De=0.1, and d) De=1

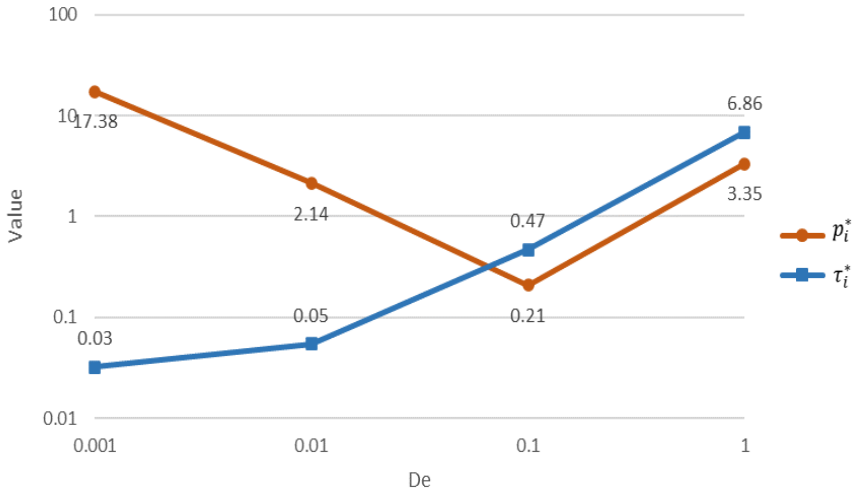

Figure 4-8 p_i^* and τ_i^* on the inner cylinder between concentric cylinders under different De and θ=50

4.2.2 Eccentric Cylinders

In this section, the chiral structures between eccentric cylinders, p_i^* and τ_i^* on the inner cylinder under different flow and geometry conditions were investigated.

4.2.2.1 Chirality Effect

Figure 4-9 shows the chirality effect at constant De=0.001 between eccentric cylinders with an eccentricity of 25%. Chiral strength increases from 20 to 50 at constant De, which increases the chiral term, and consequently, the number of hexagonal structures (i.e., decreases

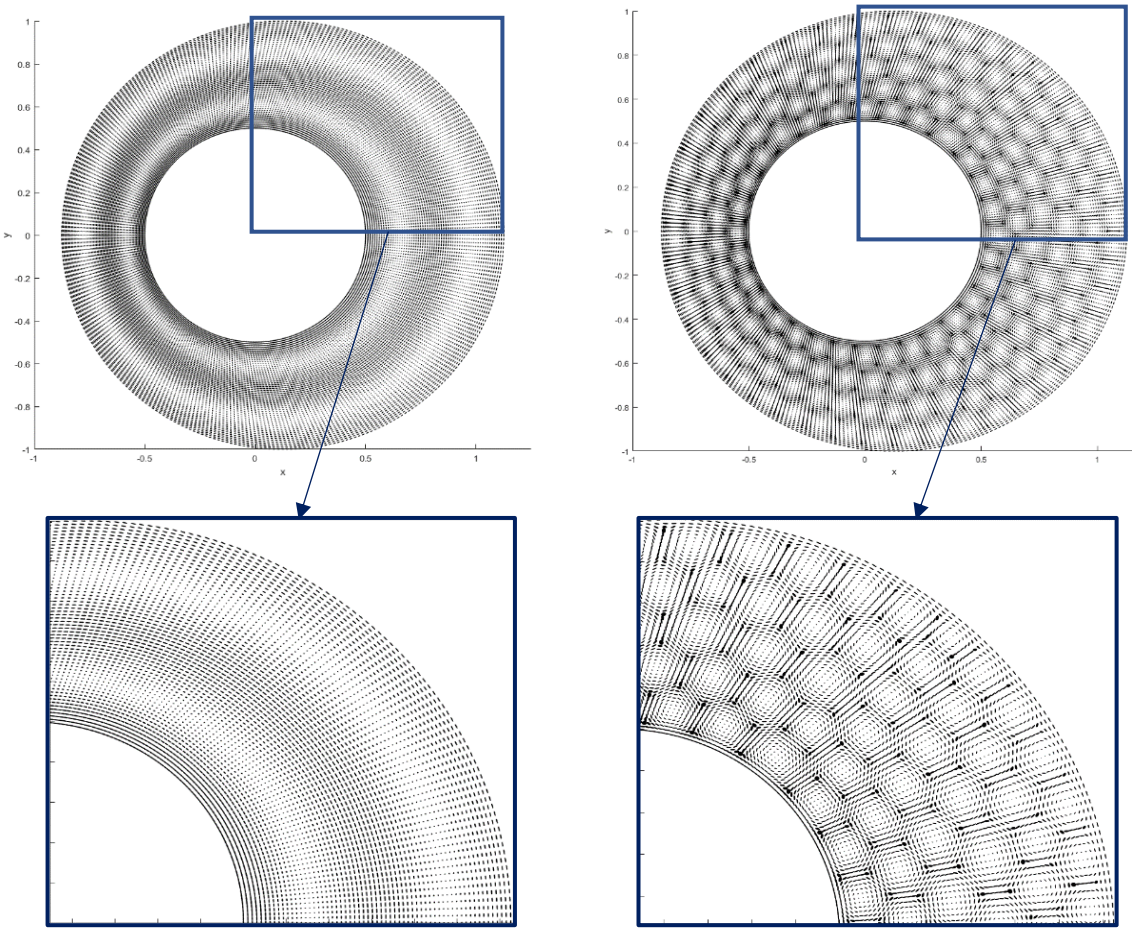

the pitch). As discussed before, the number of rotations results from a competition between the chiral term and the elasticity.

Figure 4-9 Molecular structure of CLCs between eccentric cylinders with eccentricity of 25% under different θ and De=0.001; a) θ=20, b) θ=50, c) magnified (a), and d) magnified (b)

At a higher chirality, the twist pattern is more evident as the chiral structure competes with elasticity and makes more twisted patterns in the confined domain. For the eccentric case, at θ=50, the hexagonal structure is dominant, while at θ=20, the twisted pattern of CLC is observed.

The scalar order parameter contours for the chiral strength of 20 and 50 at constant De=0.001 are shown in Figure 4-10, which clearly shows a higher order with a higher twist and a more structured pattern at higher θ.

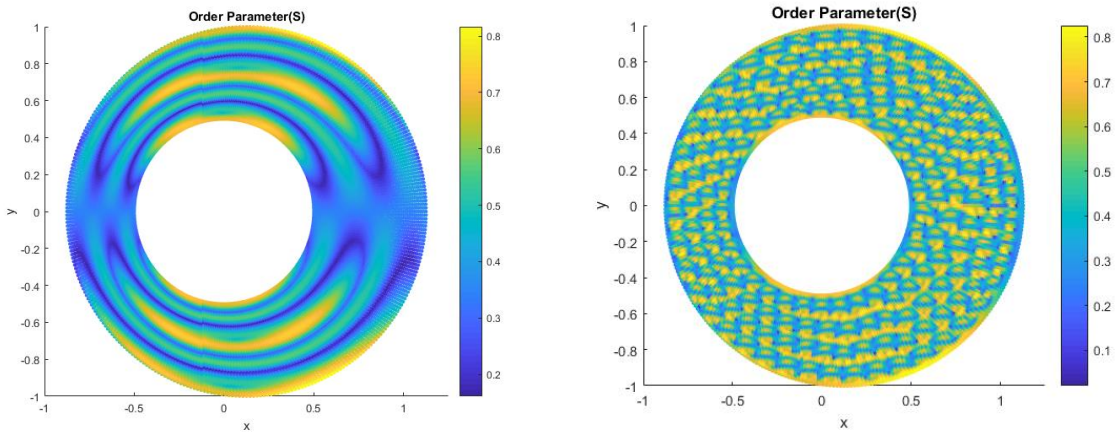

Figure 4-10 Scalar order parameter of CLCs between eccentric cylinders with eccentricity of 25% under different θ and De=0.001; a) θ=20 and b) θ=50

4.2.2.2 De Effect

Increasing the De number at a constant θ between eccentric cylinders affects the chiral structure. Figure 4-11 illustrates that at higher De (i.e., higher shear rate), the chiral structure is diminished. Although the hexagonal structure is evident at De=0.001 and θ=50, at De=1, no chiral structure is evident, and the molecules are ordered. This can be seen in the scalar order

parameter contours (Figure 4-12), where no chiral structure is seen, and a considerable part of the domain has a value close to one (i.e., fully ordered). Depending on the chiral strength, the value of De that diminishes the chiral structure can differ.

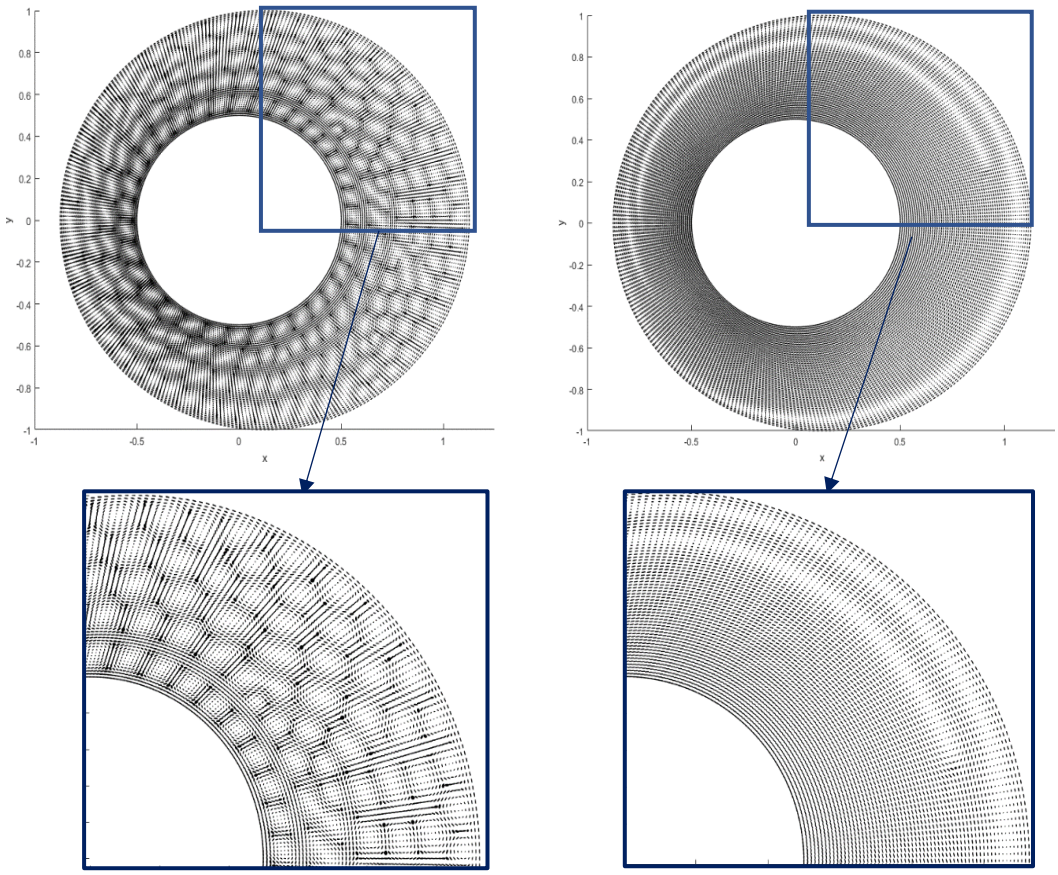

Figure 4-11. Molecular structure of CLCs between eccentric cylinders with eccentricity of 25% under different De and θ=50; a) De=0.001, b) De=1, c) magnified (a), and d) magnified (b)

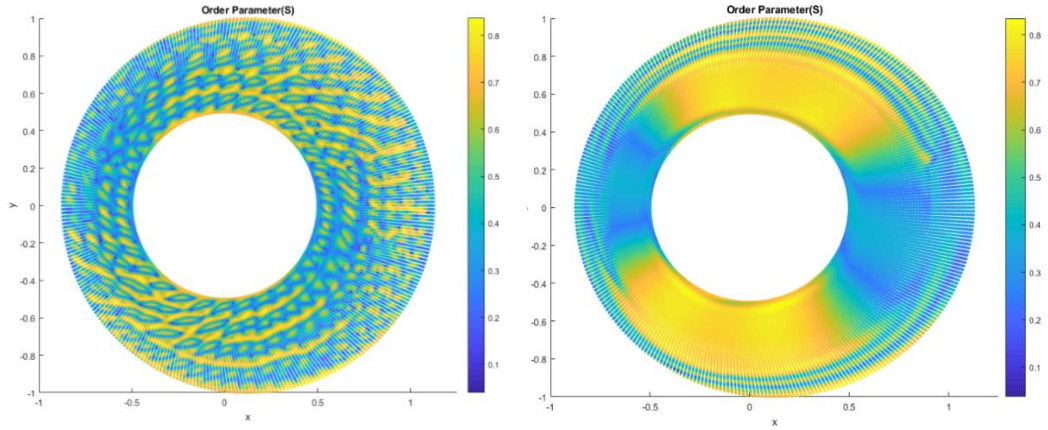

Figure 4-12. Scalar order parameter of CLCs between eccentric cylinders with eccentricity of 25% under different De numbers and θ=50; a) De=0.001 and b) De=1

4.2.2.3 Eccentricity Ratio

In this section, the structure of CLCs under eccentricity ratios of 0% (concentric), 25%, and 70% at constant De=0.1 and chiral strength of 50 was considered (Figure 4-13). The eccentricity of zero was discussed in the concentric section, where five hexagonal structures existed in the domain. It was found that at a chiral strength of 50 and De = 0.1, increasing eccentricity results in a higher number of hexagonal structures in the wider domain. Nevertheless, in the narrower domain, the structure is completely different. For an eccentricity of 70%, no hexagonal pattern is seen in the narrower domain due to the small gap, compared to the molecules' pitch, which prevents the molecules from forming a hexagonal pattern; a similar pattern was observed in [84]. Nevertheless, at lower eccentricities (0% and 25%), hexagonal patterns occur in the narrower domain. Figures 4-13 and 4-14 indicate that increasing the eccentricity causes a loss in the uniformity of microstructures due to confinement in the geometry, which decreases the rotational freedom.

The effect of eccentricity on p_i^* and τ_i^* is shown in Figure 4-15. As can be seen, the eccentricity effect on p_i^* on the inner cylinder is significant. Moreover, τ_i^* is positively correlated with eccentricity, and we see a higher τ_i^* as the eccentricity increases, though it is

less significant than p_i^*. This can be explained by the increasing number of hexagonal structures in the wider part of higher eccentricity, which results in higher p_i^*, as discussed earlier. On the other hand, we know that in all of the fluids, a higher eccentricity leads to a higher p_i^*. Therefore, the combination of these two factors leads to a more noticeable change in p_i^*.

As discussed earlier, LCs form ordered layers close to the solid surfaces, improving the tribological properties. In this chapter, the molecular structure of CLCs under different flow and geometry conditions was investigated. CLC molecules were found to have a preferred direction in the vicinity of solid surfaces for all cases. Theoretically, this formation, tangential to the solid surfaces, decreases the wear rate of the rubbing surfaces, and consequently, it lowers the coefficient of friction, making CLCs a good candidate for use as lubricants.

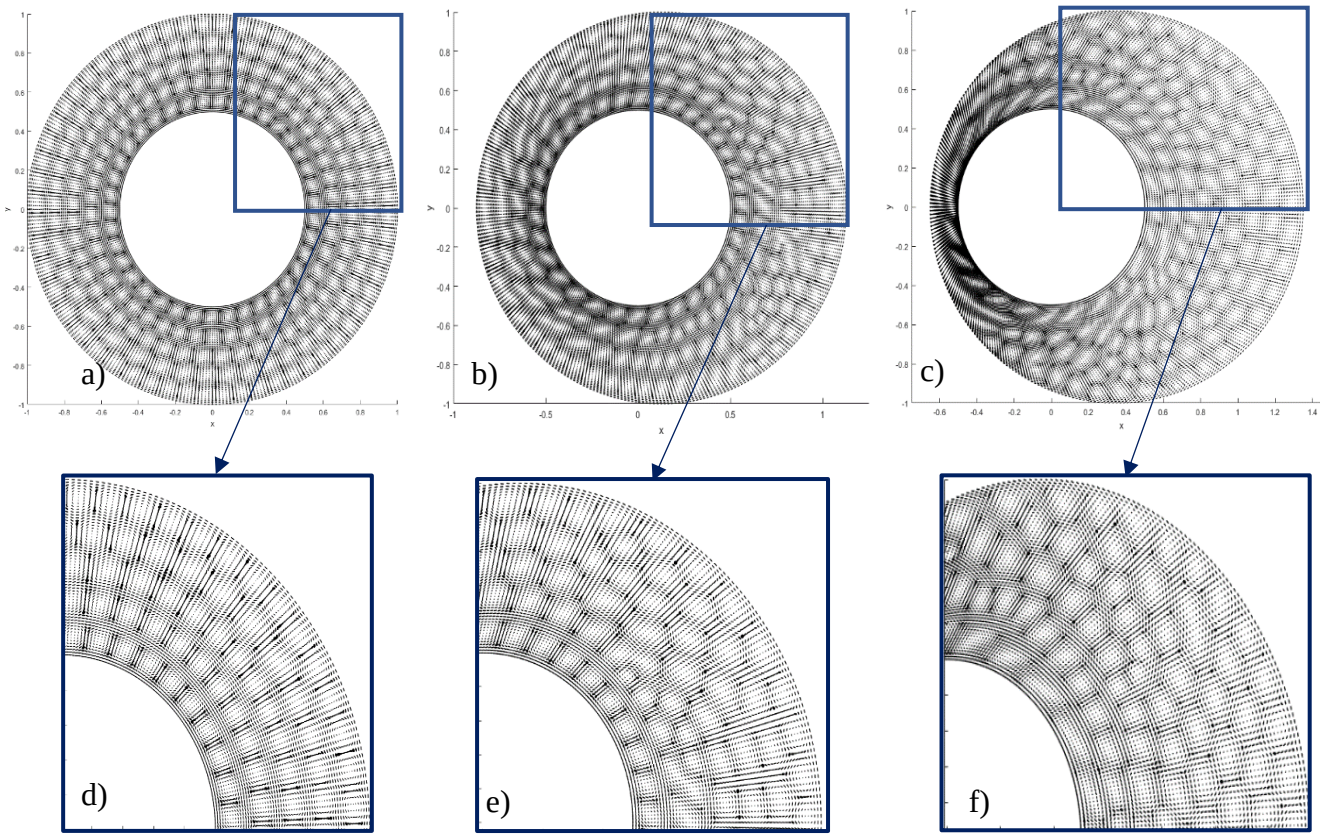

Figure 4-13. Molecular structure of CLCs under different eccentricity ratios and De=0.1 and θ=50; a) ε=0%, b) ε=25%, c) ε=70% d) magnified (a), e) magnified (b), and f) magnified (c)

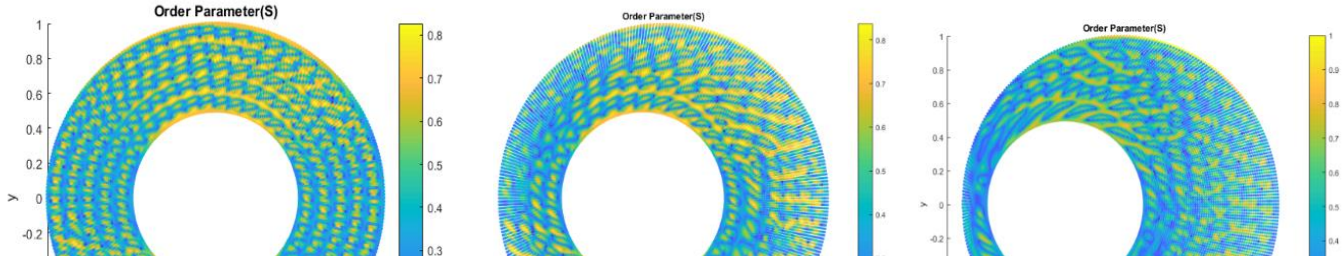

Figure 4-14. Scalar order parameter of CLCs under different eccentricity ratios and De= 0.1 and θ=50; a) ε=0%, b) ε=25%, and c) ε=70%

In this chapter, p_i^* and τ_i^* on the inner cylinder under different conditions were also studied. With regards to the lubrication problem in journal bearings, higher p_i^* can be translated to a higher load-carrying capacity, while a higher magnitude of τ_i^* is a sign of higher coefficient of friction. Higher chirality strength (θ) was found to consistently increase p_i^*, while keeping τ_i^* at the same level. Therefore, a higher θ could improve the lubrication performance. On the other hand, lower De can also improve the performance as it possesses the combination of high p_i^* and low τ_i^*. In terms of the eccentricity ratio, though p_i^* was significantly correlated with the eccentricity ratio, the τ_i^* changed gradually, which means that we would expect a better performance when CLCs are used as lubricants at higher eccentricity.

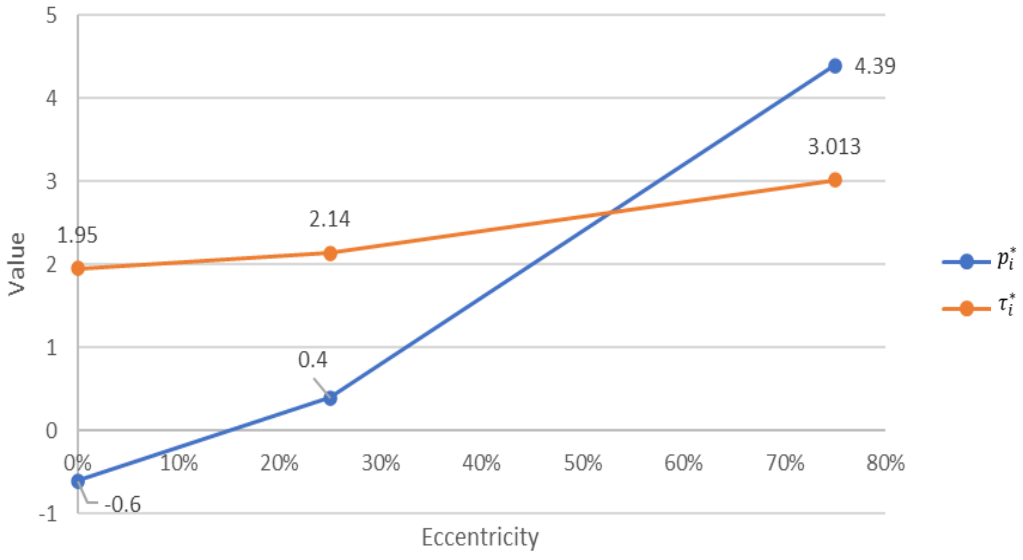

Figure 4-15 p_i^* and τ_i^* on the inner cylinder between eccentric cylinders under different eccentricities at De=0.1 and θ=50

4.3 Conclusion

In this chapter, the behaviour of CLCs between concentric and eccentric cylinders was investigated and compared the molecules' structures and responses to the flow properties under different conditions. LdG theory, which is powerful in capturing the details of the structure, was employed to capture the evolution of microstructure for chiral materials and it was coupled with linear momentum balance equation (modified Navier-Stokes equation). The effect of the De number, θ (or chiral strength), and eccentricity ratios were investigated. It was found that depending on the chiral strength and De number, the microstructure differs as the chiral term competes with the elasticity and viscous terms. For both concentric and eccentric cylinders, the molecules were found to create a helical structure from the inner cylinder to the wall of the outer cylinder perpendicular to the flow direction when the chiral term is dominant. The number of full rotations increased as the chiral strength increased, and complex hexagonal structures appeared. The chirality study showed a positive correlation between θ and p_i^*, τ_i^* and τ_i^* on the inner cylinder. The molecular structures under De numbers from 0.001 to 1 at constant θ=50 were investigated, and the chiral term was found to be dominant at low De (i.e., low shear rate) and the twist pattern was evident. At higher De, the chiral structure completely vanishes. In the eccentric cylinders study, similar to the concentric cylinders, the twist pattern is more pronounced at higher chirality, and at higher De (or higher shear rate), the flow diminishes the chiral structure. No chiral structure was found at De=1, θ=50, and an eccentricity of 25%, where the molecules were fully ordered. The structure of CLCs under eccentricity ratios of 25% and 70% at constant De and chiral strength was also investigated, and it was found that at an eccentricity of 70%, a similar but less uniform structure is seen in the wider domain, and no hexagonal pattern is seen in the narrower domain. This difference in the structure resulted in a jump in p_i^* on the inner cylinder at an eccentricity of 70%, compared to other eccentricities. With respect to the lubrication problem, an ordered formation of CLCs in the vicinity of solid surfaces was observed, which theoretically could improve the

tribological properties. Moreover, at higher chirality strengths and eccentricity ratios, and lower De, CLCs perform better as potential lubricants.

5) Chapter 5: Conclusion, Contribution, and Future Research Directions

This chapter presents a summary of the main findings and the steps taken toward studying LCs, followed by a list of contributions to the field of LCs and future work.

5.1 Summary and Conclusion

The numerical study of LCs was the focus of this thesis. The analytical method to calculate the viscosity coefficients and rheological properties of DNLCs was initially proposed. The method was applied to nematic GO dispersions as an example of DNLCs and the results were compared with the experimental results to verify the proposed method. GO dispersions have attracted enormous attention due to their unique LC and rheological properties. The results showed that the alignment viscosities from the analytical method were in excellent agreement with the experimental ones.

The alignment viscosities for concentrations from 15 to 30 mg/ml calculated by the analytical method were in agreement with the experimental results.

Although this study was focused on GO dispersion as an example of DNLC, the method can be applied to other nematic GO suspensions (e.g., different sizes of the particles) or any DNLC to find Leslie's viscosities and/or rheological properties. This theory can be applied to any DNLC with inputs from the experimental study: the size distribution of the particles, their average thickness, and the average viscosity from (at least five) different samples. The only limitation of this theory is the disc's thickness, as it should be thin ($p \ll 1$).

Moreover, the Leslie and the Landau viscosities coefficients, the alignment viscosity, the rotational diffusivity, and other rheological properties were calculated as a function of concentration. The Landau and Leslie viscosity coefficients calculated using the proposed

analytical method can be used to calculate the viscous stress tensors in the EL and the LdG theories when modelling DNLC in different applications.

In chapter three, the calculated coefficients in chapter two were used to calculate the viscous stress tensor in the EL theory and to simulate the flow of GO dispersions between concentric cylinders. The viscosities of GO dispersions were also compared with the experimental values, and it was observed that they were in good agreement. Calculating the coefficients from the proposed model and applying it to the EL theory resulted in understanding the behaviour of GO dispersions in the concentration range 15 mg/ml to 30 mg/ml and obtaining the orientation and the viscosity profile for dimensionless shear rates from 10^{-3} to 10^{4}. It was found that at lower shear rates, the elastic forces dominate the orientation profile of the director. As the shear rate increases, the viscous forces become predominant, and the orientation in the bulk of the domain reaches the alignment angle. Besides, it was shown that the solution's stability depended on the initial guess, and the alignment angle was not dependent on Frank's elastic constant in the considered range.

In the last chapter, the behaviour of CLCs between concentric and eccentric cylinders has been investigated. The numerical simulations were performed in COMSOL Multiphysics, and the LdG theory was applied using the PDE module. This theory was implemented in dynamic finite element simulations to solve the evolution of the microstructure of CLCs coupled with a linear momentum balance equation (modified 2D Navier-Stokes equation). The microstructure formation of CLCs for parameters such as chirality strength, Deborah number (De), and eccentricity of eccentric cylinders have been obtained. It was shown that for both concentric and eccentric cylinders, the molecules created a helical structure from the inner cylinder to the wall of the outer cylinder perpendicular to the flow direction when the chiral term was dominant. The number of full rotations increased as the chiral strength increased, and hexagonal structures appeared.

Moreover, it was shown that at low De, i.e., low shear rate, the chiral term is dominant, and the twist pattern is evident, and at higher De, the chiral structure completely vanished. The effect of eccentricity on the structure of CLCs at constant De and chiral strength was also investigated, and it was found that the twist pattern is more pronounced at higher chirality, and at higher De, the flow diminishes the chiral structure. It was also shown that at the eccentricity of 70%, no hexagonal pattern occurs in the narrower domain, and the difference in the structure

results in higher pressure on the inner cylinder compared to other eccentricities. In order to optimize the performance of CLCs as lubricants between cylinders, we recommend applying them at higher chirality strengths and eccentricity ratios while keeping De as low as possible.

5.2 Limitations

The limitations of this study are reported in three different sections corresponding to three different chapters as below:

- The methodology in chapter two needs inputs from the experimental studies on DNLCs, which are the distribution of the size of the GO dispersion, their average thickness, and the average viscosity from (at least five) different measurements. This method is also limited to the thin disc, where the ratio of thickness to the average diameter of the DNLC is extremely low ($p \ll 1$).
- The methodology in chapter three involves an initial guess to be provided to simulate the flow of DNLCs. As mentioned in chapter two, finding a reasonable initial guess for the orientation angle is challenging as it can result in divergence in the solution. Moreover, Frank's elasticity coefficients of GO were unavailable, and common values for the coefficients were used.
- The simulation of CLCs in chapter four was considerably computationally expensive as full Navier-Stokes equations were coupled with LdG equations in COMSOL Multiphysics to simulate the flows. The full Navier-Stokes equations were needed to converge the solution. However, the solution was not converged for the geometry of eccentric cylinders at extremely high eccentricity ratio (>80%) or high Re number ($>10^2$). Moreover, the ratio of chirality strength to the (narrowest) gap between the cylinders played a vital role in the convergence of the solution. As the chirality strength increases, the convergence of the solution in a higher eccentricity ratio becomes more difficult.

5.3 Contribution

The contributions of this study, as already published or submitted to several journals and conferences, are:

- Proposing a method to calculate the required rheological coefficients of DNLCs to apply the EL or LdG theory to complex flows of DNLCs. To the author's knowledge, this study is the first to propose an analytical method to calculate the Leslie and Landau viscosity coefficients of DNLCs.
- Understanding the behaviour of GO aqueous suspensions under flow between eccentric cylinders, which is a DNLC in a specific range of concentrations, using our proposed method.
- Understanding the complex flow of CLCs between two concentric and eccentric cylinders using the LdG nematodynamic equation coupled with the Navier-Stokes equation. To the author's knowledge, this study is the first to capture the structure of CLCs in the complex geometry of concentric and eccentric cylinders.

5.4 Future Research Directions

Considering the current accomplishments and experiences in the simulation of complex flows and understanding the computational costs associated with numerical simulations of LCs, the following research directions can be proposed:

- To investigate the flow of DNLCs in a complex flow using LdG to capture the structure of DNLCs.
- To compare the efficiency of DNLCs, rod-like NLCs, and CLCs as lubricants and using a journal-bearing geometry.
- To perform the simulation of CLCs in 3D to reveal more details in the microstructure of CLCs and defect nucleation.
- To extend the study of CLCs with more realistic parameters, closer to the actual journal-bearing problem, and investigate the rheological and tribological characteristics of CLCs
- To investigate the effect of electric or magnetic field on the formation of structure and defects nucleation of both DNLCs and CLCs to design smart bio-lubricants

- To investigate the coefficient of friction under the same conditions and optimize it based on different flow and geometry parameters for applying CLCs as lubricants in journal bearings.

References

[1] Z. Xu and C. Gao, “Aqueous liquid crystals of graphene oxide,” *ACS Nano*, vol. 5, no. 4, pp. 2908–2915, Apr. 2011.

[2] F. Lin, G. Yang, C. Niu, Y. Wang, Z. Zhu, and H. Luo, “Planar Alignment of Graphene Sheets by a Rotating Magnetic Field for Full Exploitation of Graphene as a 2D Material,” *Adv. Funct. Mater.*, p. 1805255, Sep. 2018.

[3] C. M. Care and D. J. Cleaver, “Computer simulation of liquid crystals,” *Reports Prog. Phys.*, vol. 68, no. 11, pp. 2665–2700, Sep. 2005.

[4] R. G. Larson, *The structure and rheology of complex fluids*. Oxford University Press, 1999.

[5] P. De Gennes and Prost, *The Physics of Liquid Crystals*, vol. 3rd. Oxford university press, 1996.

[6] S. (Sivaramakrishna) Chandrasekhar, *Liquid crystals*. Cambridge University Press, 1992.

[7] H. K. Bisoyi and S. Kumar, “Discotic nematic liquid crystals: Science and technology,” *Chemical Society Reviews*, vol. 39, no. 1. pp. 264–285, Jan-2010.

[8] S. Kumar, “Investigations on discotic liquid crystals,” vol. 47, no. 8, pp. 1195–1203, Jun. 2020.

[9] N. V. Usol’tseva and A. I. Smirnova, “Liquid crystals as lubricants,” *Lubricants*, vol. 7, no. 12. MDPI AG, p. 111, 01-Dec-2019.

[10] A. M. Dimiev and S. Eigler, *Graphene oxide : fundamentals and applications*. .

[11] X. Lin, D. Schmelter, S. Imanian, and H. Hintze-Bruening, “Hierarchically Ordered α-Zirconium Phosphate Platelets in Aqueous Phase with Empty Liquid,” *Sci. Rep.*, vol. 9, no. 1, pp. 1–15, Dec. 2019.

[12] L. J. Michot *et al.*, “Liquid-crystalline aqueous clay suspension,” *Proc. Natl. Acad. Sci. U. S. A.*, vol. 103, no. 44, pp. 16101–16104, Oct. 2006.

[13] Aurélie Jullien, Adriana Scarangella, Umberto Bortolozzo, Stefania Residori, and Michel Mitov, “Nanoscale hyperspectral imaging of tilted cholesteric liquid crystal structures,” *Soft Matter*, vol. 15, no. 15, pp. 3256–3263, Apr. 2019.

[14] N. Noroozi, “Numerical simulations of flow and microstructure in nematic liquid crystalline materials,” University of British Columbia, 2013.

[15] F. Livolant and A. Leforestier, “Condensed phases of DNA: Structures and phase transitions,” *Prog. Polym. Sci.*, vol. 21, no. 6, pp. 1115–1164, Jan. 1996.

[16] L. Barberi, F. Livolant, A. Leforestier, and M. Lenz, “Local structure of DNA toroids reveals curvature-dependent intermolecular forces,” *bioRxiv*, 2020.

[17] M. Eltsov, D. Grewe, N. Lemercier, A. Frangakis, F. Livolant, and A. Leforestier, “Nucleosome conformational variability in solution and in interphase nuclei evidenced by cryo-electron microscopy of vitreous sections,” *Nucleic Acids Res.*, vol. 46, no. 17, pp. 9189–9200, Sep. 2018.

[18] H. C. BERG and R. A. ANDERSON, “Bacteria Swim by Rotating their Flagellar Filaments,” *Nat. 1973 2455425*, vol. 245, no. 5425, pp. 380–382, 1973.

[19] S. F. Ermakov, N. K. Myshkin, V. I. Kolesnikov, and A. P. Sychev, “On the mechanism of cholesteric liquid crystal lubricity in metal joint friction,” *J. Frict. Wear 2015 366*, vol. 36, no. 6, pp. 496–501, Dec. 2015.

[20] S. F. Ermakov, V. I. Kolesnikov, and A. P. Sychev, “Lubricity of cholesteric liquid-crystal nanomaterials in friction of solids,” *J. Frict. Wear 2016 372*, vol. 37, no. 2, pp. 136–140, May 2016.

[21] N. V. Usol’tseva *et al.*, “Rheological characteristics of different carbon nanoparticles in cholesteric mesogen dispersions as lubricant coolant additives,” *J. Frict. Wear 2015 365*, vol. 36, no. 5, pp. 380–385, Oct. 2015.

[22] Y. Gao, Y. Jiang, W. Hu, H. Jiang, and J. Li, “Cholesteryl Liquid Crystals as Oil-Based Lubricant Additives: Effect of Mesogenic Phases and Structures on Tribological Characteristics,” 2019.

[23] D. Grecov and A. D. Rey, “Theoretical and Computational Rheology for Discotic Nematic Liquid Crystals,” *Mol. Cryst. Liq. Cryst.*, vol. 391, no. 1, pp. 57–94, Jan. 2003.

[24] N. Noroozi and D. Grecov, “Flow modelling and rheological characterization of nematic liquid crystals between concentric cylinders,” *Liq. Cryst.*, vol. 40, no. 7, pp. 871–883, Jul. 2013.

[25] N. Noroozi, D. Grecov, and S. Shafiei-Sabet, “Estimation of viscosity coefficients and rheological functions of nanocrystalline cellulose aqueous suspensions,” *Liq. Cryst.*, vol. 41, no. 1, pp. 56–66, 2014.

[26] K. H. Nam *et al.*, “Green, fast, and scalable production of reduced graphene oxide via

Taylor vortex flow," *Chem. Eng. J.*, vol. 391, Jul. 2020.

[27] M. Alamer, A. R. Lim, and Y. L. Joo, "Continuous Synthesis of Structurally Uniform Graphene Oxide Materials in a Model Taylor–Couette Flow Reactor," *Ind. Eng. Chem. Res.*, vol. 58, no. 3, pp. 1167–1176, Jan. 2018.

[28] G. Biresaw, *Tribology and the liquid-crystalline state*, vol. 441. Washington, DC: American Chemical Society, 1990.

[29] G. H. Brown and J. J. (Jerome J. Wolken, *Liquid crystals and biological structures*. Academic Press, 1979.

[30] D. R. Dreyer, S. Park, C. W. Bielawski, and R. S. Ruoff, "The chemistry of graphene oxide.," *Chem. Soc. Rev.*, vol. 39, no. 1, pp. 228–40, Jan. 2010.

[31] A. Akbari *et al.*, "Large-area graphene-based nanofiltration membranes by shear alignment of discotic nematic liquid crystals of graphene oxide," *Nat. Commun.*, vol. 7, p. 10891, Mar. 2016.

[32] C. N. R. Rao, A. K. Sood, K. S. Subrahmanyam, and A. Govindaraj, "Graphene: The new two-dimensional nanomaterial," *Angew. Chemie - Int. Ed.*, vol. 48, no. 42, pp. 7752–7777, Oct. 2009.

[33] M. Allen, V. Tung, R. K.-C. reviews, and undefined 2010, "Honeycomb carbon: a review of graphene," *ACS Publ.*, vol. 110, no. 1, pp. 132–145, Jan. 2006.

[34] M. P.-C. S. Reviews and undefined 2010, "Graphene-based nanomaterials and their electrochemistry," *pubs.rsc.org*.

[35] F. Kim, J. Luo, R. Cruz-Silva, L. J. Cote, K. Sohn, and J. Huang, "Self-propagating domino-like reactions in oxidized graphite," *Wiley Online Libr.*, vol. 20, no. 17, pp. 2867–2873, Sep. 2010.

[36] J. Wassei, R. K.-M. today, and undefined 2010, "Graphene, a promising transparent conductor," *Elsevier*.

[37] N. I. Kovtyukhova, P. J. Ollivier, B. R. Martin, T. E. Mallouk, S. A. Chizhik, and E. V. Buzaneva, "Layer-by-layer assembly of ultrathin composite films from micron-sized graphite oxide sheets and polycations," *Chem. Mater.*, vol. 11, no. 3, pp. 771–778, 1999.

[38] D. Li, M. B. Müller, S. Gilje, R. B. Kaner, and G. G. Wallace, "Processable aqueous dispersions of graphene nanosheets," *Nat. Nanotechnol.*, vol. 3, no. 2, pp. 101–105, Feb. 2008.

[39] M. M. Gudarzi, “Colloidal Stability of Graphene Oxide: Aggregation in Two Dimensions,” *Langmuir*, vol. 32, no. 20, pp. 5058–5068, May 2016.

[40] S. H. Aboutalebi, M. M. Gudarzi, Q. Bin Zheng, and J.-K. Kim, “Spontaneous Formation of Liquid Crystals in Ultralarge Graphene Oxide Dispersions,” *Adv. Funct. Mater.*, vol. 21, no. 15, pp. 2978–2988, Aug. 2011.

[41] R. H. Hurt and Z. Chen, “Liquid Crystals and Carbon Materials,” *Phys. Today*, vol. 53, no. 3, pp. 39–44, 2000.

[42] H. K. Bisoyi and S. Kumar, “Liquid-crystal nanoscience: an emerging avenue of soft self-assembly,” *Chem. Soc. Rev.*, vol. 40, no. 1, pp. 306–319, Dec. 2011.

[43] M. B. Coskun, A. Akbari, D. T. H. Lai, A. Neild, M. Majumder, and T. Alan, “Ultrasensitive Strain Sensor Produced by Direct Patterning of Liquid Crystals of Graphene Oxide on a Flexible Substrate,” *ACS Appl. Mater. Interfaces*, vol. 8, no. 34, pp. 22501–22505, Aug. 2016.

[44] R. Jalili *et al.*, “Scalable One-Step Wet-Spinning of Graphene Fibers and Yarns from Liquid Crystalline Dispersions of Graphene Oxide: Towards Multifunctional Textiles,” *Adv. Funct. Mater.*, vol. 23, no. 43, pp. 5345–5354, Nov. 2013.

[45] D. Berman, A. Erdemir, and A. V. Sumant, “Reduced wear and friction enabled by graphene layers on sliding steel surfaces in dry nitrogen,” *Carbon N. Y.*, vol. 59, pp. 167–175, Aug. 2013.

[46] P. F. Li, H. Zhou, and X. Cheng, “Investigation of a hydrothermal reduced graphene oxide nano coating on Ti substrate and its nano-tribological behavior,” *Surf. Coatings Technol.*, vol. 254, pp. 298–304, Sep. 2014.

[47] M. Sarno, A. Senatore, C. Cirillo, V. Petrone, and P. Ciambelli, “Oil lubricant tribological behaviour improvement through dispersion of few layer graphene oxide,” *J. Nanosci. Nanotechnol.*, vol. 14, no. 7, pp. 4960–4968, 2014.

[48] Y. Liu, X. Wang, G. Pan, and J. Luo, “A comparative study between graphene oxide and diamond nanoparticles as water-based lubricating additives,” *Sci. China Technol. Sci.*, vol. 56, no. 1, pp. 152–157, Jan. 2013.

[49] F. Su, G. Chen, P. H.- Friction, undefined 2020, and P. Huang, “Lubricating performances of graphene oxide and onion-like carbon as water-based lubricant additives for smooth and sand-blasted steel discs,” vol. 8, no. 1, pp. 47–57.

[50] H. Kinoshita, Y. Nishina, A. A. Alias, and M. Fujii, “Tribological properties of monolayer graphene oxide sheets as water-based lubricant additives,” *Carbon N. Y.*, vol. 66, pp. 720–723, Jan. 2014.

[51] O. Elomaa, V. K. Singh, A. Iyer, T. J. Hakala, and J. Koskinen, “Graphene oxide in water lubrication on diamond-like carbon vs. stainless steel high-load contacts,” *Diam. Relat. Mater.*, vol. 52, pp. 43–48, Feb. 2015.

[52] F. M. Leslie, “Theory of flow phenomena in nematic liquid crystals,” Springer, New York, NY, 1987, pp. 235–254.

[53] P. G. De Gennes, “Short Range Order Effects in the Isotropic Phase of Nematics and Cholesterics,” *Mol. Cryst. Liq. Cryst.*, vol. 12, no. 3, pp. 193–214, Feb. 1971.

[54] I. W. Stewart, *The static and dynamic continuum theory of liquid crystals : a mathematical introduction*. Taylor & Francis, 2004.

[55] L. Onsager, “The effects of shape on the interaction of colloidal particles,” *Ann. N. Y. Acad. Sci.*, vol. 51, no. 4, pp. 627–659, May 1949.

[56] A. Saupe, “Recent Results in the Field of Liquid Crystals,” *Angew. Chemie Int. Ed. English*, vol. 7, no. 2, pp. 97–112, Feb. 1968.

[57] D. Grecov and A. D. Rey, “Transient rheology of discotic mesophases,” *Rheol. Acta*, vol. 42, no. 6, pp. 590–604, Nov. 2003.

[58] N. Noroozi and D. Grecov, “Numerical simulation of three-dimensional flow-induced microstructure in a simplified prosthetic hip joint with nematic liquid crystal lubricant,” *Rheol. Acta*, vol. 53, no. 5–6, pp. 457–465, Jun. 2014.

[59] A. Nikzad and D. Grecov, “Numerical Simulations of Nematic Liquid Crystals Flows between Eccentric Cylinders,” *Proc. 5th Int. Conf. Fluid Flow, Heat Mass Transf.*, no. 183, pp. 1–5, 2018.

[60] J. L. Ericksen, “Conservation laws for liquid crystals conservation laws for liquid crystals,” vol. 5, no. 34, pp. 1205–959, 1961.

[61] F. L.-T. Q. J. of M. and Applied and undefined 1966, “Some constitutive equations for anisotropic fluids,” *academic.oup.com*.

[62] F. M. Leslie, “Some constitutive equations for liquid crystals,” *Arch. Ration. Mech. Anal.*, vol. 28, no. 4, pp. 265–283, Jan. 1968.

[63] F. M. Leslie, “An analysis of a flow instability in nematic liquid crystals,” *J. Phys. D.*

Appl. Phys., vol. 9, no. 6, p. 925, Apr. 1976.

[64] J. N. Baleo, M. Vincent, P. Navard, and Y. Demay, “Finite element simulation of flow and director orientation of viscous anisotropic fluids in complex 2D geometries,” *J. Rheol. (N. Y. N. Y).*, vol. 36, no. 4, pp. 663–701, May 1992.

[65] R. Y. Chang, F. C. Shiao, and W. L. Yang, “Simulation of director orientation of liquid crystalline polymers in 2-D flows,” *J. Nonnewton. Fluid Mech.*, vol. 55, no. 1, pp. 1–20, Oct. 1994.

[66] M. G. Forest, R. Zhou, and Q. Wang, “Chaotic Boundaries of Nematic Polymers in Mixed Shear and Extensional Flows,” *Phys. Rev. Lett.*, vol. 93, no. 8, Aug. 2004.

[67] M. G. Forest, R. Zhou, and Q. Wang, “Scaling behavior of kinetic orientational distributions for dilute nematic polymers in weak shear,” *J. Nonnewton. Fluid Mech.*, vol. 116, no. 2–3, pp. 183–204, Jan. 2004.

[68] P. A. Cruz, M. F. Tomé, S. McKee, and I. W. Stewart, “Numerical solution of the Ericksen–Leslie model for liquid crystalline polymers free surface flows,” *J. Nonnewton. Fluid Mech.*, vol. 268, pp. 30–45, Jun. 2019.

[69] P. A. Cruz, M. F. Tomé, I. W. Stewart, and S. McKee, “Numerical solution of the Ericksen-Leslie dynamic equations for two-dimensional nematic liquid crystal flows,” *J. Comput. Phys.*, vol. 247, pp. 109–136, Aug. 2013.

[70] J. Jiao, K. Huang, and W. Liu, “Stationary Shear Flows of Nematic Liquid Crystals: A Comprehensive Study via Ericksen–Leslie Model,” vol. 34, no. 1, Feb. 2021.

[71] Y. Han, J. Yin, Y. Hu, A. Majumdar, and L. Zhang, “Solution landscapes of the simplified EricksenLeslie model and its comparisonwith the reduced LandaudeGennes model,” *Proc. R. Soc. A*, vol. 477, no. 2253, 2021.

[72] J. L. Ericksen, “Anisotropic fluids,” *Arch. Ration. Mech. Anal.*, vol. 4, no. 1, pp. 231–237, Jan. 1959.

[73] F. C. Frank, “Liquid Crystals: On the theory of liquid crystals,” *Disc. Faraday. Soc.*, vol. 25, no. I, p. 19, 1958.

[74] M. Park and H. S. Lee, “Rotational motions of repulsive graphene oxide domains in aqueous dispersion during slow shear flow,” *J. Rheol. (N. Y. N. Y).*, vol. 64, no. 1, p. 29, Nov. 2019.

[75] N. Kuzuu and M. Doi, “Constitutive equation for nematic liquid crystals under weak

velocity gradient derived from a molecular kinetic equation," *J. Phys. Soc. Japan*, vol. 52, no. 10, pp. 3486–3494, Oct. 1983.

[76] G. Marrucci, "Prediction of Leslie coefficients for rodlike polymer nematics," *Mol. Cryst. Liq. Cryst.*, vol. 72, no. 5–6, pp. 153–161, Jan. 1982.

[77] R. G. Larson, "On the relative magnitudes of viscous, elastic and texture stresses in liquid crystalline PBG solutions," *Rheol. Acta*, vol. 35, no. 2, pp. 150–159, 1996.

[78] A. M.-E. D. SERIES and U. 2001, "Measurement of viscoelastic coefficients for nematic mesophases using magnetic resonance," *INSPEC Publ.*, pp. 405–413, 2001.

[79] D. Baalss and S. Hess, "The Viscosity Coefficients of Oriented Nematic and Nematic Discotic Liquid Crystals; Affine Transformation Model," *Zeitschrift für Naturforsch. A*, vol. 43, no. 7, pp. 662–670, Jan. 1988.

[80] T. CARLSSON, "POSSIBILITY OF THE EXISTENCE OF A POSITIVE LESLIE VISCOSITY″ALPHA″ 2. PROPOSED FLOW BEHAVIOR OF DISK LIKE NEMATIC LIQUID CRYSTALS.," *MOL CRYST LIQ CRYST*, vol. V 89, no. N 1-4, pp. 57–66, 1982.

[81] M. Kröger and S. Sellers, "Viscosities of nematic and discotic nematic liquid crystals according to the affine transformation model," *Mol. Cryst. Liq. Cryst. Sci. Technol. Sect. A. Mol. Cryst. Liq. Cryst.*, vol. 300, no. 1, pp. 245–262, Jul. 1997.

[82] C. W. Oseen, "The theory of liquid crystals," *Trans. Faraday Soc.*, vol. 29, no. 140, p. 883, Jan. 1933.

[83] N. Noroozi and D. Grecov, "Numerical simulation of flow and structure in nematic liquid crystalline materials between eccentric cylinders," *J. Nonnewton. Fluid Mech.*, vol. 208–209, pp. 1–17, Jun. 2014.

[84] M. J. Pospisil, P. Saha, S. Abdulquddos, M. M. Noor, V. A. Davis, and M. J. Green, "Orientation Relaxation Dynamics in Cellulose Nanocrystal Dispersions in the Chiral Liquid Crystalline Phase," *Langmuir*, vol. 34, no. 44, pp. 13274–13282, Nov. 2018.

[85] D. G. Venhaus, K. S. Conatser, and M. J. Green, "Dynamics of chiral liquid crystals under applied shear," vol. 40, no. 6, pp. 846–853, Jun. 2013.

[86] X. Yang, M. G. Forest, W. Mullins, and Q. Wang, "Dynamic defect morphology and hydrodynamics of sheared nematic polymers in two space dimensions," *J. Rheol. (N. Y. N. Y).*, vol. 53, no. 3, pp. 589–615, May 2009.

[87] T. Tsuji and A. D. Rey, “Effect of long range order on sheared liquid crystalline materials Part 1: compatibility between tumbling behavior and fixed anchoring,” *J. Nonnewton. Fluid Mech.*, vol. 73, no. 1–2, pp. 127–152, Nov. 1997.

[88] A. P. Singh and A. D. Rey, “Microstructure constitutive equation for discotic nematic liquid crystalline materials -,” *Rheol. Acta*, vol. 37, no. 4, pp. 374–386, Aug. 1998.

[89] Tsuji and Rey, “Effect of long range order on sheared liquid crystalline materials: flow regimes, transitions, and rheological phase diagrams,” *Phys. Rev. E. Stat. Phys. Plasmas. Fluids. Relat. Interdiscip. Topics*, vol. 62, no. 6 Pt A, pp. 8141–51, Dec. 2000.

[90] D. Grecov and A. D. Rey, “Steady state and transient rheological behavior of mesophase pitch, Part II: Theory,” *J. Rheol. (N. Y. N. Y).*, vol. 49, no. 1, pp. 175–195, Jan. 2005.

[91] E. Orlandini, D. Marenduzzo, and J. M. Yeomans, “Viscoelastic Flows of Cholesteric Liquid Crystals,” *http://dx.doi.org/10.1080/15421400701205347*, vol. 465, no. 1, pp. 1–14, Apr. 2010.

[92] D. Marenduzzo, E. Orlandini, and J. M. Yeomans, “Rheology of distorted nematic liquid crystals,” *EPL (Europhysics Lett.*, vol. 64, no. 3, p. 406, Nov. 2003.

[93] T. Tsuji and A. D. Rey, “Orientation mode selection mechanisms for sheared nematic liquid crystalline materials,” *Phys. Rev. E*, vol. 57, no. 5, p. 5609, May 1998.

[94] W. Helfrich, “Capillary Flow of Cholesteric and Smectic Liquid Crystals,” *Phys. Rev. Lett.*, vol. 23, no. 7, p. 372, Aug. 1969.

[95] K. Hongladarom, V. Secakusuma, and W. R. Burghardt, “Relation between molecular orientation and rheology in lyotropic hydroxypropylcellulose solutions,” *J. Rheol. (N. Y. N. Y).*, vol. 38, no. 5, p. 1505, Jun. 1998.

[96] D. Marenduzzo, E. Orlandini, and J. M. Yeomans, “Permeative flows in cholesterics: Shear and Poiseuille flows,” *J. Chem. Phys.*, vol. 124, no. 20, p. 204906, May 2006.

[97] F. Fadda, G. Gonnella, A. Lamura, E. Orlandini, and A. Tiribocchi, “Rheology of an Inverted Cholesteric Droplet under Shear Flow,” *Fluids 2018, Vol. 3, Page 47*, vol. 3, no. 3, p. 47, Jul. 2018.

[98] H. Zhang, Y. Zhang, Y. Wang, M. Gao, L. Zhang, and Q. Xu, “Director configuration of liquid crystals in a cylindrical cavity with homeotropic anchoring conditions,” *https://doi.org/10.1080/00268976.2021.1966532*, 2021.

[99] O. Wiese, D. Marenduzzo, and O. Henrich, “Microfluidic flow of cholesteric liquid

crystals," *Soft Matter*, vol. 12, no. 45, pp. 9223–9237, Nov. 2016.

[100] T. E. Fischer, S. Bhattacharya, R. Salher, J. L. Lauer, and Y. J. Ahn, "Lubrication by a Smectic Liquid Crystal," *http://dx.doi.org/10.1080/10402008808981846*, vol. 31, no. 4, pp. 442–448, 2008.

[101] C. H. A. Cheng, L. H. Kellogg, S. Shkoller, and D. L. Turcotte, "A liquid-crystal model for friction," *Proc. Natl. Acad. Sci. U. S. A.*, vol. 105, no. 23, pp. 7930–7935, Jun. 2008.

[102] A. Nikzad, A. Akbari, and D. Grecov, "Rheological properties of discotic nematic liquid crystals: graphene oxide dispersions study," *Liq. Cryst.*, 2021.

[103] I. M. Dris and E. S. g. Shaqfeh, "Experimental and theoretical observations of elastic instabilities in eccentric cylinder flows: local versus global instability," *J. Nonnewton. Fluid Mech.*, vol. 80, no. 1, pp. 1–58, Dec. 1998.

[104] I. Dris and E. S. g. Shaqfeh, "Flow of a viscoelastic fluid between eccentric cylinders: impact on flow stability," *J. Nonnewton. Fluid Mech.*, vol. 80, no. 1, pp. 59–87, Dec. 1998.

[105] B. Y. Ballal and R. S. Rivlin, "Flow of a Newtonian fluid between eccentric rotating cylinders: Inertial effects," *Arch. Ration. Mech. Anal.*, vol. 62, no. 3, pp. 237–294, 1976.

[106] G. Tian, M. Wang, X. Wang, and G. Jin, "Flow between eccentric cylinders: a shear-extensional controllable flow," *Journal*, vol. 28, no. 2, pp. 139–148, 2016.

[107] J. Xiang, E. Hajizadeh, R. G. Larson, and D. Nelson, "Predictions of polymer migration in a dilute solution between rotating eccentric cylinders," *J. Rheol. (N. Y. N. Y).*, vol. 65, no. 6, p. 1311, Sep. 2021.

[108] J. Li, X. Zeng, T. Ren, and E. van der Heide, "The Preparation of Graphene Oxide and Its Derivatives and Their Application in Bio-Tribological Systems," *Lubricants*, vol. 2, no. 3, pp. 137–161, Sep. 2014.

[109] D. Grecov and J.-R. Clermont, "Numerical simulations of non-stationary flows of non-Newtonian fluids between concentric and eccentric cylinders by stream-tube method and domain decomposition," *Rheol. Acta*, vol. 47, no. 5–6, pp. 609–620, Jul. 2008.

[110] S. Naficy *et al.*, "Graphene oxide dispersions: tuning rheology to enable fabrication," *Mater. Horiz.*, vol. 1, no. 3, pp. 326–331, Apr. 2014.

[111] C. Vallés, R. J. Young, D. J. Lomax, and I. A. Kinloch, "The rheological behaviour of concentrated dispersions of graphene oxide," *J. Mater. Sci.*, vol. 49, no. 18, pp. 6311–

6320, Sep. 2014.

[112] P. Kumar, U. N. Maiti, K. E. Lee, and S. O. Kim, “Rheological properties of graphene oxide liquid crystal,” *Carbon N. Y.*, vol. 80, no. 1, pp. 453–461, Dec. 2014.

[113] D. Grecov, L. R. P. De Andrade Lima, and A. D. Rey, “Multiscale simulation of flow-induced texture formation in polymer liquid crystals and carbonaceous mesophases,” in *Molecular Simulation*, 2005, vol. 31, no. 2–3, pp. 185–199.

[114] H. Brenner, “Rheology of a dilute suspension of axisymmetric Brownian particles,” *Int. J. Multiph. Flow*, vol. 1, no. 2, pp. 195–341, Apr. 1974.

[115] A. Acevedo, A. Patricia M. Cotts, A. D. Shine, P. M. Cotts, and Annette D. Shine, “Molecular weight dependence of the rotational diffusivity of rodlike polymers in concentrated nematic solutions,” 2005.

[116] L. R. P. de Andrade Lima and A. D. Rey, “Pulsatile flow of discotic mesophases,” *Chem. Eng. Sci.*, vol. 60, no. 23, pp. 6622–6636, Dec. 2005.

[117] W. S. Hummers and R. E. Offeman, “Preparation of Graphitic Oxide,” *J. Am. Chem. Soc.*, vol. 80, no. 6, pp. 1339–1339, Mar. 1958.

[118] D. Yang *et al.*, “Chemical analysis of graphene oxide films after heat and chemical treatments by X-ray photoelectron and Micro-Raman spectroscopy,” *Carbon N. Y.*, vol. 47, no. 1, pp. 145–152, Jan. 2009.

[119] B. Dan *et al.*, “Liquid crystals of aqueous, giant graphene oxide flakes,” *Soft Matter*, vol. 7, no. 23, p. 11154, Nov. 2011.

[120] R. Tkacz, R. Oldenbourg, S. B. Mehta, M. Miansari, A. Verma, and M. Majumder, “pH dependent isotropic to nematic phase transitions in graphene oxide dispersions reveal droplet liquid crystalline phases,” *Chem. Commun.*, vol. 50, no. 50, pp. 6668–6671, May 2014.

[121] R. Tkacz, R. Oldenbourg, A. Fulcher, M. Miansari, and M. Majumder, “Capillary-Force-Assisted Self-Assembly (CAS) of Highly Ordered and Anisotropic Graphene-Based Thin Films,” *J. Phys. Chem. C*, vol. 118, no. 1, pp. 259–267, Jan. 2014.

[122] F. Del Giudice, B. V. Cunning, R. S. Ruoff, and A. Q. Shen, “Filling the gap between transient and steady shear rheology of aqueous graphene oxide dispersions,” *Rheol. Acta*, vol. 57, no. 4, pp. 293–306, Apr. 2018.

[123] M. Kröger and S. Sellers, “On the signs of the Leslie viscosities α 2 and α 3 for nematics

and discotic nematics," *Mol. Cryst. Liq. Cryst. Sci. Technol. Sect. A. Mol. Cryst. Liq. Cryst.*, vol. 293, no. 1, pp. 17–27, Feb. 1997.

[124] L. R. P. de Andrade Lima and A. D. Rey, "Poiseuille flow of Leslie-Ericksen discotic liquid crystal: Solution multiplicity, multistability, and non-Newtonian rheology," *J. Nonnewton. Fluid Mech.*, vol. 110, no. 2–3, pp. 103–142, Mar. 2003.

[125] R. J. Atkin and F. M. Leslie, "Couette flow of nematic liquid crystals," *Q. J. Mech. Appl. Math.*, vol. 23, no. 2, pp. 3–24, May 1970.

[126] R. J. Atkin, "Poiseuille flow of liquid crystals of the nematic type," *Arch. Ration. Mech. Anal.*, vol. 38, no. 3, pp. 224–240, Jan. 1970.

[127] A. S. K. K. Ho and A. D. Rey, "Orienting properties of discotic nematic liquid crystals in Jeffrey-Hamel flows," *Rheol. Acta*, vol. 30, no. 1, pp. 77–88, Jan. 1991.

[128] S. Chono, T. Tsuji, and M. M. Denn, "Spatial development of director orientation of tumbling nematic liquid crystals in pressure-driven channel flow," *J. Nonnewton. Fluid Mech.*, vol. 79, no. 2–3, pp. 515–527, Nov. 1998.

[129] P. A. Cruz, M. F. Tomé, I. W. Stewart, and S. McKee, "A numerical method for solving the dynamic three-dimensional Ericksen-Leslie equations for nematic liquid crystals subject to a strong magnetic field," *J. Nonnewton. Fluid Mech.*, vol. 165, no. 3–4, pp. 143–157, Feb. 2010.

[130] T. G. Anderson, E. Mema, L. Kondic, and L. J. Cummings, "Transitions in Poiseuille flow of nematic liquid crystal," *Int. J. Non. Linear. Mech.*, vol. 75, pp. 15–21, Oct. 2015.

[131] J. Q. Carou, B. R. Duffy, N. J. Mottram, and S. K. Wilson, "Shear-driven and pressure-driven flow of a nematic liquid crystal in a slowly varying channel," *Phys. Fluids*, vol. 18, no. 2, 2006.

[132] F. M. Leslie, "Some constitutive equations for anisotropic fluids."

[133] M. Miesowicz, "The three coefficients of viscosity of anisotropic liquids," *Nature*, vol. 158, no. 4001, pp. 27–27, 1946.

[134] A. D. Rey and T. Tsuji, "Recent advances in theoretical liquid crystal rheology," *Macromol. Theory Simulations*, vol. 7, no. 6, pp. 623–639, Nov. 1998.

[135] G. W. de Kort, N. Leoné, E. Stellamanns, D. Auhl, C. H. R. M. Wilsens, and S. Rastogi, "Effect of Shear Rate on the Orientation and Relaxation of a Vanillic Acid Based Liquid Crystalline Polymer," *Polym. 2018, Vol. 10, Page 935*, vol. 10, no. 9, p. 935, Aug. 2018.

[136] G. M. Choi, M. Park, S. Y. Jeong, and H. S. Lee, “Orientation effect on the rheology of graphene oxide dispersions in isotropic phase, ordered isotropic biphase, and discotic phase,” *J. Rheol. (N. Y. N. Y).*, vol. 65, no. 5, p. 791, Jul. 2021.

[137] F. Del Giudice and A. Q. Shen, “Shear rheology of graphene oxide dispersions,” *Curr. Opin. Chem. Eng.*, vol. 16, pp. 23–30, May 2017.

[138] A. M. Adnan, C. Lü, X. Luo, and J. Wang, “Impact of Graphene Oxide on Zero Shear Viscosity, Fatigue Life and Low-Temperature Properties of Asphalt Binder,” *Mater. 2021, Vol. 14, Page 3073*, vol. 14, no. 11, p. 3073, Jun. 2021.

[139] W. Tesfai, P. Singh, Y. Shatilla, M. Z. Iqbal, and A. A. Abdala, “Rheology and microstructure of dilute graphene oxide suspension,” *JNR*, vol. 15, no. 10, p. 1989, Oct. 2013.

[140] C. F. Dietrich, P. J. Collings, T. Sottmann, P. Rudquist, and F. Giesselmann, “Extremely small twist elastic constants in lyotropic nematic liquid crystals,” *Proc. Natl. Acad. Sci. U. S. A.*, vol. 117, no. 44, pp. 27238–27244, Nov. 2020.

[141] J. P. Straley, “Frank elastic constants of the hard-rod liquid crystal,” *Phys. Rev. A*, vol. 8, no. 4, p. 2181, 1973.

[142] M. J. Bradshaw, E. P. Raynes, J. D. Bunning, and T. E. Faber, “The Frank constants of some nematic liquid crystals,” *J. Phys.*, vol. 46, no. 9, pp. 1513–1520, 1985.

[143] G. De Luca and A. D. Rey, “Chiral front propagation in liquid-crystalline materials: Formation of the planar monodomain twisted plywood architecture of biological fibrous composites,” *Phys. Rev. E*, vol. 69, no. 1, p. 011706, Jan. 2004.

[144] A. D. Rey, “Liquid crystal models of biological materials and processes,” *Soft Matter*, vol. 6, no. 15, pp. 3402–3429, Jul. 2010.

[145] D. H. Klein, L. G. Leal, C. J. García-Cervera, and H. D. Ceniceros, “Ericksen number and Deborah number cascade predictions of a model for liquid crystalline polymers for simple shear flow,” *Phys. Fluids*, vol. 19, no. 2, p. 023101, Feb. 2007.

Appendix A:Landau de-Gennes Derivations

Jaumann derivatives of order parameter tensor:

$$\widehat{\mathbf{Q}}_{11} = \frac{\partial \mathbf{Q}_{11}}{\partial \tilde{t}} + \tilde{\mathbf{u}}\frac{\partial \mathbf{Q}_{11}}{\partial \tilde{x}} + \tilde{\mathbf{v}}\frac{\partial \mathbf{Q}_{11}}{\partial \tilde{y}} + \tilde{\mathbf{w}}\frac{\partial \mathbf{Q}_{11}}{\partial \tilde{z}} - 2\widetilde{\mathbf{W}}_{12}\mathbf{Q}_{12} - 2\widetilde{\mathbf{W}}_{13}\mathbf{Q}_{13}$$

$$\widehat{\mathbf{Q}}_{22} = \frac{\partial \mathbf{Q}_{22}}{\partial \tilde{t}} + \tilde{\mathbf{u}}\frac{\partial \mathbf{Q}_{22}}{\partial \tilde{x}} + \tilde{\mathbf{v}}\frac{\partial \mathbf{Q}_{22}}{\partial \tilde{y}} + \tilde{\mathbf{w}}\frac{\partial \mathbf{Q}_{22}}{\partial \tilde{z}} + 2\widetilde{\mathbf{W}}_{12}\mathbf{Q}_{12} - 2\widetilde{\mathbf{W}}_{23}\mathbf{Q}_{23}$$

$$\widehat{\mathbf{Q}}_{12} = \frac{\partial \mathbf{Q}_{12}}{\partial \tilde{t}} + \tilde{\mathbf{u}}\frac{\partial \mathbf{Q}_{12}}{\partial \tilde{\mathbf{x}}} + \tilde{\mathbf{v}}\frac{\partial \mathbf{Q}_{12}}{\partial \tilde{y}} + \tilde{\mathbf{w}}\frac{\partial \mathbf{Q}_{12}}{\partial \tilde{z}} - \widetilde{\mathbf{W}}_{12}(\mathbf{Q}_{22} - \mathbf{Q}_{11}) - \widetilde{\mathbf{W}}_{13}\mathbf{Q}_{23} - \widetilde{\mathbf{W}}_{23}\mathbf{Q}_{13}$$

$$\widehat{\mathbf{Q}}_{13} = \frac{\partial \mathbf{Q}_{13}}{\partial \tilde{t}} + \tilde{\mathbf{u}}\frac{\partial \mathbf{Q}_{13}}{\partial \tilde{x}} + \tilde{\mathbf{v}}\frac{\partial \mathbf{Q}_{13}}{\partial \tilde{y}} + \tilde{\mathbf{w}}\frac{\partial \mathbf{Q}_{13}}{\partial \tilde{z}} - \widetilde{\mathbf{W}}_{13}(\mathbf{Q}_{33} - \mathbf{Q}_{11}) - \widetilde{\mathbf{W}}_{12}\mathbf{Q}_{23} + \widetilde{\mathbf{W}}_{23}\mathbf{Q}_{12}$$

$$\widehat{\mathbf{Q}}_{23} = \frac{\partial \mathbf{Q}_{23}}{\partial \tilde{\mathbf{t}}} + \tilde{\mathbf{u}}\frac{\partial \mathbf{Q}_{23}}{\partial \tilde{\tilde{r}}} + \tilde{\mathbf{v}}\frac{\partial \mathbf{Q}_{23}}{\partial \tilde{u}} + \tilde{\mathbf{w}}\frac{\partial \mathbf{Q}_{23}}{\partial \tilde{\mathbf{y}}} - \widetilde{\mathbf{W}}_{23}(\mathbf{Q}_{33} - \mathbf{Q}_{22}) + \widetilde{\mathbf{W}}_{12}\mathbf{Q}_{13} + \widetilde{\mathbf{W}}_{13}\mathbf{Q}_{12}$$

Short-range elasticity:

$$\mathbf{H}_{11}^{sr} = \frac{1}{De}\left[\left(\frac{U}{3} - 1\right)\mathbf{Q}_{11} + U(\mathbf{Q}_{11}^2 + \mathbf{Q}_{12}^2 + \mathbf{Q}_{13}^2) + U(\mathbf{Q}{:}\,\mathbf{Q}) \cdot \left(\mathbf{Q}_{11} + \frac{1}{3}\right)\right]$$

$$\mathbf{H}_{22}^{sr} = \frac{1}{De}\left[\left(\frac{U}{3} - 1\right)\mathbf{Q}_{22} + U(\mathbf{Q}_{12}^2 + \mathbf{Q}_{22}^2 + \mathbf{Q}_{23}^2) + U(\mathbf{Q}{:}\,\mathbf{Q}) \cdot \left(\mathbf{Q}_{22} + \frac{1}{3}\right)\right]$$

$$\mathbf{H}_{12}^{sr} = \frac{1}{De}\left[\left(\frac{U}{3} - 1\right)\mathbf{Q}_{12} + U(\mathbf{Q}_{11}\mathbf{Q}_{12} + \mathbf{Q}_{12}\mathbf{Q}_{22} + \mathbf{Q}_{13}\mathbf{Q}_{23}) + U(\mathbf{Q}{:}\,\mathbf{Q})\mathbf{Q}_{12}\right]$$

$$\mathbf{H}_{13}^{sr} = \frac{1}{De}\left[\left(\frac{U}{3} - 1\right)\mathbf{Q}_{13} + U(\mathbf{Q}_{11}\mathbf{Q}_{13} + \mathbf{Q}_{12}\mathbf{Q}_{23} + \mathbf{Q}_{13}\mathbf{Q}_{33}) + U(\mathbf{Q}{:}\,\mathbf{Q})\mathbf{Q}_{13}\right]$$

$$\mathbf{H}_{23}^{sr} = \frac{1}{De}\left[\left(\frac{U}{3} - 1\right)\mathbf{Q}_{23} + U(\mathbf{Q}12\mathbf{Q}_{13} + \mathbf{Q}_{22}\mathbf{Q}_{23} + \mathbf{Q}_{23}\mathbf{Q}_{33}) + U(\mathbf{Q}{:}\,\mathbf{Q})\mathbf{Q}_{23}\right]$$

Long-range elasticity:

$$\mathbf{H}_{11}^{lr} = \frac{1}{Er}\left[\widetilde{\nabla}^2\mathbf{Q}_{11} + \frac{L^*}{3}\left(2\frac{\partial^2\mathbf{Q}_{11}}{\partial\tilde{x}^2} + \frac{\partial^2\mathbf{Q}_{12}}{\partial\tilde{x}\,\partial\tilde{y}} + \frac{\partial^2\mathbf{Q}_{13}}{\partial\tilde{y}\,\partial\tilde{z}} - \frac{\partial^2\mathbf{Q}_{22}}{\partial\tilde{y}^2} + 2\frac{\partial^2\mathbf{Q}_{23}}{\partial\tilde{y}\,\partial\tilde{z}} - \frac{\partial^2\mathbf{Q}_{33}}{\partial\tilde{z}^2}\right)\right]$$

$$\mathbf{H}_{22}^{lr} = \frac{1}{Er}\left[\widetilde{\nabla}^2\mathbf{Q}_{22} + \frac{L^*}{3}\left(\frac{\partial^2\mathbf{Q}_{12}}{\partial\tilde{x}\tilde{y}} - \frac{\partial^2\mathbf{Q}_{11}}{\partial\tilde{x}^2} - 2\frac{\partial^2\mathbf{Q}_{13}}{\partial\tilde{x}\,\partial\tilde{z}} + 2\frac{\partial^2\mathbf{Q}_{22}}{\partial\tilde{y}^2} + \frac{\partial^2\mathbf{Q}_{23}}{\partial\tilde{y}\,\partial\tilde{z}} - \frac{\partial^2\mathbf{Q}_{33}}{\partial\tilde{z}^2}\right)\right]$$

$$\mathbf{H}_{12}^{lr} = \frac{1}{Er}\left[\widetilde{\nabla}^2\mathbf{Q}_{12} + \frac{L^*}{2}\left(\frac{\partial^2\mathbf{Q}_{11}}{\partial\tilde{x}\,\partial\tilde{y}} + \frac{\partial^2\mathbf{Q}_{12}}{\partial\tilde{x}^2} + \frac{\partial^2\mathbf{Q}_{12}}{\partial\tilde{y}^2} + \frac{\partial^2\mathbf{Q}_{13}}{\partial\tilde{y}\,\partial\tilde{z}} + \frac{\partial^2\mathbf{Q}_{22}}{\partial\tilde{x}\,\partial\tilde{y}} + \frac{\partial^2\mathbf{Q}_{23}}{\partial\tilde{x}\,\partial\tilde{z}}\right)\right]$$

$$\mathbf{H}_{13}^{lr} = \frac{1}{Er}\left[\widetilde{\nabla}^2\mathbf{Q}_{13} + \frac{L^*}{2}\left(\frac{\partial^2\mathbf{Q}_{11}}{\partial\tilde{x}\,\partial\tilde{z}} + \frac{\partial^2\mathbf{Q}_{12}}{\partial\tilde{y}\,\partial\tilde{z}} + \frac{\partial^2\mathbf{Q}_{13}}{\partial\tilde{x}^2} + \frac{\partial^2\mathbf{Q}_{13}}{\partial\tilde{z}^2} + \frac{\partial^2\mathbf{Q}_{23}}{\partial\tilde{x}\,\partial\tilde{y}} + \frac{\partial^2\mathbf{Q}_{33}}{\partial\tilde{x}\,\partial\tilde{z}}\right)\right]$$

$$\mathbf{H}_{23}^{lr} = \frac{1}{Er}\left[\widetilde{\nabla}^2\mathbf{Q}_{23} + \frac{L^*}{2}\left(\frac{\partial^2\mathbf{Q}_{12}}{\partial\tilde{x}\,\partial\tilde{z}} + \frac{\partial^2\mathbf{Q}_{13}}{\partial\tilde{x}\,\partial\tilde{y}} + \frac{\partial^2\mathbf{Q}_{22}}{\partial\tilde{y}\,\partial\tilde{z}} + \frac{\partial^2\mathbf{Q}_{23}}{\partial\tilde{y}^2} + \frac{\partial^2\mathbf{Q}_{23}}{\partial\tilde{z}^2} + \frac{\partial^2\mathbf{Q}_{33}}{\partial\tilde{y}\,\partial\tilde{z}}\right)\right]$$

Flow contributions:

$$\begin{aligned}\mathbf{F}_{11} = {} & \frac{2}{3}\beta\left(\widetilde{\mathbf{A}}_{11} + 2\widetilde{\mathbf{A}}_{11}\mathbf{Q}_{11} + \widetilde{\mathbf{A}}_{12}\mathbf{Q}_{12} + \widetilde{\mathbf{A}}_{13}\mathbf{Q}_{13} - \widetilde{\mathbf{A}}_{22}\mathbf{Q}_{22} - 2\widetilde{\mathbf{A}}_{23}\mathbf{Q}_{23} - \widetilde{\mathbf{A}}_{33}\mathbf{Q}_{33}\right) \\ & -\frac{1}{2}\beta\left[\widetilde{\mathbf{A}}_{11}(3\mathbf{Q}_{11}^2 + \mathbf{Q}_{12}^2 + \mathbf{Q}_{13}^2) + 4\widetilde{\mathbf{A}}_{12}\mathbf{Q}_{11}\mathbf{Q}_{12} + 4\widetilde{\mathbf{A}}_{13}\mathbf{Q}_{11}\mathbf{Q}_{13}\right. \\ & +\widetilde{\mathbf{A}}_{22}(\mathbf{Q}_{11}\mathbf{Q}_{22} - \mathbf{Q}_{22}^2 - \mathbf{Q}_{23}^2) + 2\widetilde{\mathbf{A}}_{23}\mathbf{Q}_{23}(\mathbf{Q}_{11} - \mathbf{Q}_{22} - \mathbf{Q}_{33}) \\ & \left.+\widetilde{\mathbf{A}}_{33}(\mathbf{Q}_{11}\mathbf{Q}_{33} - \mathbf{Q}_{23}^2 - \mathbf{Q}_{33}^2)\right]\end{aligned}$$

$$\begin{aligned}\mathbf{F}_{22} = {} & \frac{2}{3}\beta\left(\widetilde{\mathbf{A}}_{22} - \widetilde{\mathbf{A}}_{11}\mathbf{Q}_{11} + \widetilde{\mathbf{A}}_{12}\mathbf{Q}_{12} - 2\widetilde{\mathbf{A}}_{13}\mathbf{Q}_{13} + 2\widetilde{\mathbf{A}}_{22}\mathbf{Q}_{22} + \widetilde{\mathbf{A}}_{23}\mathbf{Q}_{23} - \widetilde{\mathbf{A}}_{33}\mathbf{Q}_{33}\right) \\ & -\frac{1}{2}\beta\left[\widetilde{\mathbf{A}}_{22}(3\mathbf{Q}_{22}^2 - \mathbf{Q}_{11} - \mathbf{Q}_{13}^2) + 4\widetilde{\mathbf{A}}_{12}\mathbf{Q}_{12}\mathbf{Q}_{22} + 4\widetilde{\mathbf{A}}_{23}\mathbf{Q}_{23}\mathbf{Q}_{22}\right. \\ & +\widetilde{\mathbf{A}}_{11}(\mathbf{Q}_{11}\mathbf{Q}_{22} - \mathbf{Q}_{11}^2 - \mathbf{Q}_{13}^2) + 2\widetilde{\mathbf{A}}_{13}\mathbf{Q}_{13}(\mathbf{Q}_{22} - \mathbf{Q}_{11} - \mathbf{Q}_{33}) \\ & \left.+\widetilde{\mathbf{A}}_{33}(\mathbf{Q}_{22}\mathbf{Q}_{33} - \mathbf{Q}_{13}^2 - \mathbf{Q}_{33}^2)\right]\end{aligned}$$

$$\mathbf{F}_{12} = \frac{2}{3}\beta\widetilde{\mathbf{A}}_{12} + \beta\left[\widetilde{\mathbf{A}}_{11}\mathbf{Q}_{12} + \widetilde{\mathbf{A}}_{12}(\mathbf{Q}_{11} + \mathbf{Q}_{22}) + \widetilde{\mathbf{A}}_{13}\mathbf{Q}_{23} + \widetilde{\mathbf{A}}_{22}\mathbf{Q}_{12} + \widetilde{\mathbf{A}}_{23}\mathbf{Q}_{13}\right]$$
$$-\frac{1}{2}\beta\left[\widetilde{\mathbf{A}}_{11}(3\mathbf{Q}_{11}\mathbf{Q}_{12} + \mathbf{Q}_{12}\mathbf{Q}_{22} + \mathbf{Q}_{13}\mathbf{Q}_{23}) + 4\widetilde{\mathbf{A}}_{13}\mathbf{Q}_{12}\mathbf{Q}_{13} + 4\widetilde{\mathbf{A}}_{23}\mathbf{Q}_{12}\mathbf{Q}_{23}\right.$$
$$+\widetilde{\mathbf{A}}_{22}(3\mathbf{Q}_{12}\mathbf{Q}_{22} + \mathbf{Q}_{11}\mathbf{Q}_{12} + \mathbf{Q}_{13}\mathbf{Q}_{23}) + \widetilde{\mathbf{A}}_{33}(\mathbf{Q}_{12}\mathbf{Q}_{33} + \mathbf{Q}_{13}\mathbf{Q}_{23})$$
$$\left.+\widetilde{\mathbf{A}}_{12}(\mathbf{Q}_{11}^2 + 5\mathbf{Q}_{12}^2 + \mathbf{Q}_{13}^2 + \mathbf{Q}_{22}^2 + \mathbf{Q}_{23}^2 + \mathbf{Q}_{11}\mathbf{Q}_{22})\right]$$
$$\mathbf{F}_{13} = \frac{2}{3}\beta\widetilde{\mathbf{A}}_{13} + \beta\left[\widetilde{\mathbf{A}}_{11}\mathbf{Q}_{13} + \widetilde{\mathbf{A}}_{12}\mathbf{Q}_{23} + \widetilde{\mathbf{A}}_{13}(\mathbf{Q}_{11} + \mathbf{Q}_{33}) + \widetilde{\mathbf{A}}_{23}\mathbf{Q}_{12} + \widetilde{\mathbf{A}}_{33}\mathbf{Q}_{13}\right]$$
$$-\frac{1}{2}\beta\left[\widetilde{\mathbf{A}}_{11}(3\mathbf{Q}_{11}\mathbf{Q}_{13} + \mathbf{Q}_{12}\mathbf{Q}_{23} + \mathbf{Q}_{13}\mathbf{Q}_{33}) + 4\widetilde{\mathbf{A}}_{12}\mathbf{Q}_{12}\mathbf{Q}_{13} + 4\widetilde{\mathbf{A}}_{23}\mathbf{Q}_{13}\mathbf{Q}_{23}\right.$$
$$+\widetilde{\mathbf{A}}_{22}(\mathbf{Q}_{13}\mathbf{Q}_{22} + \mathbf{Q}_{12}\mathbf{Q}_{23}) + \widetilde{\mathbf{A}}_{33}(3\mathbf{Q}_{13}\mathbf{Q}_{33} + \mathbf{Q}_{11}\mathbf{Q}_{13} + \mathbf{Q}_{12}\mathbf{Q}_{23})$$
$$\left.+\widetilde{\mathbf{A}}_{13}(\mathbf{Q}_{11}^2 + \mathbf{Q}_{12}^2 + 5\mathbf{Q}_{13}^2 + \mathbf{Q}_{23}^2 + \mathbf{Q}_{33}^2 + \mathbf{Q}_{11}\mathbf{Q}_{33})\right]$$
$$\boldsymbol{F}_{23} = \frac{2}{3}\beta\widetilde{\mathbf{A}}_{23} + \beta\left[\widetilde{\mathbf{A}}_{12}\mathbf{Q}_{13} + \widetilde{\mathbf{A}}_{13}\mathbf{Q}_{12} + \widetilde{\mathbf{A}}_{22}\mathbf{Q}_{23} + \widetilde{\mathbf{A}}_{23}(\mathbf{Q}_{22} + \mathbf{Q}_{33}) + \widetilde{\mathbf{A}}_{33}\mathbf{Q}_{23}\right]$$
$$-\frac{1}{2}\beta\left[\widetilde{\mathbf{A}}_{22}(3\mathbf{Q}_{22}\mathbf{Q}_{23} + \mathbf{Q}_{12}\mathbf{Q}_{13} + \mathbf{Q}_{23}\mathbf{Q}_{33}) + 4\widetilde{\mathbf{A}}_{12}\mathbf{Q}_{12}\mathbf{Q}_{23} + 4\widetilde{\mathbf{A}}_{13}\mathbf{Q}_{13}\mathbf{Q}_{23}\right.$$
$$+\widetilde{\mathbf{A}}_{11}(\mathbf{Q}_{11}\mathbf{Q}_{23} + \mathbf{Q}_{12}\mathbf{Q}_{13}) + \widetilde{\mathbf{A}}_{33}(3\mathbf{Q}_{23}\mathbf{Q}_{33} + \mathbf{Q}_{12}\mathbf{Q}_{13} + \mathbf{Q}_{22}\mathbf{Q}_{23})$$
$$\left.+\widetilde{\mathbf{A}}_{23}(\mathbf{Q}_{12}^2 + \mathbf{Q}_{13}^2 + \mathbf{Q}_{22}^2 + 5\mathbf{Q}_{23}^2 + \mathbf{Q}_{33}^2 + \mathbf{Q}_{22}\mathbf{Q}_{33})\right]$$

Symmetric viscous component of total stress tensor:

$$\tau_{v11} = \tilde{\nu}_1\widetilde{\mathbf{A}}_{11} + 2\tilde{\nu}_2\left[\widetilde{\mathbf{A}}_{11}\mathbf{Q}_{11} + \widetilde{\mathbf{A}}_{12}\mathbf{Q}_{12} + \widetilde{\mathbf{A}}_{13}\mathbf{Q}_{13} - \frac{\mathbf{Q}}{3}\right]$$
$$+\tilde{\nu}_4\left[\mathrm{QQ}\widetilde{\mathbf{A}} + \mathbf{Q}\widetilde{\mathbf{A}}\mathbf{Q}_{11} + \widetilde{\mathbf{A}}_{11}(3\mathbf{Q}_{11}^2 + 2\mathbf{Q}_{12}^2 + 2\mathbf{Q}_{13}^2) + 2\widetilde{\mathbf{A}}_{12}(\mathbf{Q}_{12}(2\mathbf{Q}_{11} + \mathbf{Q}_{22}) + \mathbf{Q}_{13}\mathbf{Q}_{23})\right.$$
$$\left.+2\widetilde{\mathrm{A}}_{13}(\mathbf{Q}_{13}(2\mathrm{Q}_{11} + \mathbf{Q}_{33}) + \mathbf{Q}_{12}\mathbf{Q}_{23}) + \widetilde{\mathrm{A}}_{22}\mathbf{Q}_{12}^2 + 2\widetilde{\mathrm{A}}_{23}\mathbf{Q}_{12}\mathbf{Q}_{13} + \widetilde{\mathrm{A}}_{33}\mathbf{Q}_{13}^2\right]$$

$$\tau_{v22} = \tilde{\nu}_1\widetilde{\mathrm{A}}_{22} + 2\tilde{\nu}_2\left[\widetilde{\mathrm{A}}_{12}\mathrm{Q}_{12} + \widetilde{\mathrm{A}}_{22}\mathrm{Q}_{22} + \widetilde{\mathrm{A}}_{23}\mathrm{Q}_{23} - \frac{\mathrm{QA}}{3}\right]$$
$$+\tilde{\nu}_4\left[\mathrm{QQ}\widetilde{\mathrm{A}} + \mathrm{Q}\widetilde{\mathrm{A}}\mathbf{Q}_{22} + \widetilde{\mathrm{A}}_{22}(3\mathbf{Q}_{22}^2 + 2\mathbf{Q}_{12}^2 + 2\mathbf{Q}_{23}^2) + 2\widetilde{\mathrm{A}}_{12}(\mathbf{Q}_{12}(2\mathbf{Q}_{22} + \mathbf{Q}_{11}) + \mathbf{Q}_{13}\mathbf{Q}_{23})\right.$$
$$\left.+2\widetilde{\mathbf{A}}_{23}(\mathbf{Q}_{23}(2\mathbf{Q}_{22} + \mathbf{Q}_{33}) + \mathbf{Q}_{12}\mathbf{Q}_{13}) + \widetilde{\mathbf{A}}_{11}\mathbf{Q}_{12}^2 + 2\widetilde{\mathbf{A}}_{13}\mathbf{Q}_{12}\mathbf{Q}_{23} + \widetilde{\mathbf{A}}_{33}\mathbf{Q}_{23}^2\right]$$

$$\tau_{v12} = \tilde{\nu}_1\widetilde{\mathrm{A}}_{12} + \tilde{\nu}_2\left[\widetilde{\mathbf{A}}_{11}\mathbf{Q}_{12} + \widetilde{\mathrm{A}}_{12}\mathbf{Q}_{22} + \widetilde{\mathbf{A}}_{13}\mathbf{Q}_{23} + \widetilde{\mathbf{A}}_{12}\mathbf{Q}_{11} + \widetilde{\mathbf{A}}_{22}\mathbf{Q}_{12} + \widetilde{\mathbf{A}}_{23}\mathbf{Q}_{13}\right]$$
$$+\tilde{\nu}_4\left[\mathbf{Q}\tilde{A}\mathbf{Q}_{12} + \widetilde{\mathbf{A}}_{11}(\mathbf{Q}_{12}(2\mathbf{Q}_{11} + \mathbf{Q}_{22}) + \mathbf{Q}_{13}\mathbf{Q}_{23}) + 2\widetilde{\mathbf{A}}_{23}\mathbf{Q}_{12}\mathbf{Q}_{23} + \widetilde{\mathrm{A}}_{33}\mathbf{Q}_{13}\mathbf{Q}_{23}\right.$$
$$+\widetilde{\mathrm{A}}_{12}(3\mathrm{Q}_{12}^2 + \mathrm{Q}_{11}^2 + \mathrm{Q}_{22}^2 + \mathrm{Q}_{13}^2 + \mathrm{Q}_{23}^2 + \mathrm{Q}_{11}\mathrm{Q}_{22})$$
$$\left.+2\widetilde{\mathbf{A}}_{13}\mathrm{Q}_{12}\mathbf{Q}_{13} + \widetilde{\mathbf{A}}_{22}(\mathbf{Q}_{12}(2\mathbf{Q}_{22} + \mathbf{Q}_{11}) + \mathbf{Q}_{13}\mathbf{Q}_{23})\right]$$

$$\tau_{v13} = \tilde{\nu}_1\widetilde{\mathrm{A}}_{13} + \tilde{\nu}_2\left[\widetilde{\mathrm{A}}_{11}\mathbf{Q}_{13} + \widetilde{\mathrm{A}}_{12}\mathbf{Q}_{23} + \widetilde{\mathrm{A}}_{13}\mathbf{Q}_{33} + \widetilde{\mathbf{A}}_{13}\mathbf{Q}_{11} + \widetilde{\mathrm{A}}_{23}\mathbf{Q}_{12} + \widetilde{\mathrm{A}}_{33}\mathbf{Q}_{13}\right]$$
$$+\tilde{\nu}_4\left[\mathbf{Q}\tilde{A}\mathbf{Q}_{13} + \widetilde{\mathbf{A}}_{11}(\mathbf{Q}_{13}(2\mathbf{Q}_{11} + \mathbf{Q}_{33}) + \mathbf{Q}_{12}\mathbf{Q}_{23}) + 2\widetilde{\mathbf{A}}_{23}\mathbf{Q}_{13}\mathbf{Q}_{23} + \widetilde{\mathbf{A}}_{22}\mathbf{Q}_{12}\mathbf{Q}_{23}\right.$$
$$+\widetilde{\mathrm{A}}_{13}(3\mathrm{Q}_{13}^2 + \mathrm{Q}_{11}^2 + \mathrm{Q}_{33}^2 + \mathrm{Q}_{12}^2 + \mathrm{Q}_{23}^2 + \mathrm{Q}_{11}\mathrm{Q}_{33})$$
$$\left.+2\widetilde{\mathbf{A}}_{12}\mathbf{Q}_{12}\mathbf{Q}_{13} + \widetilde{\mathbf{A}}_{33}(\mathbf{Q}_{13}(2\mathbf{Q}_{33} + \mathbf{Q}_{11}) + \mathbf{Q}_{12}\mathbf{Q}_{23})\right]$$

$$\tau_{v23} = \tilde{\nu}_1\widetilde{\mathbf{A}}_{23} + \tilde{\nu}_2\left[\widetilde{\mathbf{A}}_{12}\mathbf{Q}_{13} + \widetilde{\mathbf{A}}_{22}\mathbf{Q}_{23} + \widetilde{\mathbf{A}}_{23}\mathbf{Q}_{33} + \widetilde{\mathbf{A}}_{13}\mathbf{Q}_{12} + \widetilde{\mathbf{A}}_{23}\mathbf{Q}_{22} + \widetilde{\mathbf{A}}_{33}\mathbf{Q}_{23}\right]$$
$$+\tilde{\nu}_4\left[\mathbf{Q}\tilde{A}_{23} + \widetilde{\mathbf{A}}_{22}(\mathbf{Q}_{23}(2\mathbf{Q}_{22} + \mathbf{Q}_{33}) + \mathbf{Q}_{12}\mathbf{Q}_{13}) + 2\widetilde{\mathbf{A}}_{12}\mathbf{Q}_{12}\mathbf{Q}_{23} + \widetilde{\mathbf{A}}_{11}\mathbf{Q}_{12}\mathbf{Q}_{13}\right.$$
$$+\widetilde{\mathrm{A}}_{23}(3\mathrm{Q}_{23}^2 + \mathrm{Q}_{22}^2 + \mathrm{Q}_{33}^2 + \mathrm{Q}_{12}^2 + \mathrm{Q}_{13}^2 + \mathrm{Q}_{22}\mathrm{Q}_{33})$$
$$\left.+2\widetilde{\mathrm{A}}_{13}\mathbf{Q}_{13}\mathbf{Q}_{23} + \widetilde{\mathrm{A}}_{33}(\mathbf{Q}_{23}(2\mathbf{Q}_{33} + \mathbf{Q}_{22}) + \mathbf{Q}_{12}\mathbf{Q}_{13})\right]$$

$\mathrm{Q}\widetilde{\mathrm{A}}$ and $\mathrm{QQ}\widetilde{\mathrm{A}}$ are:

$$\mathrm{Q}\widetilde{\mathrm{A}} = \mathrm{Q}_{11}\widetilde{\mathrm{A}}_{11} + \mathbf{Q}_{22}\widetilde{\mathrm{A}}_{22} + \mathbf{Q}_{33}\widetilde{\mathrm{A}}_{33} + 2\left(\mathrm{Q}_{12}\widetilde{\mathrm{A}}_{12} + \mathrm{Q}_{13}\widetilde{\mathrm{A}}_{13} + \mathrm{Q}_{23}\widetilde{\mathrm{A}}_{23}\right)$$
$$\mathrm{QQ}\widetilde{\mathrm{A}} = (\mathbf{Q}_{11}^2 + \mathrm{Q}_{12}^2 + \mathrm{Q}_{13}^2)\widetilde{\mathrm{A}}_{11} + (\mathbf{Q}_{12}^2 + \mathrm{Q}_{22}^2 + \mathrm{Q}_{23}^2)\widetilde{\mathrm{A}}_{22} + (\mathrm{Q}_{13}^2 + \mathrm{Q}_{23}^2 + \mathrm{Q}_{33}^2)\widetilde{\mathrm{A}}_{33}$$
$$+2(\mathbf{Q}_{11}\mathbf{Q}_{12} + \mathrm{Q}_{12}\mathbf{Q}_{22} + \mathrm{Q}_{13}\mathrm{Q}_{23})\widetilde{\mathrm{A}}_{12} + 2(\mathrm{Q}_{11}\mathrm{Q}_{13} + \mathrm{Q}_{12}\mathrm{Q}_{23} + \mathrm{Q}_{13}\mathrm{Q}_{33})\widetilde{\mathrm{A}}_{13}$$
$$+2(\mathbf{Q}_{12}\mathrm{Q}_{13} + \mathrm{Q}_{22}\mathbf{Q}_{23} + \mathrm{Q}_{23}\mathrm{Q}_{33})\widetilde{\mathrm{A}}_{23}$$

Anisotropic component of the total stress tensor ($\tau_{a11} = \tau_{a22} = \tau_{a33} = 0$):

$$\tau_{a12} = (\mathrm{Q}_{22} - \mathrm{Q}_{11})\mathrm{H}_{12} + (\mathrm{H}_{11} - \mathrm{H}_{22})\mathrm{Q}_{12} + \mathrm{H}_{13}\mathrm{Q}_{23} - \mathrm{H}_{23}\mathrm{Q}_{13}$$
$$\tau_{a21} = (\mathrm{Q}_{11} - \mathrm{Q}_{22})\mathrm{H}_{12} + (\mathrm{H}_{22} - \mathrm{H}_{11})\mathrm{Q}_{12} + \mathrm{H}_{23}\mathrm{Q}_{13} - \mathrm{H}_{13}\mathrm{Q}_{23}$$
$$\tau_{a13} = (\mathrm{Q}_{33} - \mathrm{Q}_{11})\mathrm{H}_{13} + (\mathrm{H}_{11} - \mathrm{H}_{33})\mathrm{Q}_{13} + \mathrm{H}_{12}\mathrm{Q}_{23} - \mathrm{H}_{23}\mathrm{Q}_{12}$$
$$\tau_{a31} = (\mathrm{Q}_{11} - \mathrm{Q}_{33})\mathrm{H}_{13} + (\mathrm{H}_{33} - \mathrm{H}_{11})\mathrm{Q}_{13} + \mathrm{H}_{23}\mathrm{Q}_{12} - \mathrm{H}_{12}\mathrm{Q}_{23}$$
$$\tau_{a23} = (\mathrm{Q}_{33} - \mathrm{Q}_{22})\mathrm{H}_{23} + (\mathrm{H}_{22} - \mathrm{H}_{33})\mathrm{Q}_{23} + \mathrm{H}_{12}\mathrm{Q}_{13} - \mathrm{H}_{13}\mathrm{Q}_{12}$$
$$\tau_{a32} = (\mathrm{Q}_{22} - \mathrm{Q}_{33})\mathrm{H}_{23} + (\mathrm{H}_{33} - \mathrm{H}_{22})\mathrm{Q}_{23} + \mathrm{H}_{13}\mathrm{Q}_{12} - \mathrm{H}_{12}\mathrm{Q}_{13}$$

QH and QQH are:

$$\mathrm{QH} = \mathrm{Q}_{11}\mathrm{H}_{11} + \mathrm{Q}_{22}\mathrm{H}_{22} + \mathrm{Q}_{33}\mathrm{H}_{33} + 2(\mathrm{Q}_{12}\mathrm{H}_{12} + \mathrm{Q}_{13}\mathrm{H}_{13} + \mathrm{Q}_{23}\mathrm{H}_{23})$$

$$\begin{aligned}\mathrm{QQH} = {} & (\mathrm{Q}_{11}^2 + \mathrm{Q}_{12}^2 + \mathrm{Q}_{13}^2)\mathrm{H}_{11} + (\mathrm{Q}_{12}^2 + \mathrm{Q}_{22}^2 + \mathrm{Q}_{23}^2)\mathrm{H}_{22} + (\mathrm{Q}_{13}^2 + \mathrm{Q}_{23}^2 + \mathrm{Q}_{33}^2)\mathrm{H}_{33} \\ & + 2(\mathrm{Q}_{11}\mathrm{Q}_{12} + \mathrm{Q}_{12}\mathrm{Q}_{22} + \mathrm{Q}_{13}\mathrm{Q}_{23})\mathrm{H}_{12} + 2(\mathrm{Q}_{11}\mathrm{Q}_{13} + \mathrm{Q}_{12}\mathrm{Q}_{23} + \mathrm{Q}_{13}\mathrm{Q}_{33})\mathrm{H}_{13} \\ & + 2(\mathrm{Q}_{12}\mathrm{Q}_{13} + \mathrm{Q}_{22}\mathrm{Q}_{23} + \mathrm{Q}_{23}\mathrm{Q}_{33})\mathrm{H}_{23}\end{aligned}$$

Elastic component of total stress tensor:

$$\begin{aligned}\tau_{e11} = {} & -\frac{2}{3}\beta\mathbf{H}_{11} - 2\beta[\mathbf{H}_{11}\mathbf{Q}_{11} + \mathbf{H}_{12}\mathbf{Q}_{12} + \mathbf{H}_{13}\mathbf{Q}_{13} - \mathrm{QH3}] \\ & + \frac{1}{2}\beta[\mathrm{QHQ}_{11} - \mathrm{QQH} + \mathrm{H}_{11}(3\mathrm{Q}_{11}^2 + 2\mathrm{Q}_{12}^2 + 2\mathrm{Q}_{13}^2) \\ & + 2\mathrm{H}_{12}(\mathrm{Q}_{12}(2\mathrm{Q}_{11} + \mathrm{Q}_{22}) + \mathrm{Q}_{13}\mathrm{Q}_{23}) + 2\mathrm{H}_{13}(\mathrm{Q}_{13}(2\mathrm{Q}_{11} + \mathrm{Q}_{33}) + \mathrm{Q}_{12}\mathrm{Q}_{23}) \\ & + \mathrm{H}_{22}\mathrm{Q}_{12}^2 + 2\mathrm{H}_{23}\mathrm{Q}_{12}\mathrm{Q}_{13} + \mathrm{H}_{33}\mathrm{Q}_{13}^2]\end{aligned}$$

$$\begin{aligned}\tau_{e22} = {} & -\frac{2}{3}\beta\mathbf{H}_{22} - 2\beta[\mathbf{H}_{12}\mathbf{Q}_{12} + \mathbf{H}_{22}\mathbf{Q}_{22} + \mathbf{H}_{23}\mathbf{Q}_{23} - \mathrm{QH}/3] \\ & + \frac{1}{2}\beta[\mathrm{QH}_{22} - \mathrm{QQH} + \mathrm{H}_{22}(3\mathbf{Q}_{22}^2 + 2\mathbf{Q}_{12}^2 + 2\mathbf{Q}_{23}^2) \\ & + 2\mathbf{H}_{12}(\mathbf{Q}_{12}(2\mathbf{Q}_{22} + \mathbf{Q}_{11}) + \mathbf{Q}_{13}\mathbf{Q}_{23}) + 2\mathbf{H}_{23}(\mathbf{Q}_{23}(2\mathbf{Q}_{22} + \mathrm{Q}_{33}) + \mathrm{Q}_{12}\mathbf{Q}_{13}) \\ & + \mathrm{H}_{11}\mathbf{Q}_{12}^2 + 2\mathrm{H}_{13}\mathbf{Q}_{12}\mathbf{Q}_{23} + \mathrm{H}_{33}\mathbf{Q}_{23}^2]\end{aligned}$$

$$\begin{aligned}\tau_{e12} = {} & -\frac{2}{3}\beta\mathrm{H}_{12} - \beta[\mathrm{H}_{11}\mathbf{Q}_{12} + \mathrm{H}_{12}\mathbf{Q}_{22} + \mathrm{H}_{13}\mathbf{Q}_{23} + \mathrm{H}_{12}\mathrm{Q}_{11} + \mathrm{H}_{22}\mathbf{Q}_{12} + \mathrm{H}_{23}\mathbf{Q}_{13}] \\ & + \frac{1}{2}\beta[\mathrm{H}_{11}(\mathrm{Q}_{12}(2\mathrm{Q}_{11} + \mathrm{Q}_{22}) + \mathrm{Q}_{13}\mathrm{Q}_{23}) + 2\mathrm{H}_{13}\mathrm{Q}_{12}\mathrm{Q}_{13} \\ & + \mathrm{H}_{12}(3\mathrm{Q}_{12}^2 + \mathrm{Q}_{11}^2 + \mathrm{Q}_{22}^2 + \mathrm{Q}_{13}^2 + \mathrm{Q}_{23}^2 + \mathrm{Q}_{11}\mathrm{Q}_{22}) \\ & + \mathrm{H}_{22}(\mathrm{Q}_{12}(2\mathrm{Q}_{22} + \mathrm{Q}_{11}) + \mathrm{Q}_{13}\mathrm{Q}_{23}) + 2\mathrm{H}_{23}\mathrm{Q}_{12}\mathrm{Q}_{23} + \mathrm{H}_{33}\mathrm{Q}_{13}\mathrm{Q}_{23} + \mathrm{QH}_{Q12}]\end{aligned}$$

$$\begin{aligned}\tau_{e13} = {} & -\frac{2}{\beta}\mathrm{H}_{13} - \beta[\mathrm{H}_{11}\mathrm{Q}_{13} + \mathrm{H}_{12}\mathrm{Q}_{23} + \mathrm{H}_{13}\mathrm{Q}_{33} + \mathrm{H}_{13}\mathrm{Q}_{11} + \mathrm{H}_{23}\mathrm{Q}_{12} + \mathrm{H}_{33}\mathrm{Q}_{13}] \\ & + \frac{1}{2}\beta[\mathrm{H}_{11}(\mathrm{Q}_{13}(2\mathrm{Q}_{11} + \mathrm{Q}_{33}) + \mathrm{Q}_{12}\mathrm{Q}_{23}) + 2\mathrm{H}_{12}\mathrm{Q}_{12}\mathrm{Q}_{13} \\ & + \mathrm{H}_{13}(3\mathrm{Q}_{13}^2 + \mathrm{Q}_{11}^2 + \mathrm{Q}_{33}^2 + \mathrm{Q}_{12}^2 + \mathrm{Q}_{23}^2 + \mathrm{Q}_{11}\mathrm{Q}_{33}) \\ & + \mathrm{H}_{33}(\mathrm{Q}_1\beta(2\mathrm{Q}_{33} + \mathrm{Q}_{11}) + \mathrm{Q}_{12}\mathrm{Q}_{23}) + 2\mathrm{H}_{23}\mathrm{Q}_{13}\mathrm{Q}_{23} + \mathrm{H}_{22}\mathrm{Q}_{12}\mathrm{Q}_{23} + \mathrm{QHQ}_{13}]\end{aligned}$$

$$\begin{aligned}\tau_{e23} = {} & -\frac{2}{3}\beta\mathrm{H}_{23} - \beta[\mathrm{H}_{12}\mathrm{Q}_{13} + \mathrm{H}_{22}\mathrm{Q}_{23} + \mathrm{H}_{23}\mathrm{Q}_{33} + \mathrm{H}_{13}\mathrm{Q}_{12} + \mathrm{H}_{23}\mathrm{Q}_{22} + \mathrm{H}_{33}\mathrm{Q}_{23}] \\ & + \frac{1}{2}\beta[\mathrm{H}_{22}(\mathrm{Q}_{23}(2\mathrm{Q}_{22} + \mathrm{Q}_{33}) + \mathrm{Q}_{12}\mathrm{Q}_{13}) + 2\mathrm{H}_{13}\mathrm{Q}_{13}\mathrm{Q}_{23} \\ & + \mathrm{H}_{23}(3\mathrm{Q}_{23}^2 + \mathrm{Q}_{22}^2 + \mathrm{Q}_{33}^2 + \mathrm{Q}_{12}^2 + \mathrm{Q}_{13}^2 + \mathrm{Q}_{22}\mathrm{Q}_{33}) \\ & + \mathrm{H}_{33}(\mathrm{Q}_{23}(2\mathrm{Q}_{33} + \mathrm{Q}_{22}) + \mathrm{Q}_{12}\mathrm{Q}_{13}) + 2\mathrm{H}_{12}\mathrm{Q}_{12}\mathrm{Q}_{23} + \mathrm{H}_{11}\mathrm{Q}_{12}\mathrm{Q}_{13} + \mathrm{QHQ}_{23}]\end{aligned}$$

Ericksen component of total stress tensor:

$$\tau_{Er11} = -\left\{\left(\frac{\partial \mathbf{Q}_{11}}{\partial \tilde{x}} + \frac{\partial \mathbf{Q}_{11}}{\partial \tilde{y}} + \frac{\partial \mathbf{Q}_{11}}{\partial \tilde{z}}\right)\left[(1+L^{\star})\left(\frac{\partial \mathbf{Q}_{11}}{\partial \tilde{x}} + \frac{\partial \mathbf{Q}_{12}}{\partial \tilde{x}} + \frac{\partial \mathbf{Q}_{13}}{\partial \tilde{x}}\right)\right.\right.$$
$$\left. + L^{\star}\left(\frac{\partial \mathbf{Q}_{12}}{\partial \tilde{y}} + \frac{\partial \mathbf{Q}_{22}}{\partial \tilde{y}} + \frac{\partial \mathbf{Q}_{23}}{\partial \tilde{y}}\right) + L^{\star}\left(\frac{\partial \mathbf{Q}_{13}}{\partial \tilde{z}} + \frac{\partial \mathbf{Q}_{23}}{\partial \tilde{z}} + \frac{\partial \mathbf{Q}_{33}}{\partial \tilde{z}}\right)\right]$$
$$\left. + \frac{\partial \mathbf{Q}_{12}{}^{2}}{\partial \tilde{x}} + \frac{\partial \mathbf{Q}_{13}{}^{2}}{\partial \tilde{x}} + \frac{\partial \mathbf{Q}_{23}}{\partial \tilde{x}}\left(\frac{\partial \mathbf{Q}_{12}}{\partial \tilde{z}} + \frac{\partial \mathbf{Q}_{13}}{\partial \tilde{y}}\right) + \frac{\partial \mathbf{Q}_{12}}{\partial \tilde{y}}\frac{\partial \mathbf{Q}_{22}}{\partial \tilde{x}} + \frac{\partial \mathbf{Q}_{13}}{\partial \tilde{z}}\frac{\partial \mathbf{Q}_{33}}{\partial \tilde{x}}\right\}$$

$$\tau_{Er22} = -\left\{\left(\frac{\partial \mathbf{Q}_{22}}{\partial \tilde{x}} + \frac{\partial \mathbf{Q}_{22}}{\partial \tilde{y}} + \frac{\partial \mathbf{Q}_{22}}{\partial \tilde{z}}\right)\left[(1+L^{\star})\left(\frac{\partial \mathbf{Q}_{12}}{\partial \tilde{y}} + \frac{\partial \mathbf{Q}_{22}}{\partial \tilde{y}} + \frac{\partial \mathbf{Q}_{23}}{\partial \tilde{y}}\right)\right.\right.$$
$$\left. + L^{\star}\left(\frac{\partial \mathbf{Q}_{11}}{\partial \tilde{x}} + \frac{\partial \mathbf{Q}_{12}}{\partial \tilde{x}} + \frac{\partial \mathbf{Q}_{13}}{\partial \tilde{x}}\right) + L^{\star}\left(\frac{\partial \mathbf{Q}_{13}}{\partial \tilde{z}} + \frac{\partial \mathbf{Q}_{23}}{\partial \tilde{z}} + \frac{\partial \mathbf{Q}_{33}}{\partial \tilde{z}}\right)\right]$$
$$\left. + \frac{\partial \mathbf{Q}_{12}{}^{2}}{\partial \tilde{y}} + \frac{\partial \mathbf{Q}_{23}{}^{2}}{\partial \tilde{y}} + \frac{\partial \mathbf{Q}_{13}}{\partial \tilde{y}}\left(\frac{\partial \mathbf{Q}_{12}}{\partial \tilde{z}} + \frac{\partial \mathbf{Q}_{23}}{\partial \tilde{x}}\right) + \frac{\partial \mathbf{Q}_{11}}{\partial \tilde{y}}\frac{\partial \mathbf{Q}_{12}}{\partial \tilde{x}} + \frac{\partial \mathbf{Q}_{23}}{\partial \tilde{z}}\frac{\partial \mathbf{Q}_{33}}{\partial \tilde{y}}\right\}$$

$$\tau_{Er12} = -\left\{\left(\frac{\partial \mathbf{Q}_{12}}{\partial \tilde{x}} + \frac{\partial \mathbf{Q}_{12}}{\partial \tilde{y}} + \frac{\partial \mathbf{Q}_{12}}{\partial \tilde{z}}\right)\left[(1+L^{\star})\left(\frac{\partial \mathbf{Q}_{11}}{\partial \tilde{x}} + \frac{\partial \mathbf{Q}_{12}}{\partial \tilde{x}} + \frac{\partial \mathbf{Q}_{13}}{\partial \tilde{x}}\right)\right.\right.$$
$$\left. + L^{\star}\left(\frac{\partial \mathbf{Q}_{12}}{\partial \tilde{y}} + \frac{\partial \mathbf{Q}_{22}}{\partial \tilde{y}} + \frac{\partial \mathbf{Q}_{23}}{\partial \tilde{y}}\right) + L^{\star}\left(\frac{\partial \mathbf{Q}_{13}}{\partial \tilde{z}} + \frac{\partial \mathbf{Q}_{23}}{\partial \tilde{z}} + \frac{\partial \mathbf{Q}_{33}}{\partial \tilde{z}}\right)\right]$$
$$\left. + \frac{\partial \mathbf{Q}_{23}}{\partial \tilde{x}}\left(\frac{\partial \mathbf{Q}_{13}}{\partial \tilde{x}} + \frac{\partial \mathbf{Q}_{23}}{\partial \tilde{y}} + \frac{\partial \mathbf{Q}_{22}}{\partial \tilde{z}}\right) + \frac{\partial \mathbf{Q}_{23}}{\partial \tilde{z}}\frac{\partial \mathbf{Q}_{33}}{\partial \tilde{x}} + \frac{\partial \mathbf{Q}_{22}}{\partial \tilde{x}}\left(\frac{\partial \mathbf{Q}_{12}}{\partial \tilde{x}} + \frac{\partial \mathbf{Q}_{22}}{\partial \tilde{y}}\right)\right\}$$

$$\tau_{Er13} = -\left\{\left(\frac{\partial \mathbf{Q}_{13}}{\partial \tilde{x}} + \frac{\partial \mathbf{Q}_{13}}{\partial \tilde{y}} + \frac{\partial \mathbf{Q}_{13}}{\partial \tilde{z}}\right)\left[(1+L^{\star})\left(\frac{\partial \mathbf{Q}_{11}}{\partial \tilde{x}} + \frac{\partial \mathbf{Q}_{12}}{\partial \tilde{x}} + \frac{\partial \mathbf{Q}_{13}}{\partial \tilde{x}}\right)\right.\right.$$
$$\left. + L^{\star}\left(\frac{\partial \mathbf{Q}_{12}}{\partial \tilde{y}} + \frac{\partial \mathbf{Q}_{22}}{\partial \tilde{y}} + \frac{\partial \mathbf{Q}_{23}}{\partial \tilde{y}}\right) + L^{\star}\left(\frac{\partial \mathbf{Q}_{13}}{\partial \tilde{z}} + \frac{\partial \mathbf{Q}_{23}}{\partial \tilde{z}} + \frac{\partial \mathbf{Q}_{33}}{\partial \tilde{z}}\right)\right]$$
$$\left. + \frac{\partial \mathbf{Q}_{23}}{\partial \tilde{x}}\left(\frac{\partial \mathbf{Q}_{12}}{\partial \tilde{x}} + \frac{\partial \mathbf{Q}_{33}}{\partial \tilde{y}} + \frac{\partial \mathbf{Q}_{23}}{\partial \tilde{z}}\right) + \frac{\partial \mathbf{Q}_{23}}{\partial \tilde{y}}\frac{\partial \mathbf{Q}_{22}}{\partial \tilde{x}} + \frac{\partial \mathbf{Q}_{33}}{\partial \tilde{x}}\left(\frac{\partial \mathbf{Q}_{13}}{\partial \tilde{x}} + \frac{\partial \mathbf{Q}_{33}}{\partial \tilde{z}}\right)\right\}$$

$$\tau_{E_{r23}} = -\left\{\left(\frac{\partial \mathbf{Q}_{23}}{\partial \tilde{x}} + \frac{\partial \mathbf{Q}_{23}}{\partial \tilde{y}} + \frac{\partial \mathbf{Q}_{23}}{\partial \tilde{z}}\right)\left[(1+L^{\star})\left(\frac{\partial \mathbf{Q}_{12}}{\partial \tilde{y}} + \frac{\partial \mathbf{Q}_{22}}{\partial \tilde{y}} + \frac{\partial \mathbf{Q}_{23}}{\partial \tilde{y}}\right)\right.\right.$$
$$\left. + L^{\star}\left(\frac{\partial \mathbf{Q}_{11}}{\partial \tilde{x}} + \frac{\partial \mathbf{Q}_{12}}{\partial \tilde{x}} + \frac{\partial \mathbf{Q}_{13}}{\partial \tilde{x}}\right) + L^{\star}\left(\frac{\partial \mathbf{Q}_{13}}{\partial \tilde{z}} + \frac{\partial \mathbf{Q}_{23}}{\partial \tilde{z}} + \frac{\partial \mathbf{Q}_{33}}{\partial \tilde{z}}\right)\right]$$
$$\left. + \frac{\partial \mathbf{Q}_{13}}{\partial \tilde{y}}\left(\frac{\partial \mathbf{Q}_{33}}{\partial \tilde{x}} + \frac{\partial \mathbf{Q}_{12}}{\partial \tilde{y}} + \frac{\partial \mathbf{Q}_{13}}{\partial \tilde{z}}\right) + \frac{\partial \mathbf{Q}_{11}}{\partial \tilde{y}}\frac{\partial \mathbf{Q}_{13}}{\partial \tilde{x}} + \frac{\partial \mathbf{Q}_{33}}{\partial \tilde{y}}\left(\frac{\partial \mathbf{Q}_{23}}{\partial \tilde{y}} + \frac{\partial \mathbf{Q}_{33}}{\partial \tilde{z}}\right)\right\}$$

And the last term, the chiral term, is:

$$\mathcal{P}_{11} = 2\frac{\partial Q_{13}}{\partial y}$$

$$\mathcal{P}_{12} = -\frac{\partial Q_{13}}{\partial x} + \frac{\partial Q_{23}}{\partial y}$$

$$\mathcal{P}_{13} = \frac{\partial Q_{12}}{\partial x} - \frac{\partial Q_{11}}{\partial y} + \frac{\partial Q_{33}}{\partial y}$$

$$\mathcal{P}_{22} = -2\frac{\partial Q_{23}}{\partial x}$$

$$\mathcal{P}_{33} = \frac{\partial Q_{22}}{\partial x} - \frac{\partial Q_{33}}{\partial x} - \frac{\partial Q_{12}}{\partial y}$$